FILAMENT CARBURIZATION DURING THE HOT-WIRE CHEMICAL VAPOUR DEPOSITION OF CARBON NANOTUBES

by

CLIVE JUSTIN OLIPHANT

Submitted in partial fulfilment of the requirements of the
degree of Magister Scientiae in the Department of Physics, University of the
Western Cape

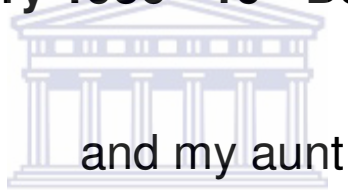|	
Supervisor:	**Dr. C. J. Arendse, National Centre for Nano-Structured Materials (NCNSM), Council for Scientific and Industrial Research (CSIR)**
Co-supervisor:	**Prof. D. K. Knoesen, University of the Western Cape (UWC)**

May 2008

This thesis is dedicated to the loving memories

of my grandmother

SARAH OLIPHANT

(15th January 1936 - 19th December 2006)

and my aunt

RITA MOFOKENG

(1st March 1965 - 18th July 2005)

KEYWORDS

FILAMENT CARBURIZATION DURING THE HOT-WIRE CHEMICAL VAPOUR DEPOSITION OF CARBON NANOTUBES

Clive Justin Oliphant

Multi-walled carbon nanotubes

Hot-wire CVD

Carburization

Structural properties

Morphology

Structural perfection

Filament poisoning

Stability

In situ resistance

Filament-temperature

ABSTRACT

FILAMENT CARBURIZATION DURING THE HOT-WIRE CHEMICAL VAPOUR DEPOSITION OF CARBON NANOTUBES

Clive Justin Oliphant
MSc Thesis, Department of Physics, University of the Western Cape

Carbon nanotubes (CNTs) are one-dimensional structures that possess extraordinary properties, which render them ideal candidates for various applications. Currently, these materials are synthesised using several techniques. The most promising technique for a controlled and repeatable mass-production of CNTs is hot-wire chemical vapour deposition (HWCVD). Single (S) - or multi-walled (MW) CNTs can be grown using this technique either in the gas phase or directly on a substrate coated with transition metal nanoparticles. Furthermore, this technique has the ability to synthesise CNTs that are aligned perpendicular to the substrate, which is considered vital for device applications. Presently, the self-assemble growth mechanism of CNTs is not well understood. Researchers therefore focused on the effect of each deposition parameter on the structural properties of the synthesised CNTs. However, few studies have concentrated on the role of the filament itself during the deposition.

This study reports on the changes in the structural properties of a tungsten-filament when exposed to a methane / hydrogen ambient for different durations at various filament-temperatures. These changes have an effect on the morphology and structural properties of the synthesised MWCNTs. Using x-ray diffraction, scanning electron microscopy, energy dispersive x-ray spectroscopy and Raman spectroscopy, it is found that 1400 °C is the optimum filament-temperature at the present deposition conditions. At this temperature the filament undergoes minimal structural changes that ensure a relatively stable deposition process. Consequently, MWCNTs with a high structural perfection and relatively less impurity concentration are synthesised.

May 2008

DECLARATION

I declare that

''FILAMENT CARBURIZATION DURING THE HOT-WIRE CHEMICAL VAPOUR DEPOSITION OF CARBON NANOTUBES''

is my own work, that it has not been submitted for any degree or examination in any other university, and that all the sources I have used or quoted have been indicated and acknowledged by means of complete references.

Clive Justin Oliphant

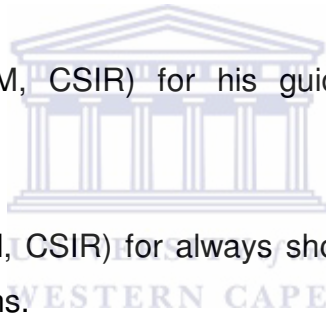**Signature: ……………………….**   **May 2008**

ACKNOWLEDGEMENTS

Thank you!

TABLE OF CONTENTS

CHAPTER ONE

INTRODUCTION

1.1 Crystalline carbon allotropes

Carbon is a non-metal and occurs by itself in nature in different forms called allotropes. Diamond is the rarest crystalline allotrope of carbon where the bonds between the carbon atoms are sp^3 hybridised. This bonding results in the characteristically strong carbon-carbon bond of diamond in a tetrahedral arrangement as shown in figure 1.1 [1.1]. On the other hand, graphite is the most stable allotrope of carbon. It is commonly used in pencil leads and as a lubricant. The carbon bonds in graphite are sp^2 hybridised and consequently lay in a plane at an angle of 120° to each other. As a result, the structure of graphite resembles that of a two dimensional (2-D) sheet of hexagonal rings, schematically shown in figure 1.2 [1.1]. Weak van der Waals forces exist between the single graphite sheets whilst the in-plane carbon-carbon atoms have a shorter bond length and consequently a stronger bond than diamond.
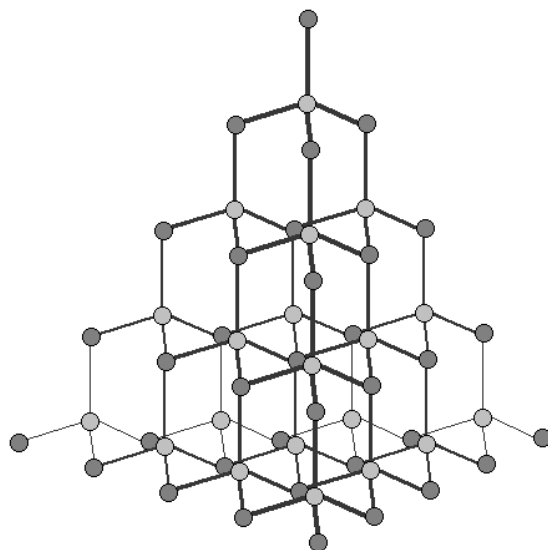
Figure 1.1: *Schematic illustration of the tetrahedral arrangement of diamond at molecular scale [1.1]*
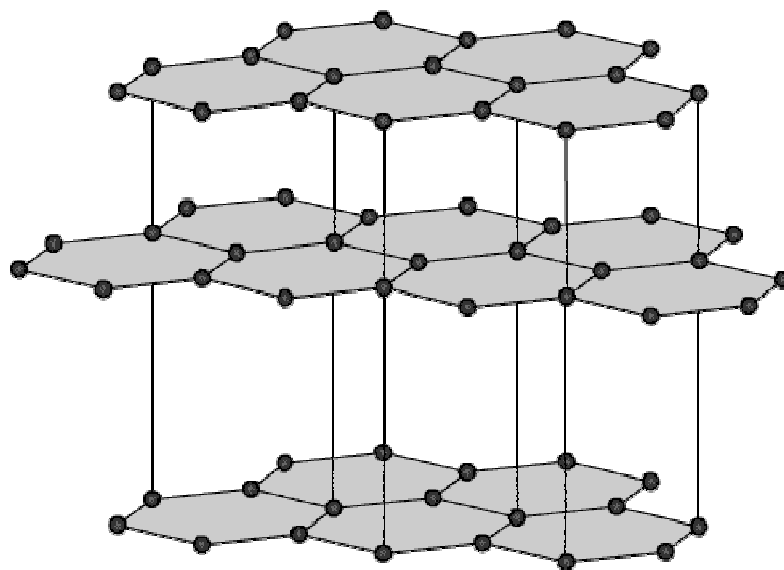
Figure 1.2: *Schematic representation of the bonding in graphite [1.1]*

The vaporisation of graphite using a focus-pulsed laser led Kroto *et al.* [1.2] to the discovery of fullerenes in 1985. These molecules are stable and consist of carbon in a cage-like structure. The first discovered fullerene is called the Buckministerfullerene and it contains sixty carbon atoms (C_{60}) in a football-like structure as shown in figure 1.3 [1.2].
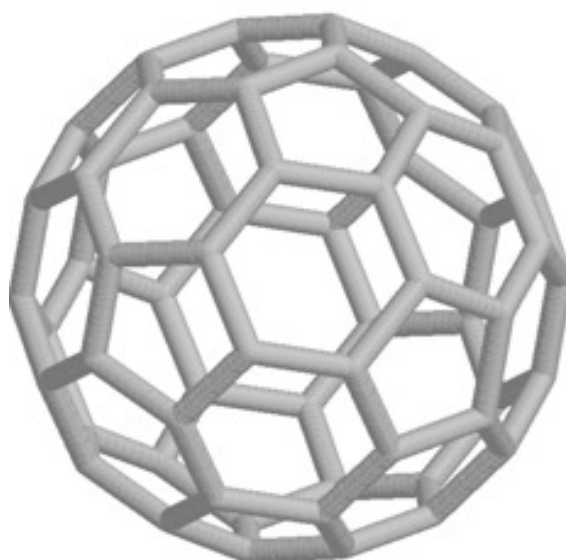
Figure 1.3: *Proposed schematic resembling the structure of C_{60} in order to satisfy the valence of sixty carbon atoms [1.2]*

Sumio Iijima used a high-resolution transmission electron microscope (HRTEM) to study soot from the arc-vaporisation of graphite rods. In 1991, he reported on nano-sized carbon needles, shown in figure 1.4, known today as carbon nanotubes (CNTs) [1.3].
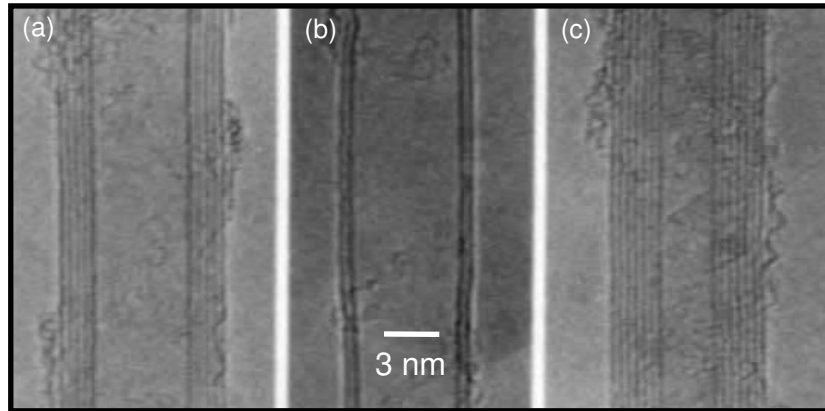
Figure 1.4: *HRTEM micrographs of CNTs with: a) 5 walls, b) 2 walls and c) 7 walls [1.3]*

1.2   Structure of carbon nanotubes

CNTs have a large aspect ratio since they can grow up to a few micrometers in length with a nanometer-sized diameter [1.3]. CNTs are therefore one-dimensional (1-D) structures. Figure 1.5 shows a schematic depicting the different configurations of an ideal single-walled carbon nanotube (SWCNT). A SWCNT is a singular 2-D graphite sheet (graphene) rolled up seamlessly and capped by half a fullerene. Three types of SWCNTs are realised by rolling the graphene sheet in a specific direction relative to its axis, which is referred to as the chiral angle (θ). An armchair SWCNT forms by rolling the graphene sheet at an angle of 30°. The zigzag type of SWCNT forms by an angle of 0° whilst a chiral SWCNT forms by rolling the graphene sheet at any angle between 0° and 30°.
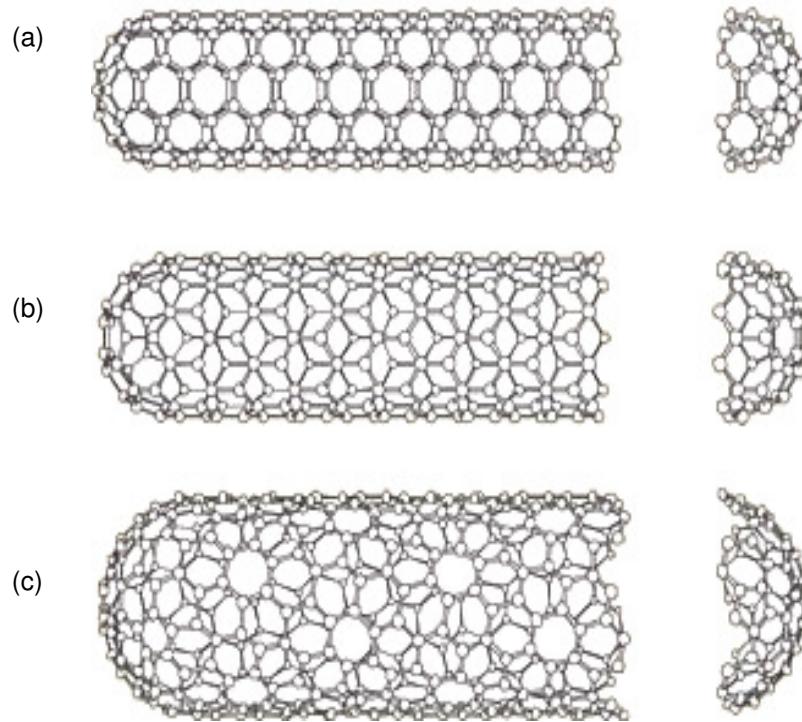
Figure 1.5: *Schematic representation of: a) an armchair, b) zigzag and c) chiral carbon nanotube [1.4]*

Dresselhaus *et al.* [1.4] define a chiral vector $\vec{C}_h$ expressed in equation (1.1) that can describe the structure of a SWCNT, except for its length.

$$\vec{C}_h = n\vec{a}_1 + m\vec{a}_2 \qquad (1.1)$$

where $\vec{a}_1$, $\vec{a}_2$ are the unit cell base vectors of the graphene sheet, n and m are integers and $n \geq m$. The magnitude of $\vec{a}_1$ and $\vec{a}_2$ is given by a = $\sqrt{3}$ x $a_{C\text{-}C}$ = $\sqrt{3}$ x 0.142 nm = 0.246 nm, where $a_{C\text{-}C}$ is the closest distance between two carbon atoms in a graphene sheet. Figure 1.6 presents a schematic showing the chiral vector, chiral angle, the zigzag and armchair axes [1.5].
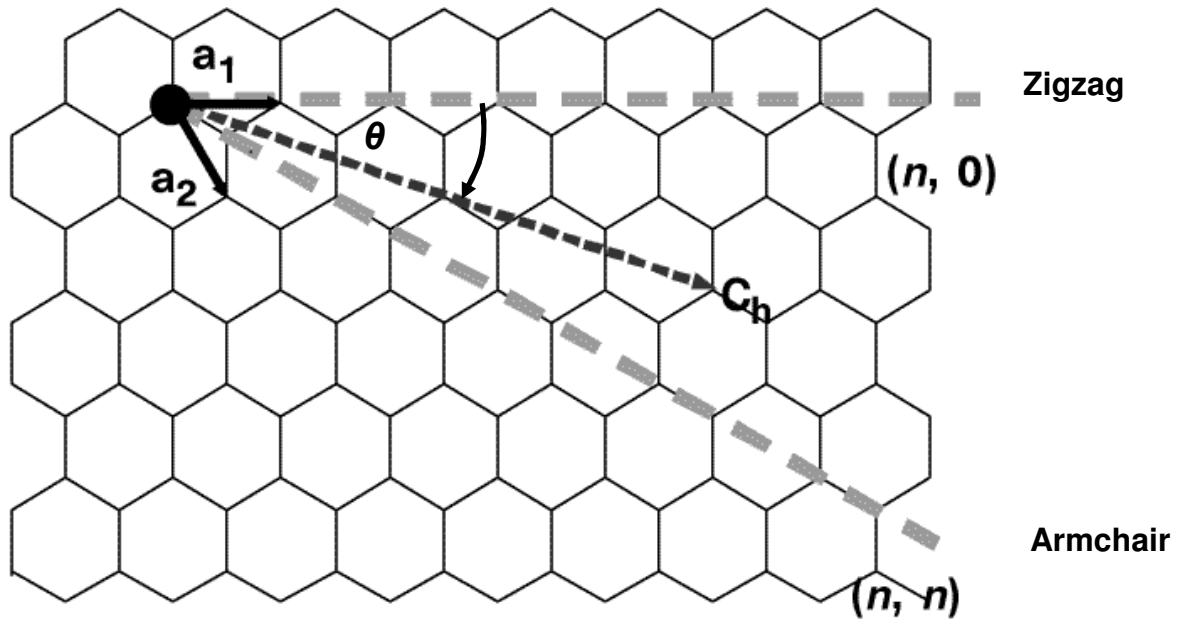
Figure 1.6: *Schematic showing an unfolded graphene sheet, chiral vector, chiral angle, the zigzag and armchair axes [1.5]*

The chiral vector connects two coinciding crystallographic equivalent points upon the formation of tube. This means that the magnitude of $\vec{C}_h$ is simply the circumference of the tube (in nm) by [1.4]:

$$\left|\overrightarrow{C_h}\right| = 0.246 \sqrt{n^2 + m^2 + nm} \qquad (1.2)$$

The diameter (in nm) of the tube is thus given by:

$$d_t = \frac{\left|\overrightarrow{C_h}\right|}{\pi} = \frac{0.246\sqrt{n^2 + m^2 + nm}}{\pi} \qquad (1.3)$$

As mentioned earlier, the chiral angle is the angle between $\vec{C}_h$ and the zigzag axis ($\theta = 0°$) as shown in figure 1.6 and is expressed as [1.4]:

$$\theta = \cos^{-1} \frac{2n + m}{2\sqrt{n^2 + nm + m^2}} \qquad (1.4)$$

The number of carbon atoms contained in a unit cell, N_C, is proportional to the ratio of the areas of the cylinder surface and the graphene unit cell. Since there are 2 atoms per graphene unit cell, N_C is given by equation (1.5) as [1.4]:

$$N_C = \frac{2\left(n^2 + nm + m^2\right)}{d_R} \tag{1.5}$$

where d_R is equal to the highest common divisor of n and m, i.e. d_H, if the difference $n - m$ is not a multiple of 3 or $d_R = 3d_H$ if $n - m$ is a multiple of 3.

On the other hand, the structure of multi-walled carbon nanotubes (MWCNTs) resembles a collection of concentric SWCNTs, as schematically shown in figure 1.7 [1.3]. The distance between each SWCNT is slightly larger than that between graphene layers in graphite [1.3 - 1.7].
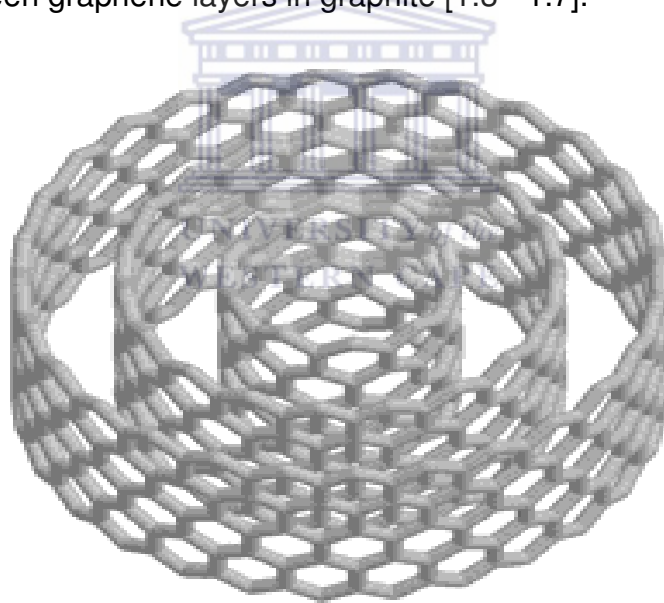
Figure 1.7: *Schematic representation of a MWCNT [1.7]*

1.3   Properties of carbon nanotubes

As mentioned earlier, CNTs are 1-D structures and therefore possess interesting properties and applications. CNTs are ballistic electrical conductors at room temperature [1.8] and can be either metallic or semiconducting, depending on the indices *(n,m)* [1.9]. Calculated dispersion relations for a (5,5) armchair tube, (9,0) zigzag tube and a (10,0) zigzag tube are shown in figure 1.8. The tubes in figure 1.8a - b are metallic because the valence and conduction bands overlap, whilst 1.8c is a semiconductor because of the separation of the bands.
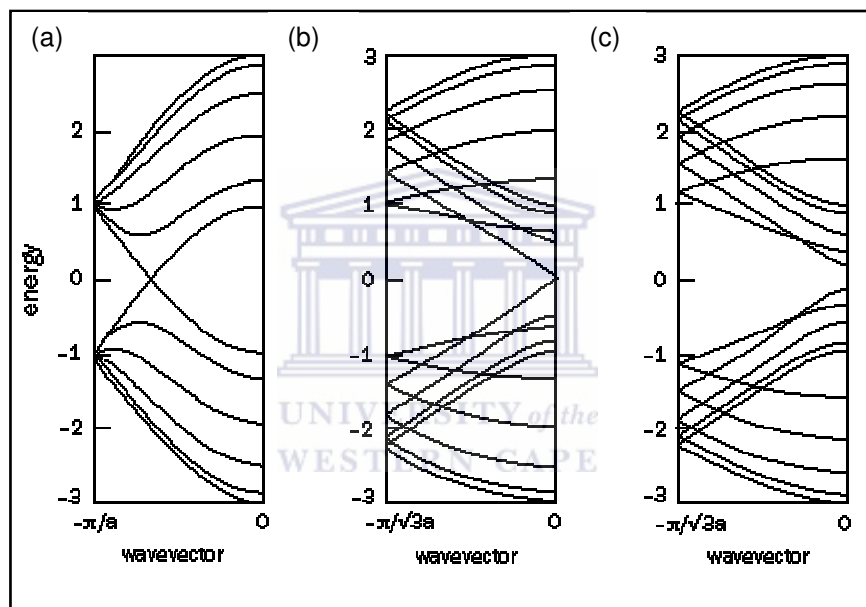
Figure 1.8: *Calculated dispersion relations for (a) (5,5) armchair tube, (b)*
(9,0) zigzag tube and (c) zigzag (10,0) [1.9]

A single MWCNT have the highest measured thermal conductivity (~3000 $Wm^{-1}K^{-1}$) of all known materials [1.10]. The strong C-C bonds render CNTs the ultimate fibers. The measured Young's modulus of 810 ± 410 GPa for a single MWCNT [1.11] ensures that CNTs can sustain extreme applied forces but retain their structural integrity afterwards.

Furthermore, these remarkable materials show good field emission capabilities. CNT emitters remain stable for longer while operating in moderate vacuum conditions compared to usual metal emitters [1.12]. CNT emitters are two times more intense than a conventional thermionic cathode ray tube (CRT) lighting element [1.13] and the nanotube cathode had a lifetime of ~8000 hrs [1.14]. CNT-based flat panel displays and electron microscopes include the prospect of saving energy as well as being environmentally friendly and economically competitive due to pure CNTs consisting of 100 % carbon [1.12].

1.4   Hot-wire chemical vapour deposition

The three most widely reported synthesis routes for CNTs are laser ablation [1.15], arc discharge [1.16] and chemical vapour deposition (CVD) [1.17 - 1.21]. Due to its gas phase mechanism, the CVD technique holds the most promise for mass-production of CNTs. However, the low degree of control over the deposition process leads to poor reproduction. On the other hand, another version of CVD called the hot-wire chemical vapour deposition (HWCVD) technique has a localised region of catalytic precursors dissociation, which is at the surface of the filament. This leads to an increase in controllability and repeatability of the deposition process compared to thermal CVD.

The HWCVD technique of synthesising various materials has been in use for nearly thirty years. Weisman *et al.* [1.22] used HWCVD to synthesise silicon films as early as 1979. Later on in 1982, Matsumoto *et al.* [1.23] synthesised diamond-like carbon (DLC) with the HWCVD technique. The filament has the ability to dissociate molecular hydrogen (H_2) catalytically into atomic hydrogen, which etches away the dangling bonds. Compared to other CVD techniques, the HWCVD of SWCNTs requires the simultaneous use of a catalyst, e.g. nickel (Ni), cobalt (Co) or iron (Fe) or an alloy of these materials, and a resistively heated filament.

During the HWCVD process of producing CNTs, a mixture of precursor gases, e.g. H_2 and methane (CH_4), is introduced into a chamber or quartz tube containing a tungsten (W) or tantalum (Ta) filament. At high temperatures, the catalytic action of the filament results in the dissociation of the precursor gases into reactive species. These reactive species subsequently participate in secondary gas phase reactions. Provided that the optimum deposition conditions are maintained, carbon species self assemble into CNTs on nanoparticles of transition metals or in vapours comprising of such nanoparticles [1.24 - 1.26]. Depending on the deposition conditions, both MWCNTs and SWCNTs can be selectively synthesised using the HWCVD technique [1.25]. Furthermore, this synthesis technique has the ability to produce aligned CNTs, which is important for some device applications [1.13]. There is no need to use expensive laser equipment or high arc temperatures during HWCVD. Furthermore, unlimited scaling up of the substrate area, low deposition temperatures, growth of isolated CNTs and repeatable nature of the deposition process, results in the HWCVD technique to be an attractive method for mass-production of CNTs. However, not just any metal filament is suitable for HWCVD. A certain criterion has to be adhered to for a filament to be used in HWCVD for reliable stability during the deposition process.

1.5   Required filament properties

A filament with a high melting point is required in order to remain intact during operation at temperatures above 1000 °C in a HWCVD system and must have an optimal mechanical stability at a high current input. Based on their extraordinary properties, transition metal elements are ideal candidates for the use of filaments in HWCVD. Tungsten and tantalum have proven to be preferred candidates for the use of a filament in HWCVD [1.26 - 1.30]. Table 1.1 displays some of the properties of these remarkable metals [1.28 – 1.32].

Table 1.1:   *Selected properties of Ta and W [1.28 - 1.32]*

Metal	Melting point (℃)	Vickers Micro-hardness (kgmm^{-2})	Modulus of elasticity (GPa)	Resistivity μΩcm (at 25 ℃)
Tungsten	3396	400	345	5.28
Tantalum	3076	110	186	12.5

The melting points of these metals are in excess of 3000 ℃, which is more than sufficient for HWCVD and their hardness is amongst the highest of metals. However, in some cases the precursor gases react with the filament and consequently influence its catalytic effect during the HWCVD process. In the special case where W- and Ta-filaments are in a CH$_4$ containing atmosphere, a reaction occurs between the filaments and carbon in the gas phase. This reaction is called carburization and it changes the structure and hence the properties of the filament during the deposition. These changes result in an unstable deposition process, which will ultimately play a negative role in scaling up HWCVD for mass-production of CNTs.

1.6 Carburization overview

There are two rate-determining steps during carburization: an initial surface controlling step and a later diffusion-controlling step [1.33]. Studying the thickness of the carbide layer as a function of time provides a differentiation between the two rate determining steps. A linear graph implies that the supply of carbon via the catalytic dissociation of the carbon containing gas on the surface of the filament is the slowest step in the reaction. Parabolic growth behaviour suggests diffusion of carbon into the metal is the slowest step in the reaction. Tables 1.2 and 1.3 summarize the previous carburization results for Ta- and W-filaments in CH$_4$ diluted in H$_2$, respectively.

Table 1.2:   *Previous carburization results for Ta-filaments. T_{fil} denotes the filament-temperature*

Filament diameter	Pressure (Torr)	CH$_4$ dilution	Carburization time	Phases formed	T_{fil} and Resistance	Author/s and year of publication
0.5mm	30	5 %	0.5 and 1 hr	Ta$_2$C+TaC	2200 °C	Matsubara et al. [1.29], 1990
			2 hrs	TaC		
0.5 mm	30	0.5 %	22 minutes	Ta$_2$C+TaC	2500 °C	Tsutsumoto [1.27], 1998
			60 minutes	TaC	0.70 Ω	
		1 %	14 minutes	Ta$_2$C+TaC		
			30 minutes	TaC	0.65 Ω	
		3%	14 minutes	Ta$_2$C+TaC		
			25 minutes	TaC	0.60 Ω	
0.8 mm	10	1%	30-60 hrs	Ta$_2$C+TaC	2200 °C	
			> 60 hrs	TaC		
0.8 mm, 500 mm long	10	0.5 and 1 %	5 and 24 hrs	Ta$_2$C+TaC+Ta	2000 °C, 0.8 Ω	Okoli et al. [1.38], 1990
	40	1 %	24 hrs	C+Ta$_2$C+TaC+Ta	2200 °C	
			64 hrs	Ta$_2$C+TaC		
			5 hrs	Ta$_2$C+TaC+Ta	2400 °C, 1.3 Ω	
			24 hrs	TaC		

Table 1.3:   *Previously reported carburization results for W-filaments*

Filament dimension	Pressure (Torr)	CH$_4$ dilution	Carburization time	Phases formed	T_{fil} and Resistance	Author/s and year of publication
Not given	30	0.5 %	12 minutes	α-W$_2$C	1700 °C, 1.4 Ω	Moustakas [1.30], 1989
0.5 mm diameter	30	5 %	2 hrs	W$_2$C+WC	2200 °C	Matsubara et al. [1.29], 1990
			4 hrs	WC		
0.8 mm diameter, 500 mm long	10	0.5 and 1 %	5 hrs	W$_2$C+WC+W	2000 °C	Okoli et al. [1.38], 1990
0.6 mm diameter, 120 mm long	22.5	1 %	5 hrs	WC	1600 °C, 0.2 Ω	Kromka et al. [1.35], 2001
0.5 mm diameter, 112 mm long	22.5	1 %	1 hr	High intensity of W$_2$C+ low intensity of WC	2450 °C, 0.24 Ω	Zeiler et al. [1.36], 2002
			40 hrs	W$_2$C+WC		

1.7   Structural properties of a carburized filament

The structure of a filament changes during carburization due to a metal transforming into its carbide via the incorporation of carbon into the lattice of the metal. Consequently, the properties of a filament change during carburization. Carburization influences important properties of the filament such as its catalytic characteristics, thermal radiation abilities, strength and electrical resistance. From tables 1.2 and 1.3 it can be seen that carburization is a complex phenomenon that depend on the process parameters such as the filament used (type, dimensions), pressure, temperature, exposure time and CH_4 dilution. Sections 1.7.1 and 1.7.2 present previous filament carburization results for W- and Ta-filaments, respectively, with discussions on key aspects. Section 1.7.3 will address the formation of solid carbon layers on the filament-surface during carburization.

1.7.1 Tungsten-filaments
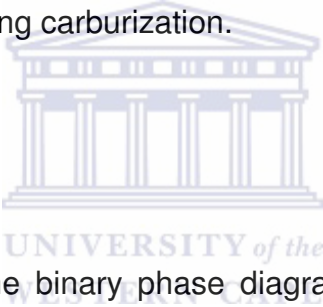
Figure 1.9 shows the binary phase diagram of tungsten and carbon according to Kurlov *et al.* [1.34]. There are two compounds that collectively cover a bigger range of stability below 2726 °C namely: ditungsten carbide (W_2C) and monotungsten carbide (WC). The isolated existence of these phases depends on the atomic percentage carbon (at % C) and the temperature.

The lower tungsten carbide, designated by W_2C, exists in three crystal structures with the same chemical composition (polymorph), the difference lying in the locations of vacancies and carbon atoms in the carbon planes. A low temperature W_2C compound, $\beta'' - W_2C$, exists by itself in the temperature range 1249 - 2096 °C and a carbon concentration range of 29.5 - 32.5 at %. It has a hexagonal structure where the carbon atom planes and the vacancy planes arrange alternatively between W atom planes.
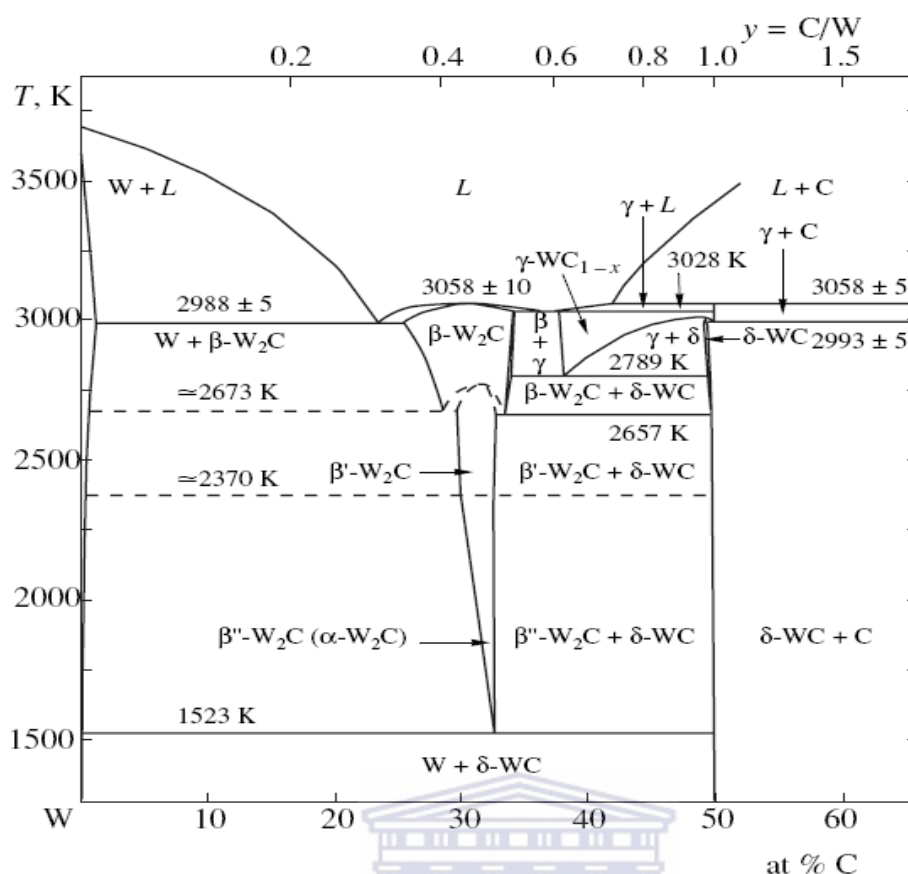
Figure 1.9: *W-C phase diagram showing the different equilibrium carbide compounds as a function of carbon concentration and temperature [1.34]*

The intermediate temperature W_2C compound, β' - W_2C, is the only stable phase between the temperature range of 2096 - 2399 °C and a carbon concentration range of 29.5 - 33.0 at %. This compound has a hexagonal close pack tungsten substructure with an ordered array of carbon atoms and vacancies. In contrast, the high temperature compound W_2C, β - W_2C, is the only stable phase between 2399 - 2784 °C and 28 - 33 at %. It has a hexagonal close pack tungsten structure, but with random positions of carbon atoms and vacancies in each carbon plane. Figure 1.10 is a schematic of the different lattices of the three W_2C polymorphs [1.34].

The major compound, δ - WC, is stable at a carbon concentration of ~50 at % above 1026 °C. δ - WC has a hexagonal structure with carbon and tungsten hexagonal substructures. It is apparent from the W – C phase diagram that C has a high solubility in W.

●- random arrangement of carbon atoms and vacancies ●-carbon atoms □-vacancy sites
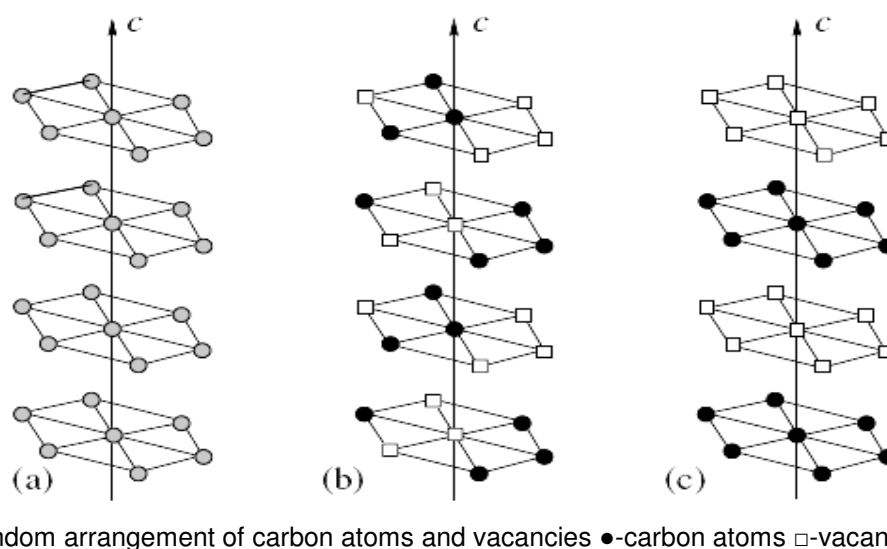
Figure 1.10: *Schematic showing the polymorphs of W_2C: a) β - W_2C, b) β' - W_2C and c) β'' - W_2C [1.34]*

Furthermore, it is also possible that the different tungsten carbide phases can co-exists at some conditions. In the discussion that follows, mostly WC and W_2C compounds formed during the carburization of W-filaments in a CH_4 / H_2 ambient. Moustakas [1.30] reported that large cracks developed along the length of a W-filament carburized in CH_4 [1.30]. These cracks formed due to the incorporation of carbon into the filament. Furthermore, carbonaceous hemispherical deposits appeared on the surface of the filament during the deposition. The formation of these deposits occurred during the adsorption and desorption of carbon during carburization. X-ray diffraction (XRD) patterns revealed that tungsten has been fully converted to β'' - W_2C at these conditions.

Kromka *et al.* [1.35] also subjected W-filaments to CH_4 and observed only WC peaks from the XRD pattern of the filament. In conjunction with SEM analysis, this indicated that the surface of the W-filament was fully carburized after the 5 hrs of treatment. Furthermore, scanning electron microscope (SEM) micrographs of the cross-section of the filament apparently showed that after 2 hrs a WC layer, approximately 120 - 150 μm thick, formed on the perimeter of the W core. The filament-diameter increased to about 0.7 mm due to the formation of micro-cracks.

Recently, a kinetic investigation on the structural changes of W-filaments during the HWCVD of DLC was performed [1.36]. In less than 1 minute and at 2450 °C, XRD spectra revealed the presence of W_2C, which increases in intensity up until 1 hr and then decreases onwards. The WC phase then appeared after 20 minutes and its intensity increased with carburization time. Metallographic cross-sections presented in figure 1.11 [1.36], confirmed the XRD results that a W_2C layer formed on the surface of the W-filament. This layer grew in thickness radially inward and after 70 minutes, there was no W observed.
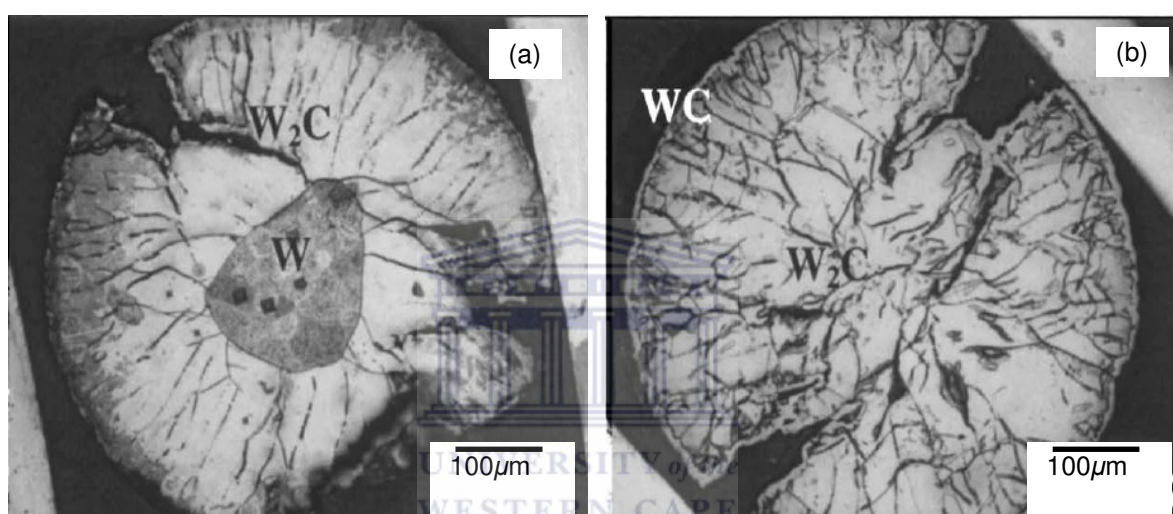
Figure 1.11: *Optical micrographs of a W-filament carburized in CH_4 for: (a) 60 minutes and (b) 70 minutes [1.36]*

The disappearance of the W core occurs simultaneously with the growth of WC from the surface of the filament. Furthermore, the W-filaments showed a network of small cracks. The thickness of the W_2C layer was measured using an optical microscope. Initially, a high growth rate for W_2C is due to the high reactivity of the metal surface. After 1 minute, this rate decreased and remained constant. After the complete transformation of W into W_2C a filament volume increase of 12 % was achieved [1.36]. The activation energy for the growth of the W_2C layer was determined to be 30 kJmol^{-1} from an Arrhenius plot in the temperature range of 2155 - 2445 °C. This energy corresponds to the activation energy needed for the catalytic dissociation of CH_4 on the filament-surface.

On the other hand, the WC layer growth followed a polynomial law and the measured volume increase corresponding to the formation of WC was about 8.6 %. Formation of large cracks on the filament occurred due to its volume expansion during carburization [1.36].

Based on the literature findings, it is clear that carburization of W-filaments occurs in the sequence:

$$W + C \text{ (1600 - 2450 °C)} \longrightarrow W + W_2C \longrightarrow W_2C + WC \longrightarrow WC$$
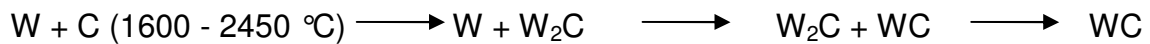
The rate of this sequence increases with increasing temperature up to 2450 °C and a CH_4 dilution of up to 5%. Formation of the carbides proceeds from the surface of the filament, confirming that the initial growth mechanism for W_2C is surface controlled and it is relatively rapid. However, as the thickness of the carbide increases with time, so does the limiting step changes from surface to diffusion controlled. A somewhat slower growth rate for WC occurred, as surface produced carbon atoms had to diffuse through the WC layer to reach the reaction zone at the WC and W_2C interface. The growth of the carbon hemispherical deposits observed in the study [1.30] can be explained based on a mechanism of diamond nucleation growth on refractory carbide substrates described by Lux *et al.* [1.37]. Initially, the dissociation of the C-containing gas results in the formation of carbon atoms that diffuse on the metal-surface or into the metal-matrix. This results in the formation of refractory carbide-metal layers at the appropriate carbon concentration.

Nevertheless, as the carbide layer becomes thicker it becomes increasingly difficult for the carbon atoms to diffuse through the already carbon-occupied carbide layer, resulting in the formation of metastable and subsequently critical carbon clusters on the surface. These clusters then results in the growth of carbonaceous crystalline agglomerates. Nonetheless, if the evaporation of carbon from the surface (desorption) is high the agglomerates do not form a layer that covers the surface. Furthermore, there exist a difference in thermal expansion of the carbon clusters and the surface. Both these processes result in the formation of isolated hemispherical deposits. Figure 1.12 demonstrates this process [1.37].
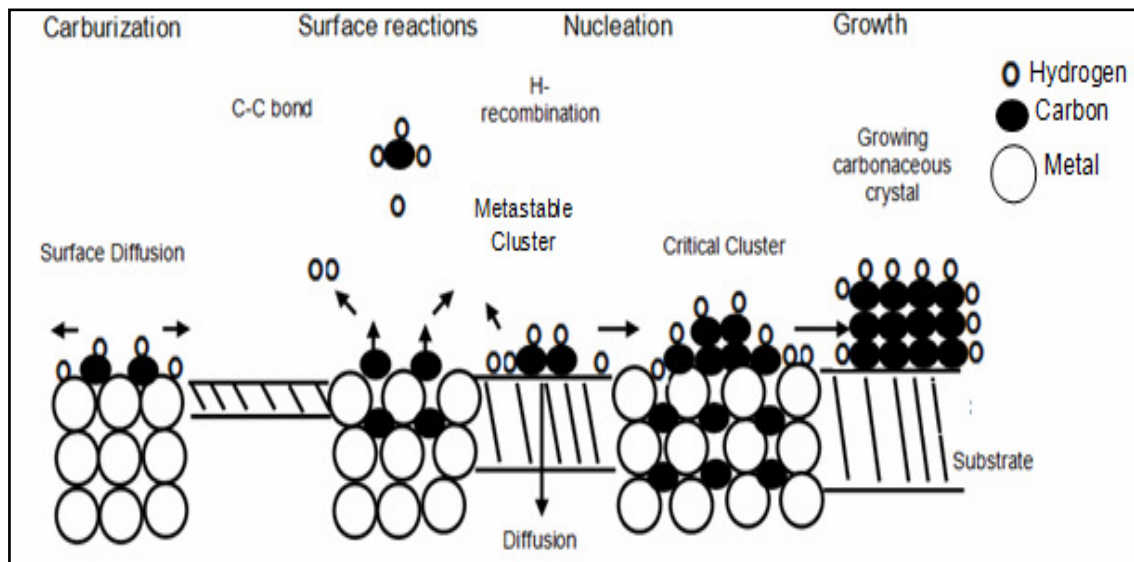
Figure 1.12: *Schematic representation of the nucleation and growth processes of carbon layers on refractory carbide substrates [1.37]*

The formation of cracks is due to the volume expansion that the filament experience during carburization. This volume increase stems from the expansion of the lattice caused by the incorporation of carbon into the metal [1.33]. Consequently, this gives rise to a difference in the densities of tungsten and the tungsten carbide layer. The diffusion of hydrogen into the filament may also contribute to crack formation.

The tungsten carbide layer has a lower density than the inner tungsten layer, which results in formation of stresses in the carbide layer. Compressive stresses establish at the interface of tungsten and tungsten carbide whilst at the outer regions the carbide is under hoop tension. The filament will therefore experience cracking when the outer tensile stresses exceed that of the carbide phase. This ultimately results in the observed brittleness and cracks of the filament after carburization [1.33].

1.7.2 Tantalum-filaments

Figure 1.13 shows the binary phase diagram for Ta and carbon, obtained from the review by E. K. Storms [1.32].
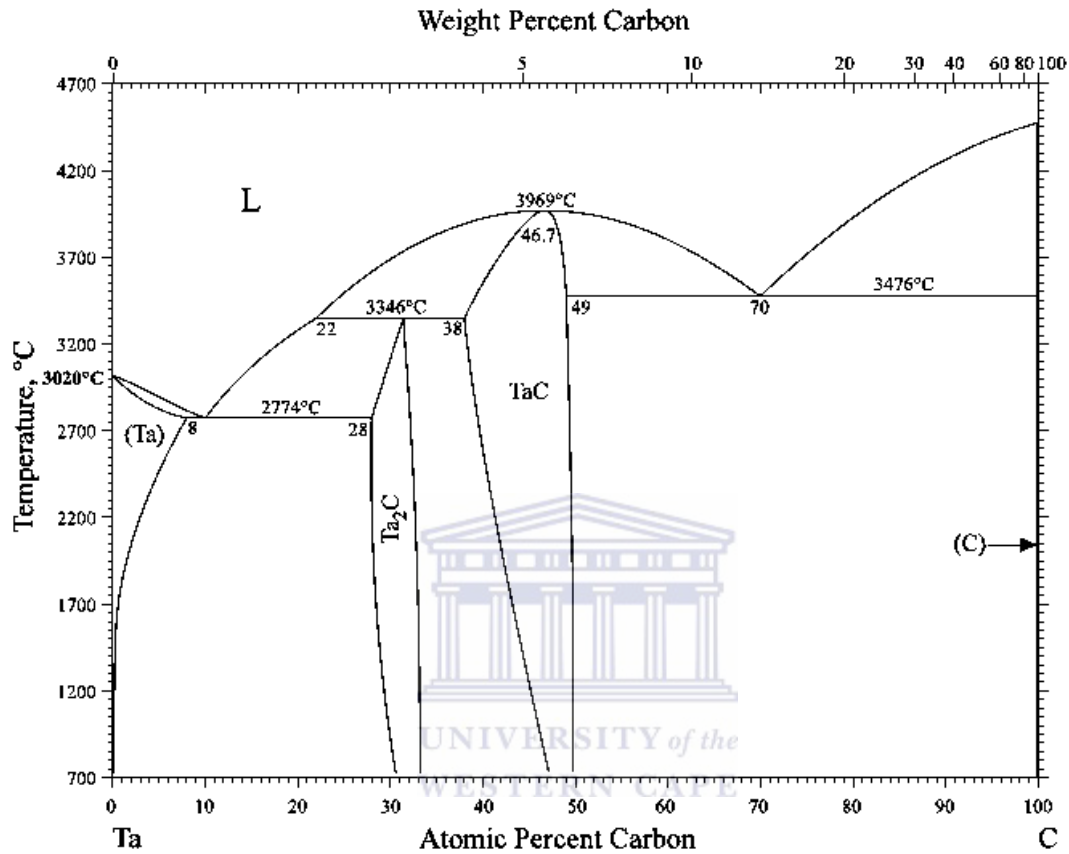
Figure 1.13: *Phase diagram of Ta and carbon [1.32]*

According to figure 1.13, Ta has two carbides namely ditantalum carbide (Ta$_2$C) and monotantalum carbide (TaC). The Ta$_2$C compound exists at 28 - 33 at % C and 699 - 3345 °C. [1.32]. TaC has a cubic close structure with octahedral interstitial sites where carbon atoms are believed to be situated. The possible equilibrium phases that can form when tantalum react with carbon at elevated temperatures are shown in figure 1.13. Similarly to the tungsten carbide phases, carbon has also a high solubility in Ta. Also noticeable is the high melting temperature of TaC (~3965 °C). In the discussion that follows, mostly Ta$_2$C and TaC compounds were found to form during the carburization of Ta-filaments.

Matsubara *et al.* [1.29] reported that a Ta-filament deforms less than a W-filament after 1hr of carburization. They also found, through XRD analysis, that Ta_2C and TaC peaks appear after 0.5 - 1 hr of carburization, whilst only TaC peaks were observed after 4 hrs. Interestingly enough, XRD spectra showed that the TaC peaks shifted slightly to lower diffraction angles for longer durations of carburization time. This means that the lattice parameter of TaC increases with carburization time until full stoichiometric TaC is formed via the increments of carbon.

A SEM micrograph presented in figure 1.14a showed that at 1 hr the internal structure of the Ta-filament consisted of three distinguishable regions: an inner Ta core, an intermediate Ta_2C layer and an enclosing TaC layer [1.29]. At 4 hrs a solid layer of TaC was observed as shown in the SEM micrograph in figure 1.14b. The high resistance of the Ta-filament to deformation during carburization is related to the higher melting temperature of TaC versus that of WC.
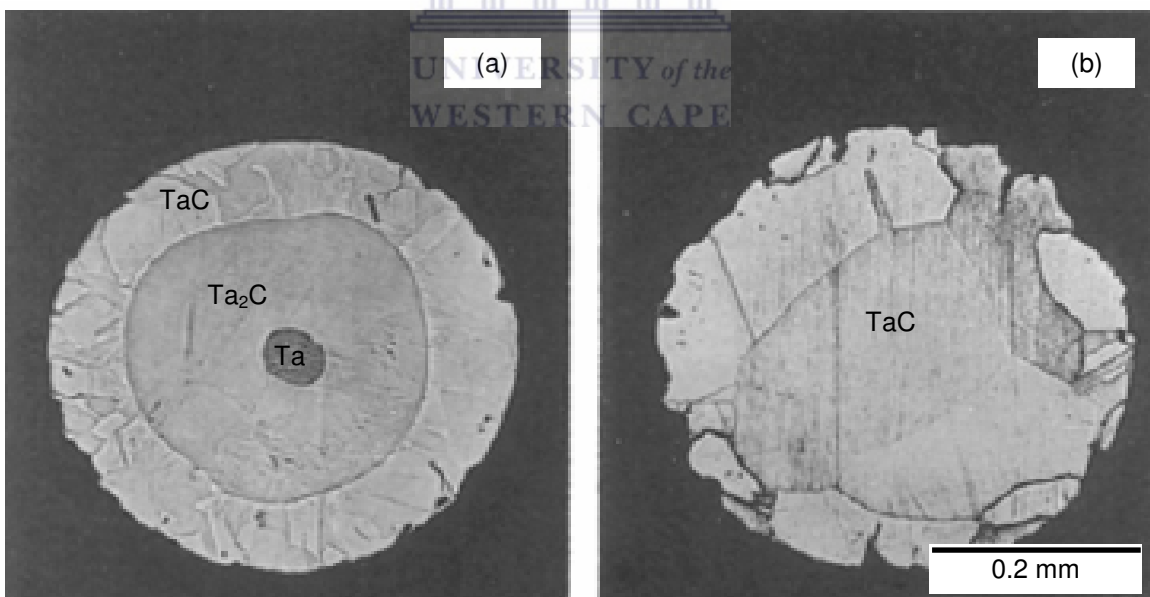
Figure 1.14: *SEM micrographs of cross-sections of a Ta-filament carburized in CH_4 for (a) 1 hr and (b) for 4 hrs [1.29]*

Further insights came from a study by Okoli *et al.* [1.38] on the carburization behaviour of Ta-filaments. Ta-filaments showed remarkable stability for temperatures up to 2400 °C under the same conditions as that for W. After 5 hrs at 2000 °C and 2400 °C, Ta-filaments consisted of TaC, Ta and Ta_2C layers. However, after 24 hrs the filament was fully carburized, consisting of TaC only. An increase in the volumes of the filaments as well as large cracks along the length of the carburized filaments occurred. The carburized Ta-filaments showed a high level of brittleness after cooling.

Tsutsumoto [1.27] investigated the relationship between the filament strength and carburization. XRD patterns showed that Ta, Ta_2C and TaC phases were formed after 10 minutes. As the carburization continued, only the TaC phase was detected. The filament underwent rapid elongation until 30 minutes and saturated around 60 minutes. Saturated values increased slightly with CH_4 dilutions and the net elongation was found to be about 5 %. The diameter of the filament increased by 8 % resulting in a volume increase of 22.5 %. The bending strength of the filament decreased and reached a minimum around 60 minutes for 0.5 % CH_4.

At this time, the filament is very brittle and it corresponds to the time of disappearance of the Ta_2C layer from the filament. However, as carburization continues, a 40 % increase in the strength of the filament (relative to the original strength) occurred. A large crack formed at this stage of carburization. Smaller cracks formed around 30 minutes due to the volume expansion of the filament. These cracks disappeared after 200 minutes due to sintering, which means that the formation and disappearance of the cracks during carburization resulted in the observed behaviour of the filament-strength as a function of carburization time [1.27].

According to literature findings at a given temperature in the range 2000 – 2400 °C, Ta-filaments carburizes in the sequence:

$$Ta + C \longrightarrow Ta + Ta_2C + TaC \longrightarrow Ta_2C + TaC \longrightarrow TaC$$

As is the case for W-filaments, the carburization rate for Ta-filaments increases with decreasing CH_4 dilution and rising temperature. However, Ta-filaments carburize much faster since they have a higher carbon diffusion coefficient, as shown in table 1.4. Previous results presented in table 1.2 clearly show that the carburization rate of Ta-filaments increases more sensitively with temperature, confirming the superior diffusion of carbon in Ta-filaments than their W counterparts.

Table 1.4:   *Diffusion coefficients for carbon in metals and carbides taken from [1.38]*

Phase	Diffusion Coefficient (m^2s^{-1})
Ta	2×10^{-9}
Ta_2C	4×10^{-14}
TaC	2×10^{-14}
W	1×10^{-11}
W_2C	2×10^{-13}
WC	not known

The effect of temperature and CH_4 dilution on the formation of a carbide layer may be deduced from Fick's law of diffusion [1.39]:

$$J = -D\frac{\partial C(x,t)}{\partial x} \qquad (1.6)$$

where J is the flux *($molm^{-2}s^{-1}$)*, t is time, C *($mol^{-1}m^{-3}$)* is the concentration of the solute and x (m) the distance into the filament-lattice. The negative sign indicates that the solute moves from a region with a higher concentration to a region with a lower concentration. D *($m^{-2}s^{-1}$)* is the diffusion coefficient, which depend on temperature T *(K)* via the following relation:

$$D = D_0 exp(-Q/RT) \qquad (1.7)$$

where D_0 is the maximum diffusion coefficient, Q $(Jmol^{-1})$ is the activation energy for diffusion and R $(8.314\ J^{-1}K^{-1}mol^{-1})$ is the universal gas constant. Thus, from equations (1.6) and (1.7) it is apparent that the duration of carburization decreases as the temperature and CH_4 volume concentration increases. However, increasing the CH_4 dilution may result in the formation of carbonaceous phases on the surface of the carburized filament. These carbon phases influence DLC formation and will be discussed in section 1.7.3.

The superior melting point of TaC over WC accounts for the preferred use of Ta-filaments in the case when extreme operating temperatures are desired. Furthermore, the increase in filament strength due to sintering observed by Tsutsumoto [1.27] may result in Ta-filaments having a longer operational life. Table 1.5 tabulates some properties of WC and TaC [1.31]. Ta and W carbides have superior hardness, modulus and resistivities relatively to the metals (compare table 1.1). Additionally, the melting point of WC is lower than W, whilst TaC has a much higher melting temperature than Ta.
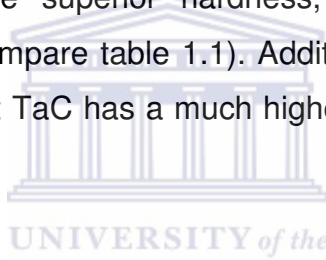
Table 1.5: *Some properties of W- and Ta-carbides [1.31]*

Carbide	Melting point (°C)	Vickers Micro-hardness (kgmm^{-2})	Modulus of elasticity (GPa)	Resistivity µΩcm (at 25 °C)
WC	2796	2200	690	22
TaC	3796	1800	285	20

1.7.3   Carbon layer formation on filaments during carburization

A graphite-like carbon layer forms on the surface of a filament if the incoming flux of carbon atoms is higher than the diffusion of carbon into the filament and the outgoing flux of carbon atoms due to the etching of the carbon layer by atomic hydrogen. Furthermore, carbon layers are more likely to form on W-filaments than Ta-filaments. This is due to the higher carbon diffusion coefficient of Ta compared to W, resulting in a faster diffusion of carbon into the Ta-filament (see table 1.4) [1.40, 1.41]. This ultimately results in the formation of a solid carbon layer on the filament-surface. In the case of DLC deposition, this results in "filament poisoning". The solid carbon layer on the filament-surface prevents direct contact between H_2 and the filament-surface. This results in a lower production rate of atomic hydrogen, which decreases the growth rate and sp^3 character in the DLC thin films grown by the HWCVD technique [1.39].

1.8   Electrical and thermal properties of a carburized filament

The previous section focused on the structural changes of a filament during carburization. This will undoubtedly influence the properties of the filament and ultimately the whole deposition process. Hence, this section covers some aspects concerning the changes in the resistance and thermal properties of the filament as a function of time, CH_4 dilution and temperature. From the changes, it is possible to gain information pertaining to the carburization events of filaments.

1.8.1   Resistance and the duration of carburization

Carburization of Ta and W-filaments results in the formation of carbides that have different properties than their metallic parent phases. Transition metals Ta and W have intrinsic resistivities and the resistance of the filament depends on the characteristic resistivity of the material under investigation.

A change in the resistance will therefore be indicative of the metallurgical changes associated with the carburizing filament. Moustakas [1.30] found that the resistance of a W-filament saturated at a value of 1.4 Ω after 12 minutes, meaning the filament carburization process is complete. On the other hand, Sommer *et al.* [1.40] studied the change in the resistance of W-filaments as a function of temperature. In contrast to Okoli *et al.* [1.38], they observed that the resistance of the filament increased initially and then decreased between 2200 - 2350 °C. They attributed it to the higher deposition pressure used, which should favour the formation of carbon layers on the filament-surface. It was assumed that full filament carburization could be deduced from the time when the resistance of the filament reached a constant value, which was roughly after 1 hr in the conditions of their study.

Kromka *et al.* [1.35] also found an increase in the resistance of W-filaments until it saturates at a value of about 0.2 Ω around 240 minutes. Zeiler *et al.* [1.36] found that the resistance of a W-filament increased rapidly in the first 60 minutes of carburization. This behaviour corresponds to the rise of a metallic resistance with temperature as well as the formation of the W_2C compound. The resistance then saturates at a value of 0.26 Ω up until 800 minutes and subsequently decreases. This decrease was related to the lower resistivity of WC.

Interestingly, the resistance of Ta-filaments at 2000 °C was almost constant whilst the metallographic studies showed that the carburization was still in progress [1.38]. Increasing the temperature of the filament and the CH_4 dilution resulted in differences in measured resistances. At 2000 °C, the resistance of the filament increased slightly and then became constant at about 0.8 Ω between 3 to 6 hrs. At 1 % CH_4 dilution, the resistance decreased after 5 hrs due to the carbon coating on the filament. At 2400 °C, the resistance attained a maximum value of about 1.3 Ω after 4 to 5 hrs of carburization. Remarkably, after 24 hrs the measured resistance decreased to almost the initial value for a pre-carburized Ta-filament.

Similar to Okoli *et al.* [1.38], Tsutsumoto [1.27] reported that the resistance of Ta-filaments increased rapidly, reaches a maximum value after 10 to 20 minutes of exposure and then decreased afterwards to a constant value after 1 hr, in agreement with [1.38]. Contrary to W-filaments, increasing the CH_4 dilution resulted in a higher increasing rate of resistance, decrease of maximum values of resistance and lower final resistance values as shown in table 1.2 [1.27].

It is clear that there are two opposing views on the use of resistance measurements to determine the duration of carburization. On the one hand, resistance versus time measurements showed a saturation curve after complete transformation of Ta- or W-filaments into one of their carbides [1.31 and 1.36] and on the other hand, resistance curves were not corroborating with studies on the cross-section of the filament [1.38]. Judging from the resistance curves, one needs to be sure of the period needed for the measurement. A short duration may only provide information on the duration of carburization associated with the intermediate (W_2C or Ta_2C) stage, as observed by [1.30]. However, the resistance curves should be correlated to XRD and SEM analysis. Moreover, formation of cracks after extensive duration of carburization may ultimately lead to large discrepancy in the resistance values [1.35, 1.38]. The decrease in resistance was attributed to the lower resistivity of TaC compared to Ta_2C and sintering of the cracks [1.27].

1.8.2 Resistance and thickness of carbide layers

Resistance studies enable one to calculate the thickness of the WC carbide layer formed during carburization, as schematically shown in figure 1.15. The unreacted metal core and the surrounding carbide layer act as resistors connected in parallel [1.38]. For resistors connected in parallel the reciprocal of the total resistance R_T is the sum of the reciprocal values of the resistance of the metal core R_W and the carbide layer R_{WC}, as expressed in equation (1.8):

$$\frac{1}{R_T} = \frac{1}{R_W} + \frac{1}{R_{WC}}$$ (1.8)
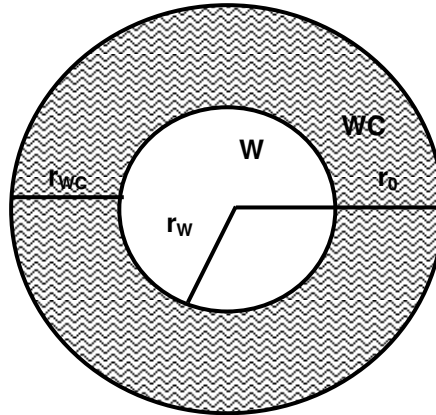
Figure 1.15: *Schematic showing the layers formed during carburization with: the original radius of the filament (r_0), the radius of the unreacted metal core (r_W) and the radius of the carbide (r_{WC})*

The resistances R_W and R_{WC} can be calculated from equations (1.9):

$$R_W = \frac{\rho_W L}{A_W} \text{ and } R_{WC} = \frac{\rho_{WC} L}{A_0 - A_W}$$ (1.9)

where ρ_W and $A_W = \pi(r_0 - r_{WC})^2$ are the resistivity and cross-sectional area of the unreacted metal core respectively, ρ_{WC} is the resistivity of the carbide layer, $A_0 = \pi r_0^2$ is the cross-section area of the original, unreacted filament and L is the length of the filament. By combining equations (1.8) and (1.9), the carbide thickness as a function of R_T is [1.35, 1.38]:

$$r_{WC} = r_0 - \sqrt{r_0^2 - \frac{\rho_{WC} r_0^2}{\rho_{WC} - \rho_W} + \frac{L \rho_{WC} \rho_W}{\pi(\rho_{WC} - \rho_W)R_T}}$$ (1.10)

However, the calculated thickness values of the filament were half than that of the observed values. The discrepancy between the theoretical and experimental values is due to: 1) crack formation, 2) the growth of a WC shell on the W_2C shell and 3) literature values for the resistivities of the different phases are different due to dissolved carbon in each of the phases (W and its

carbides) [1.38]. Furthermore, decreasing the resistivity values for WC resulted in the formation of thicker calculated WC layers after 2 hrs of carburization and the thickness of the WC layers grows initially at the same rate and then saturates for different values of WC resistivity as shown in figure 1.16 [1.35].
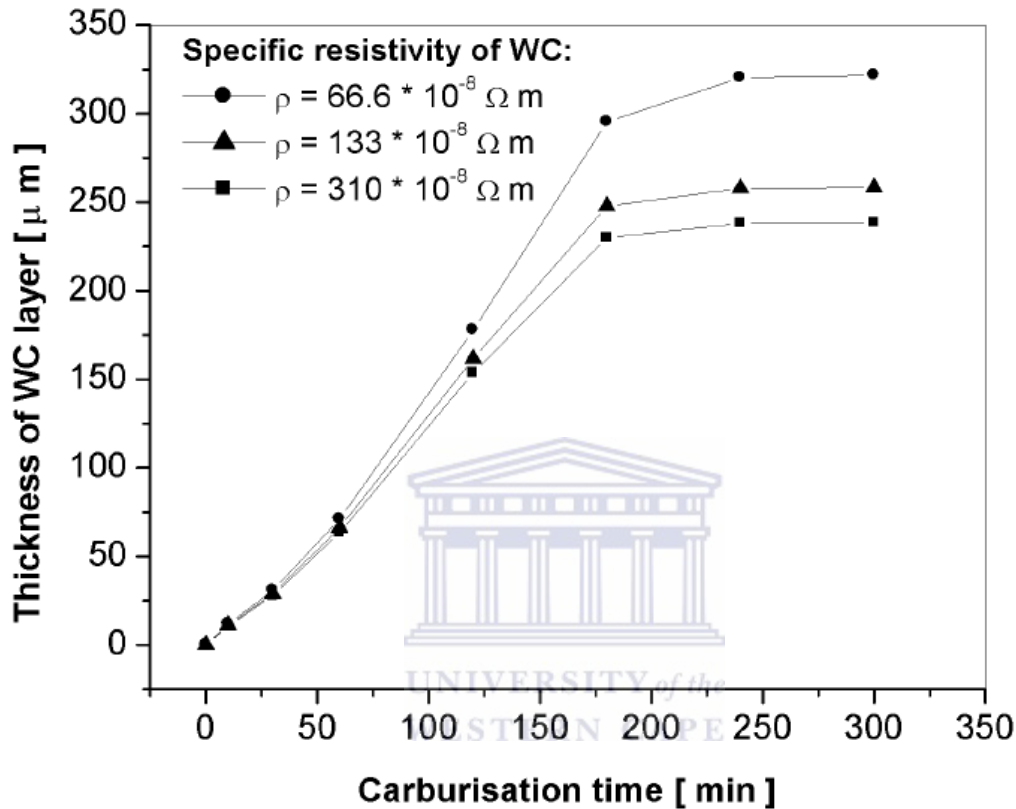
Figure 1.16: *Calculated thicknesses of the WC layer as a function of carburization time at different resistivities [1.35]*

1.8.3 Influence of carburization on the filament-temperature

It was found that the measured temperature of W-filaments decreased by ~200 °C with carburization time [1.38]. The increased area of the filament as well as the effects of different phases with different thermal emissivities and electrical conductivities explained this observation. Furthermore, W-filaments experienced a greater temperature decrease than Ta-filaments. This is due to the higher rate of heat loss via thermal conduction along the electrodes and the higher chances of a solid carbon formation on W-filaments.

In conclusion, filament carburization results in an unstable filament surface and subsequently variations in its properties, such as its temperature, catalytic activity and operational lifetime. Consequently, these changes influence the whole deposition process, which lead to a small window for a stable operation.

1.9   Suggested growth mechanism of carbon nanotubes

As mentioned earlier, the structural properties of the hot-filament change during carburization, which result in an unstable deposition process. The unstable deposition process subsequently influences the sensitive, self-assembly type of growth mechanism of CNTs during HWCVD. In fact, the current drive behind the synthesis of CNTs is to understand the growth process of these remarkable structures and to subsequently mass-produce them in a less expensive and controlled way.

Two growth mechanisms are the best models to describe CNT growth during CVD; namely root growth and tip growth. In root (or extrusion) growth, reactive hydrocarbon species, formed by dissociation of the hydrocarbon gas at the filament or via secondary reactions, are dehydrogenated resulting in the release of carbon. Subsequently carbon becomes soluble and diffuses into the nano-sized islands of transition metal catalysts until supersaturation occurs. Graphene sheets have un-terminated (dangling) bonds at their edges. A tubular form terminates these dangling bonds that results in a lower energy state. The electrons in the pi-bonds are delocalised meaning that the single-walled tube has the ability to conduct electrons either as a semiconductor or as a metal, depending on its diameter. Consequently, carbon precipitates in a tubular, graphitic structure on the catalysts particle that is strongly attached to the substrate. Thus, the diameter of the nano-island catalysts determines the diameter of the CNT [1.42]. This process then continues (resulting in a longer tube) until the catalysts is deactivated.

On the other hand, in tip growth the transition metal catalysts particle detaches itself from the substrate and moves up in the direction of the tube axis, aiding in the addition of carbon atoms from the top of the growing tube. Figure 1.17 schematically demonstrates both growth mechanisms [1.43].
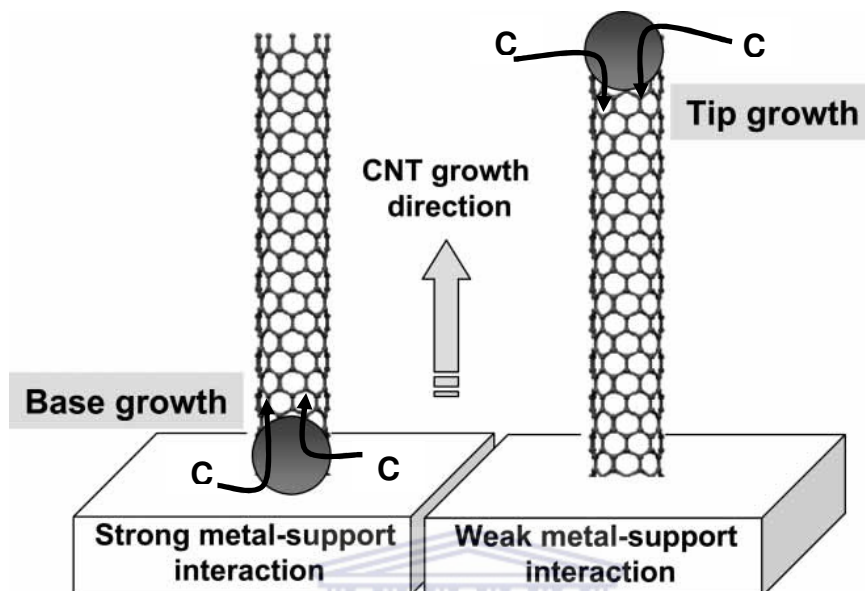
Figure 1.17: *Schematic illustration of the proposed base and tip growth mechanisms of carbon nanotubes [1.43]*

1.10 Kinetic factors during CNT growth and the filament-surface

Due to the sensitive nature of the CNT growth, optimization of the kinetic factors, such as the supply of carbon to the catalysts, the rate of carbon diffusion into the catalyst as well as the carbon precipitation rate on the nano-island catalyst must be understood. The use of transition metal catalysts such as Ni, Co and Fe [1.43] for the synthesis of CNTs therefore comes as no surprise considering the remarkable properties these materials possess. These materials have the ability to dissociate catalytically the reactive hydrocarbon species formed at the filament or via secondary reactions. Furthermore, the high solubility and diffusion rates of carbon, high melting points and their stability at high temperatures render them ideal candidates as catalysts for CNTs synthesis [1.43].

Currently, it is still unclear why CNTs grow at substrate temperatures between 500 - 900 °C, but it may be due to a good compromise of all the aforementioned kinetic factors involve in the growth of CNTs on transition metal substrates [1.43]. In conclusion, during HWCVD the precursor gases dissociates near the filament. Subsequently, the rate of supply of these reactive species from the filament must compromise the other kinetic factors for a stable CNTs deposition. The surface and temperature of the filament therefore play crucial roles during the deposition process.

1.11 Aims and outline

The HWCVD technique holds the most promise as a technique to be scaled-up for mass-production of CNTs. However, few articles have dealt with what happens to the filament itself at elevated temperatures when in a CH_4 / H_2 ambient. Furthermore, there are not many reports in literature that dealt with the effect of temperature and structural properties of the filament on the structural properties of CNTs.

The aim of this study will therefore be to study the reactions between the precursor gases and the surface of the transition metal filament as a function of exposure time and filament-temperature at our deposition conditions. Any changes in the morphology and structural properties of the synthesised CNTs as a function of the temperature and structural properties of the filament will be determined using different characterization techniques.

Chapter 1 highlighted the current state of carbon nanotubes research and a review on the current knowledge of filament carburization in a CH_4 / H_2 ambient during HWCVD. Chapter 2 provides a description and the operation of the HWCVD system employed in this study. This chapter will be concluded by discussions regarding the analytical techniques used to study the structural properties and morphology of the carburized filament and the synthesised CNTs.

Chapter 3 focuses on the structural changes of a W-filament after exposure for different periods at various filament-temperatures in a CH_4 / H_2 environment. Chapter 4 investigates the effect of the structural changes and temperature of the filament on the morphology and structural properties of the synthesised CNTs. Finally, a summary on the results presented in chapters 3 and 4 will be given at the end of the thesis.

UNIVERSITY *of the*
WESTERN CAPE

1.12 References

[1.1]   D. D. Ebbing, "General Chemistry", 5th edition, *Houghton Mifflin Co.*, Boston (1996)

[1.2]   H. W. Kroto, J. R. Heath, S. C. O'Brien, R. F. Curl and R. E. Smalley, *Nature*, **318**, 162 (1985)

[1.3]   S. Iijima, *Nature*, **354**, 56 (1991)

[1.4]   G. Dresselhaus, M. S. Dresselhaus and R. Saito, "Physical Properties of Carbon Nanotubes", *Imperial College Pres*, London (1998)

[1.5]   T. W. Odom, J. Huang, P. Kim and C. M. Lieber, *Nature*, **391**, 62 (1998)

[1.6]   H. Hiura, T. W. Ebbesen, and K. Tanigaki, *Adv. Mater.* **7**, 275 (1995)

[1.7]   S. G. Louie, "*Electronic Properties, Junctions, and Defects of Carbon Nanotubes*", taken from "Carbon Nanotubes: Synthesis, Structure, Properties, and Applications" by G. Dresselhaus, M. S. Dresselhaus and P. Avouris, *Springer*, Germany, p 113 (2001)

[1.8]   W. A. de Heer, S. Frank, P. Poncharal, Z. L. Wang, *Science*, **280**, 1744 (1998)

[1.9]   G. Dresselhaus, M. S. Dresselhaus and P. C. Eklund, "Science of fullerenes and Carbon nanotubes", *Academic Pres*, San Diego (1996)

[1.10] P. L. McEuen, P. Kim, L. Shi and A. Majumdar, *Phys. Rev. Lett.,* **87**, 215502-1 (2001)

[1.11] J. P. Salvatat, J. M. Bonard, N. H. Thompson, A. J. Kulik, L. Forró, W. Benoit and L. Zuppiroli, *Appl. Phys. A*, **69**, 255 (1999)

[1.12] Y. Saito and S. Uemura, *Carbon*, **38**, 169 (2000)

[1.13] S. Uemura, Y. Seko, H. Kamogawa, M. Morikawa and T. Shimojo , *ITE Tech. Rep.*, **17**, 31 (1993)

[1.14] Y. Saito, K. Hamaguchi, R. Mizushima, S. Uemura, T. Nagasako, T. Shimojo and J. Yotani, *Applied Surface Science*, **146**, 305 (1999)

[1.15] R. E. Smalley, T. Guo, P. Nikolaev, A. G. Rinzler, D. Tomanek and D. T. Colbert, *J. Phys. Chem.*, **99**, 10694 (1995)

[1.16] Saito Y, *Carbon*, **33**, 979 (1995)

[1.17] M. José-Yacamán, M. Miki-Yoshida, L. Rendón and J. G. Santiesteban, *Appl. Phys. Lett.*, **62**, 657 (1993)

[1.18] J-E Bourée, C. S. Cojocaru, D. Kim and D. Pribat, *Thin Solid Films*, **501**, 227 (2006)

[1.19] S. Maruyama, Y. Murakami, Y. Miyauchi and S. Chiashi, *Chemical Physics Letters*, **374**, 53 (2003)

[1.20] N. Sgriccia, L. Zong, S. Zhou, M. C. Hawley, S. Zou and J. Asmussen, "Synthesis of Aligned Carbon Nanotubes by Microwave Plasma Chemical Vapour Deposition", Michigan State University (2005)

[1.21] W. J. Lackey, S. N. Bondi, R. W. Johnson, X. Wang and Z. L. Wang, *Carbon*, **44**, 1393 (2006)

[1.22] H. Wiesemann, A. Ghosh, T. McMahon and M. Strongin, *J. Appl. Phys.,* **50**, 3752 (1979)

[1.23] S. Matsumoto, Y. Sato, M. Tsutsumi and N. Setaka, *J. Mater. Sci.*, **17**, 3106 (1982)

[1.24] E. Salernitano, T. D. Makris, R. Giorgi, N. Lisi, L. Pilloni, F. Sarto and M. Alvisi, *Diamond and Related Materials*, **13**, 305 (2004)

[1.25] A.C. Dillon, A.H. Mahan, J. L. Alleman, M. J. Heben, P.A. Parilla and K.M. Jones, *Thin Solid Films*, **430**, 292 (2003)

[1.26] J. Bonard, *Thin Solid Films*, **501**, 8 (2006)

[1.27] T. Tsutsumoto, *Thin Solid Films*, **317**, 371 (1998)

[1.28] J. Yehoda, "*Thermally Assisted (Hot-Filament) Deposition of Diamond*", taken from "Diamond Films Handbook" edited by J. Asmussen and D. Reinhard, *Marcel Dekker*, p 119 (2002)

[1.29] H. Matsubara and T. Sakuma, *Journal of Material Science*, **25**, 4472 (1990)

[1.30] T. D. Moustakas, *Solid State Ionics*, **32-33**, 861 (1989)

[1.31] S. T. Oyama, "The Chemistry of Transition Metal Carbides and Nitrides", *Chapman & Hall*, Great Britain (1996)

[1.32] E. K. Storms, "The Refractory carbides", **2**, *Academic Press Inc.*, New York and London (1967)

[1.33] C. F. Davidson, G. B. Alexander and M. E. Wadsworth, *Metallurgical Transactions A*, **10A**, 1059 (1979)

[1.34] A. S. Kurlov and A. I. Gusev, *Inorganic Materials*, **42**, 121 (2006)

[1.35] A. Kromka, J. Janík, A. Šatka, J. Pavlov and I. Červeň, *Acta Physica Slovaca*, **51**, 359 (2001)

[1.36] S. Schwarz, E. Zeiler, S. M. Rosiwal and R. F. Singer, *Materials Science and Engineering A*, **335**, 236 (2002)

[1.37] B. Lux and R. Haubner, *"Nucleation and Growth of Low-Pressure Diamond"* In "Diamond and Diamond-like films and coating" by J C Angiis, R. E. Clausing, L.L Honon and P. Koidl, *Plenum Press*, New York, p 579 (1991)

[1.38] S. Okoli, R. Haubner and B. Lux, *Surface and Coatings Technology*, **47**, 585 (1991)

[1.39] G.F. Zhang and V. Buck, *Surface and Coatings Technology*, **160**, 14 (2002)

[1.40] M. Sommer and F. W. Smith, *J. Mater. Res.*, **511**, 2433 (1990)

[1.41] M. Sommer, K. Mui and F. W. Smith, *Solid State Communications*, **69**, 775 (1989)

[1.42] H. Dai, "*Nanotube Growth and Characterization*", taken from "Carbon Nanotubes: Synthesis, Structure, Properties, and Applications" edited by G. Dresselhaus, M. S. Dresselhaus and P. Avouris, *Springer,* Germany, p 29 (2001)

[1.43] E. Lamouroux, P. Serp and P. Kalck, *Catalysis Reviews,* **49**, 341 (2007)
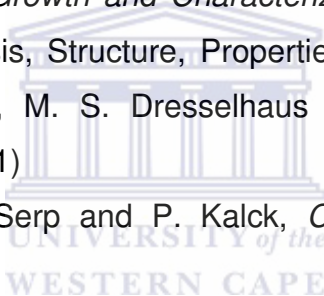
CHAPTER TWO

EXPERIMENTAL TECHNIQUES

2.1   Introduction

This chapter provides a description of the hot-wire chemical vapour deposition (HWCVD) system used in this study and the deposition procedure. A discussion of the analytical techniques used to characterise the structure of carbon nanotubes (CNTs) and the carburization of tungsten (W) filaments concludes the chapter.

2.2   Sample preparation

2.2.1   The Hot-Wire CVD System

The quartz tube-based HWCVD system was designed and built at the Council for Scientific and Industrial Research (CSIR). This highly versatile deposition system, intended to be an experimental system for the deposition of CNTs, can also be used to synthesise materials such as diamond-like carbon (DLC) and some polymers.

The system, schematically shown in figure 2.1, consists of a quartz tube (inner diameter 28.64 mm and outer diameter 32mm) and is capable of achieving pre-deposition pressures of 10^{-3} Torr when pumped down with an Adixen ACP 28 dry pump, capable of a pumping speed of 28 m^3h^{-1}. Extending into the quartz tube are stainless steel electrical contacts for supplying electrical power to the filament from a Kenwood Texio dc-power supply with a maximum current output of 20 A.
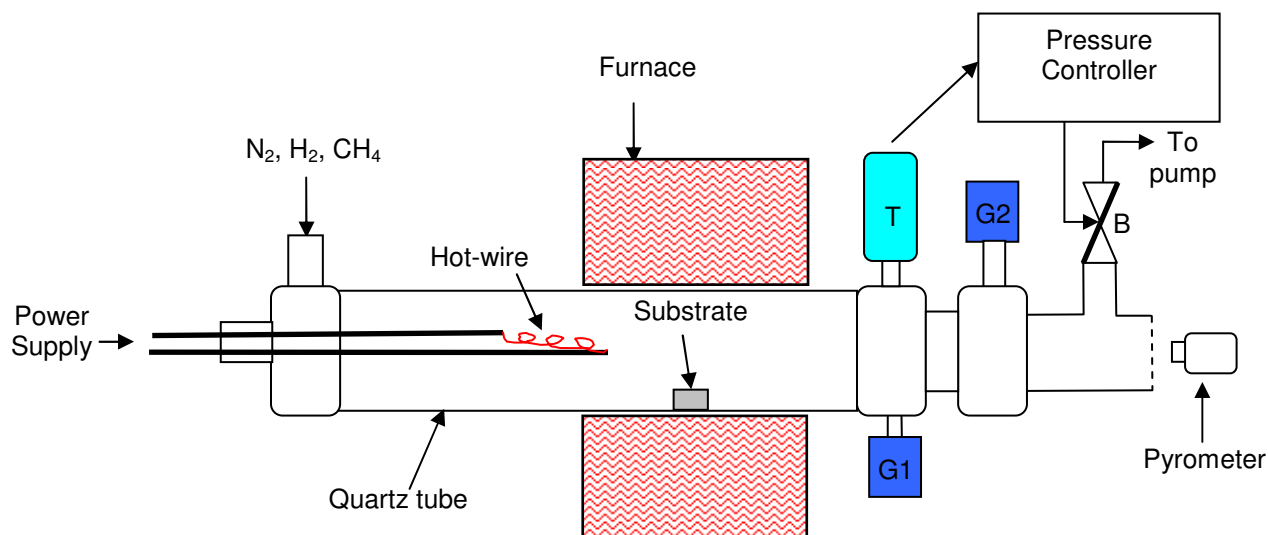
Figure 2.1: *Schematic diagram showing the quartz tube based HWCVD used in the current study. The symbols are discussed in the text.*

During the deposition of CNTs, the tube was enclosed by an electrical furnace with a K-type thermocouple, capable of measuring temperatures below 1000 °C. A Raytek two-colour pyrometer, located approximately 1.5 m away from the filament, was used to measure the temperature of the filament. This type of pyrometer is capable of measuring temperatures between 1000 - 3000 °C with an error of 0.75 % and a resolution of 1 °C.

A RIBER ionization gauge (G1), capable of measuring pressures between 7.5×10^{-3} Torr and 750 Torr, was used to measure the pre-deposition pressure. However, another pressure gauge (G2), capable of measuring pressures between 750×10^{-3} Torr and 750 Torr more accurately, was employed to measure the deposition pressure.

The deposition pressure was controlled using a pressure regulating system capable of controlling pressures between 10^{-4} to 760 Torr. It consists of a MKS type 651C controlling unit, a MKS Type 253B throttling valve (B) and a MKS Baratron type 722A absolute pressure transducer (T).

The pressure regulating system operates via a loop initiated by using the transducer to measure the pressure inside the quartz tube. The transducer sends an electrical signal, with a value proportional to the pressure inside the quartz tube, to the controlling unit. Subsequently, the unit opens and closes the valve until the user defined deposition pressure set point is reached and maintained. Figure 2.2 presents a photograph of the HWCVD system with the filament operating at 10 A and at the pre-deposition pressure prior to the experiments.
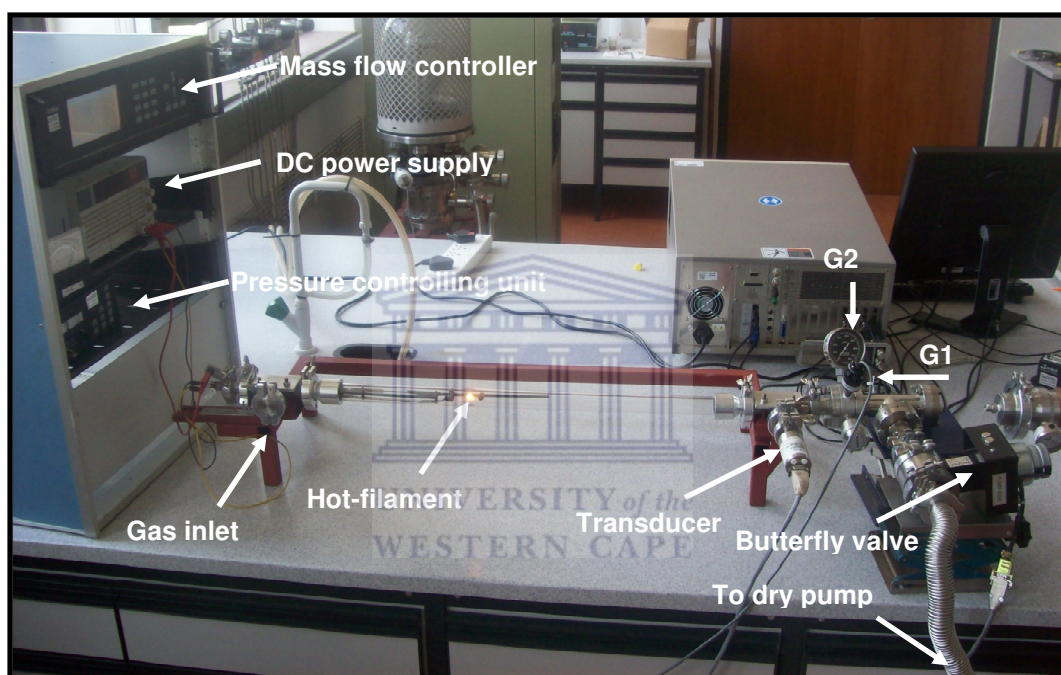
Figure 2.2:   *Photograph showing the various components of the HWCVD system in action, without the furnace and substrate*

2.2.2 Gas supply

Different gases supplied to the system comprise of the reaction gases methane (CH_4) and hydrogen (H_2), as well as the purging gas nitrogen (N_2). A gas supply network consisting of cylinders, gas lines, manual valves, non-return valves, mass flow controllers, a common inlet and an exhaust, supplies the gases to the system. Figure 2.3 shows a schematic representing the gas supply network.
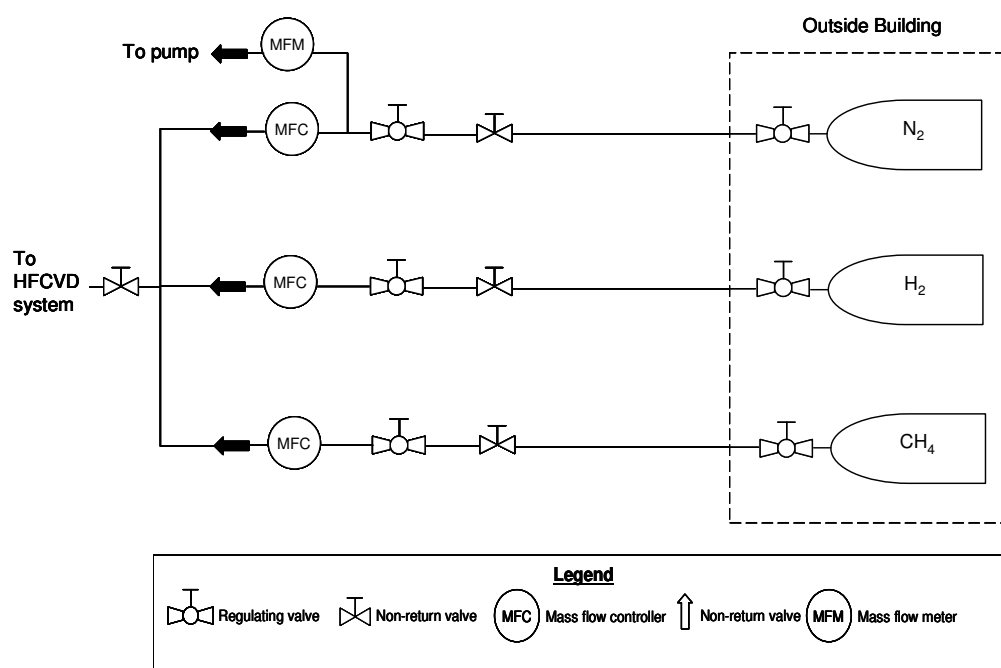
Figure 2.3: *Schematic diagram showing the gas supply network to the HWCVD system*

The pressure at which these gases exit the cylinders is controlled by regulating valves. Manual and regulating valves control the supply of these gases to the three MKS® mass flow controllers (MFC). The MFCs in turn regulate the flow rate of the gases through the system. An additional mass flow meter (MFM) was used to purge the pump with N_2 to eliminate any trace of residual gases trapped inside the pump. An exhaust, pumped by the Adixen® dry pump, draws the gases outside the building.

2.2.3 Filament current-temperature calibration

During the deposition, precursor gases dissociate in the vicinity of a transition metal filament, such as a tungsten (W) filament. The generation and supply rates of the reactive species for the deposition process are determined by the filament-temperature, which is controlled by passing a constant dc-current through it. Calibration of the filament-temperature to the applied current was performed at a pressure of 30×10^{-3} Torr using the pyrometer and the plot is presented in figure 2.4.
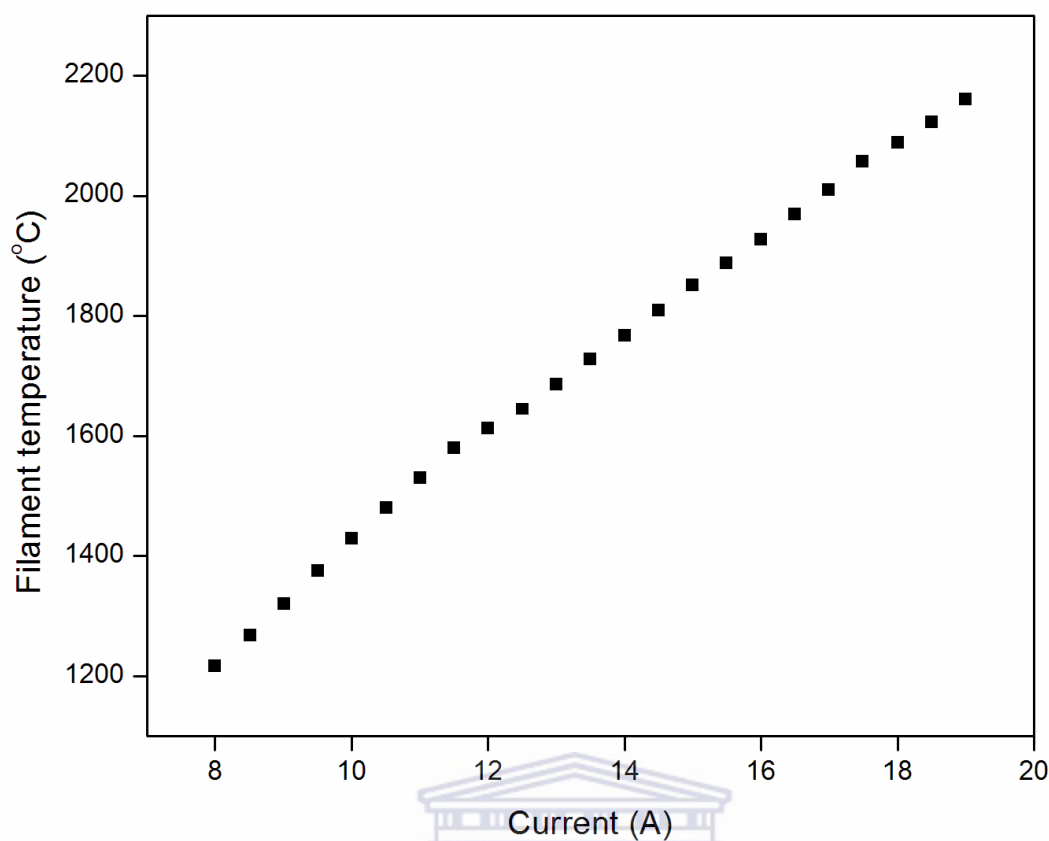
Figure 2.4: *Calibration plot of the filament-temperature to the applied electrical current in vacuum*

It is clear from figure 2.4 that the filament-temperature increases monotonically with the current. However, the power supply to the filament needs to be increased when operating in a CH_4 / H_2 environment in order to compensate for the expected cooling effect of the gases.

2.2.4   The deposition procedure

2.2.4.1   Filament Carburization

W-filaments were used to dissociate CH_4 and H_2 precursor gases during the HWCVD of CNTs. Pure W-filaments (99.95% W), with a diameter of 0.5 mm and a length of 350 mm, were coiled and cleaned ultrasonically for 5 minutes in acetone. The filaments were allowed to dry then attached between the electrical contacts. Subsequently, the ensemble was inserted into the quartz tube.

After the system reached the pre-deposition pressure, the filaments were heated to for approximately 2 minutes in order to evaporate any contamination on the surface brought about by the preparation of the filament. The current input to the filaments was then set to a value of zero. After 5 minutes, the gases were supplied to the MFCs by opening the Hattersley manual valves. Precursor gases CH_4 and H_2 flowed through the system at a constant rate determined by the MFCs. The pressure in the tube was controlled by the pressure regulating system. After stable deposition pressure conditions were obtained, the filaments were resistively heated to the desired temperatures as measured by the two-colour pyrometer. Values of the current, voltage and temperature of the filament were recorded as a function of exposure time. After carburization, the electrical power supply to the filaments was stopped and the MFCs with the MFM were closed. The system was allowed to cool down to room temperature and the filaments were carefully removed.

2.2.4.2   Substrate Preparation

The HWCVD synthesis of CNTs requires the use of suitable transition metal catalysts. In this study, approximately 10 nm nickel (Ni) thin films were deposited on thermally oxidized silicon wafers using electron-beam deposition housed at the iThemba Laboratories in Cape Town. The base pressure in the Bell-jar system was approximately 10^{-7} Torr and increased to 10^{-6} Torr during the deposition. The Ni-deposition rate amounted to 1.7 Å / s.

2.2.4.3   Carbon Nanotube Synthesis

Clean, coiled W-filaments were attached between the electrical contacts and inserted in the quartz tube. The substrate was placed in the middle of the furnace approximately 10 cm away from the middle hottest part of the filament. Subsequently, the HWCVD system was closed and pumped down to the pre-deposition pressure. The filament was then heated to outgas any impurities on the filament-surface. The substrate heater temperature was set to the desired temperature. The precursor CH_4 and H_2 gases were

supplied to the corresponding MFC by opening the Hattersley® manual valves. A constant gas flow rate was maintained in the system by setting the two MFCs to the required flow rates. The deposition pressure was set to a constant value and after stable deposition conditions were attained, the filaments were heated to the required temperature, which signalled the start of the deposition. The present design of the HWCVD system does not allow for a shutter. After the deposition, the power supply to the filament was stop and the Hattersley valves were closed. The furnace temperature was set to 0 °C and N_2 gas at a flow rate of 300 sccm[*] was used to purge the HWCVD system. No nitrides were formed on the filament-surface at these conditions. After the system cooled down to room temperature, the samples were removed and stored away for analysis.

2.2.5 Grinding and polishing procedure

A cross-sectional analysis of the carburized filament is required in order to perform a kinetic study on the filament ageing process. A turn from the middle of the coiled filament was broken off and embedded in a mixture consisting of two parts epoxy powder and one part curing agent. The hardened specimens were then grinded with SiC coated grinding papers using water as a lubricant in a sequence consisting of papers with grit sizes of 150,400, 1200 and 4000. The grinded specimens were then polished with diamond coated polishing sheets using water as a lubricant in the sequence consisting of lapping film coated with diamond particles of sizes 15, 6, 3 and 1 μm. Final polishing was conducted using a 0.5 μm diamond coated lapping film. The specimens were rinsed with ethanol to remove any impurities accumulated during the grinding and polishing phases. After polishing, a turn from the centre of the coiled filament was placed next to its corresponding cross-sectional view using double-sided copper tape. This made it possible to monitor filament-surface as a function of exposure time and temperature.

---

[*] sccm ≡ standard cubic centimetre per minute

1 sccm = $V_m \times 10^{-1}$ $\times 10^{-6}$ m^3/60s ~ 7.440×10^{-7} mol^{-1}

2.3   Analytical techniques

Table 2.1 presents the different characterization techniques utilized in this study as well as the information each one can provide about the filament and the structural properties of the nanotubes.

Table 2.1:   *Analytical techniques used in this study*

Technique	Information	Filament/CNTs	Sensitivity/Analysis depth
Raman spectroscopy	Structure and properties	CNTs	Sensitivity ~ 3 wt%, penetration depth ~ 60 nm in graphite [2.1]
Scanning electron microscope (SEM)	Surface morphology, Elemental analysis	Filament and CNTs	Interaction volume ~ 0.26 - 2.98 µm at 15 kV
X-ray diffraction	Phase formation	Filament	Sensitivity ~5 wt%, penetration depth ~ 17 – 2390 µm

2.3.1   Raman Spectroscopy

2.3.1.1   Introduction

Raman spectroscopy is a non-destructive technique, which requires no sample preparation. When light is incident on a sample it is mainly elastically scattered in random directions; this phenomenon is known as Rayleigh scattering. The remaining fraction of the light has a different energy because it is inelastically scattered and is then referred to as Raman scattering. A Raman scattered photon has an energy related to the characteristic vibrations of a molecule, expressed as the difference between the incoming and the scattered wave's frequency. In the case of carbon nanotubes, Raman spectroscopy provides qualitative and quantitative information on the structure, electronic properties and the extent of homogenous growth of the tubes on the substrate.

2.3.1.2   Theory of Raman scattering

Each molecule vibrates with its own characteristic frequency. It is therefore possible to identify a molecule by irradiating it with radiation of known frequency and measuring the changes of this known frequency. Photons in the incoming beam interact with the molecule in the target sample and distort the electron cloud around its nuclei. This result in the excitation of the molecule to a higher, short-lived energy state called a virtual energy state. These energy states are only activated when the intense beam strikes the molecule.

The molecule can return to its original lower energy state in any of the following three ways. If the molecule de-excites from the virtual energy state to the state in which the molecule was originally in, an elastically scattered photon emerges. This gives rise to Rayleigh scattering, which is energetically favoured since it corresponds to the displacement of the lighter electron cloud about the heavier nuclei [2.2]. Stokes scattering occurs if the molecule de-excites to a vibrational state higher than its original state prior to its interaction with the radiation. This event is accompanied with the conversion of a part of the incident radiation's energy into the creation of a phonon. The scattered radiation consequently has a lower energy related to the vibrational frequency of the molecule [2.3]. On the other hand, anti-Stokes scattering occurs when the molecule de-excites to an energy level lower than its original state. In this case, phonon annihilation occurs. This will result in the emission of a photon with a higher energy than the incident beam. The probability of Raman scattering occurring (1 in 10^6 photons) is relatively weak compared to Rayleigh scattering as it involves the displacement of the much heavier nuclei with respect to the electron cloud of the molecule [2.2]. Stokes scattering lines are much more intense than anti-Stokes lines as most molecules prefer to be in the ground energy states and only a relatively smaller fraction is in vibrational excited states at room temperatures according to the Boltzmann distribution. Figure 2.5 schematically illustrates the three possible scattering events [2.2].
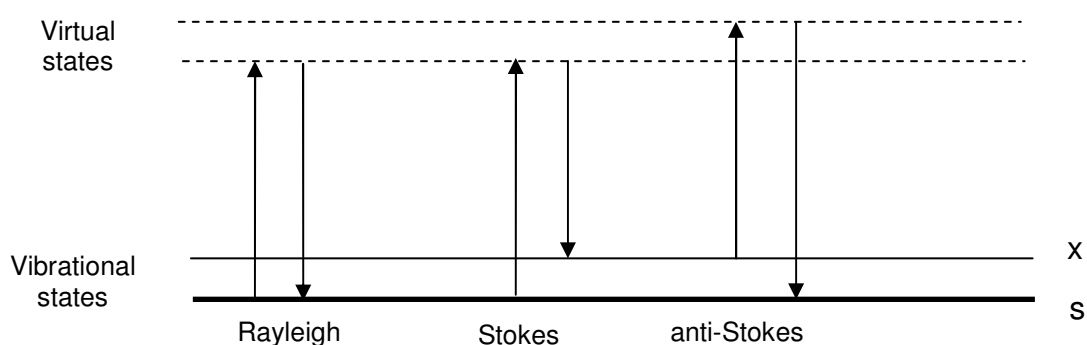
Figure 2.5: *Schematic diagram showing the quantum mechanical description of the possible scattering events accompanying an excited molecule. The x and s levels are vibrational states with different energies [2.2].*

2.3.1.3   Setup of a Raman system

Figure 2.6 shows a schematic diagram of a Raman spectrometer. A focussed UV or visible laser passes through a Fabry-Perot pinhole where its intensity is measured and controlled. Afterwards, the laser is directed by a series of mirrors into the spectrometer and then to a notch filter and a beam splitter. The beam then reflects entirely into the microscope containing the sample. Scattered radiation, collected through the same optics, falls at an angle on the notch filter favouring transmission. A charge-coupled detector (CCD) captures the scattered radiation after it passes through a monochromater (grater). A computer equipped with advanced software displays the digitally acquired information in the form a spectrum [2.2].
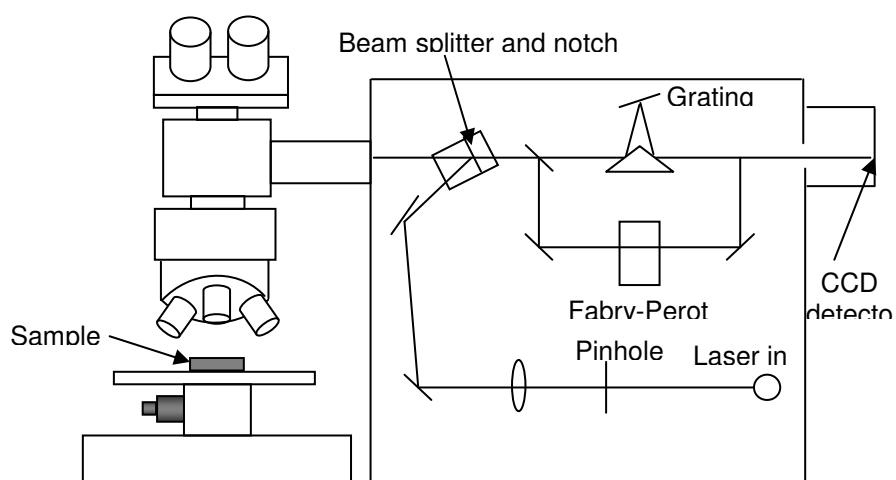
Figure 2.6:   *Schematic diagram of a Raman spectrometer [2.2]*

2.3.1.4   Characterization of carbon nanotubes by Raman spectroscopy

Raman spectroscopy provides a safe, non-destructive and simple way of characterizing CNTs. For CNTs, Raman spectral features corresponding to the radial breathing mode (RBM) and G-band as well as the D- and G' bands are valuable tools in characterizing CNTs. Figure 2.7 shows a typical Raman spectrum of a single-walled carbon nanotube (SWCNT) [2.4].
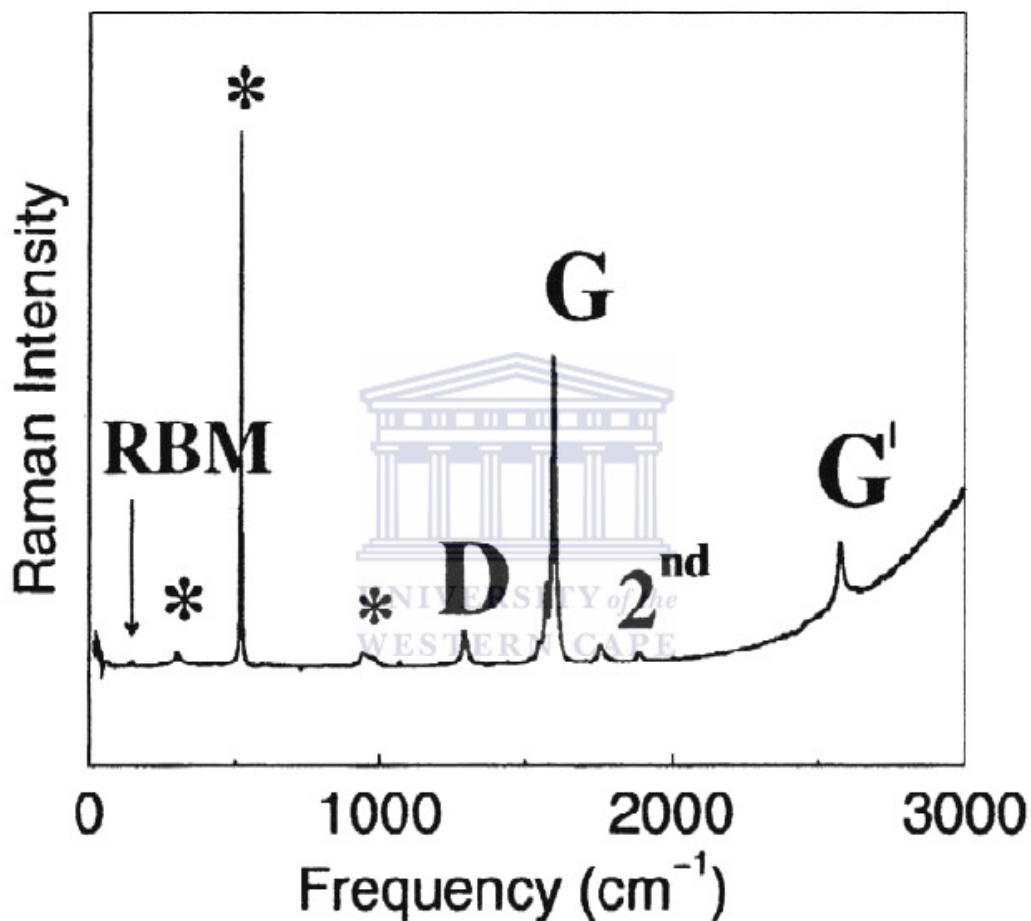
Figure 2.7:   *Raman spectrum of a SWCNT showing the various vibrational modes. The features marked with '*' at 303, 521 and 963 cm-1 are from the silicon-based substrate and are used for calibration of the nanotube Raman spectrum [2.4].*

2.3.1.5   The Radial Breathing Mode (RBM)

The RBM corresponds to the phonon mode resulting from the in-phase vibration of carbon atoms in the radial direction of the carbon nanotube, as shown in figure 2.8. Usually, SWCNTs exhibit this vibrational mode and its frequency, ω_{RBM}, is between 120 - 350 cm^{-1} with diameters in the range of 0.7 - 2 nm [2.6]. The interaction between neighbouring tubes in multi-walled CNTs (MWCNTs) results in the usually observed absence of the RBM signal for this type of CNT. The RBM frequency (ω_{RBM}) may be use to determine the distribution of the diameters (d_t) of a sample containing SWCNTs from the relation in equation (2.1) [2.6]:

$$\omega_{RBM} = \frac{A}{d_t} + B \tag{2.1}$$

where *A* and *B* are experimentally determined parameters. For a bundle of SWCNTs with diameters d_t = *1.5 ± 0.2 nm*, *A = 234 cm^{-1} nm* and *B = 10 cm^{-1}*, which corresponds to an up shift in the RBM due to tube-tube interactions [2.7]. For one SWCNT on a silica substrate it was found that *A = 248 cm^{-1} nm* and *B = 0* [2.7].
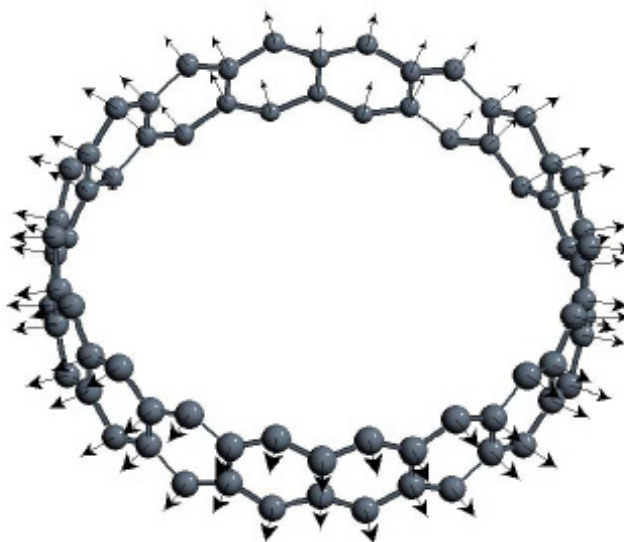
Figure 2.8:   *Schematic representation of the vibrational mode corresponding to the RBM of carbon nanotubes [2.5]*

For a single Raman measurement, the distribution of the SWCNTs diameters calculated through equation (2.1) corresponds to those tubes at the spot irradiated with the incident laser. As a result, one Raman measurement will not give a good approximation of the SWCNTs tube distribution on the entire substrate [2.6]. Moreover, measuring different spots of the sample may be used to determine the homogeneity of the deposited material.

2.3.1.6   G-band

In CNTs, the G-band corresponds to the vibration of the tube along its axial direction, i.e. tangential vibrations of the carbon atoms. Upon close inspection of figure 2.7, for SWCNTs the G-band have two peaks, due to symmetry breaking effects associated with the curvature of a SWCNT, called the G^+ feature at 1590 cm^{-1} and the G^- feature at 1570 cm^{-1}. The G^+ feature corresponds to the in-phase vibrations of the carbon atoms along the nanotubes axis, as shown in figure 2.9. Its frequency, ω_G^+, is independent of d_t and chiral angel θ and is sensitive to the transfer of charge from dopants to SWCNTs: ω_G^+ shifts up for acceptors and shifts down for donors [2.6]. This is of importance for the doping of semiconducting CNTs for device applications.
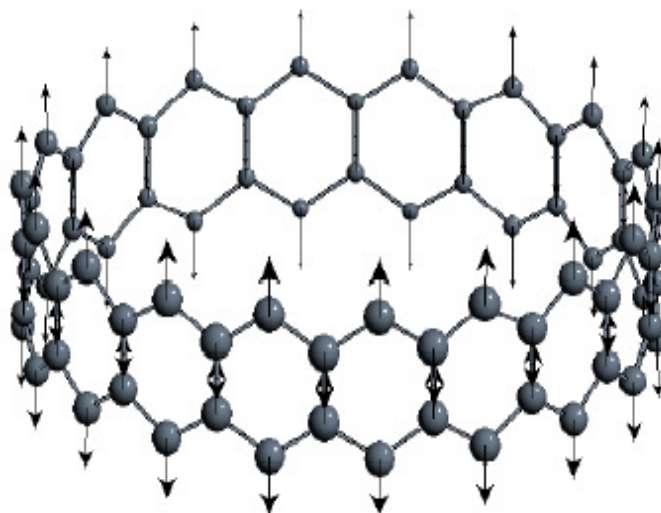
Figure 2.9: *Schematic diagram showing the mode causing the G^+ feature [2.5]*

On the other hand, the G⁻ feature corresponds to the in-phase vibration of carbon atoms along the circumferential direction of the tube, schematically illustrated in figure 2.10 [2.5]. The line-shape of the G-band is sensitive to the electronic properties of the SWCNTs. The G-band of a semiconductor SWCNT is narrow. In contrast, the line-shape of a metallic SWCNT is broad, as shown in figure 2.11 [2.6].
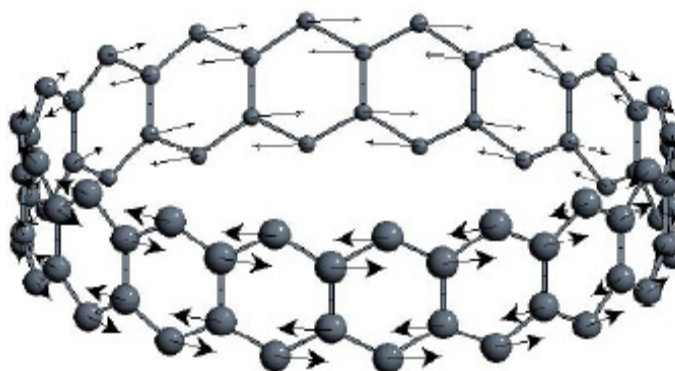
Figure 2.10: *Schematic diagram showing the circumferential vibrational mode associated with the G⁻ feature [2.5]*
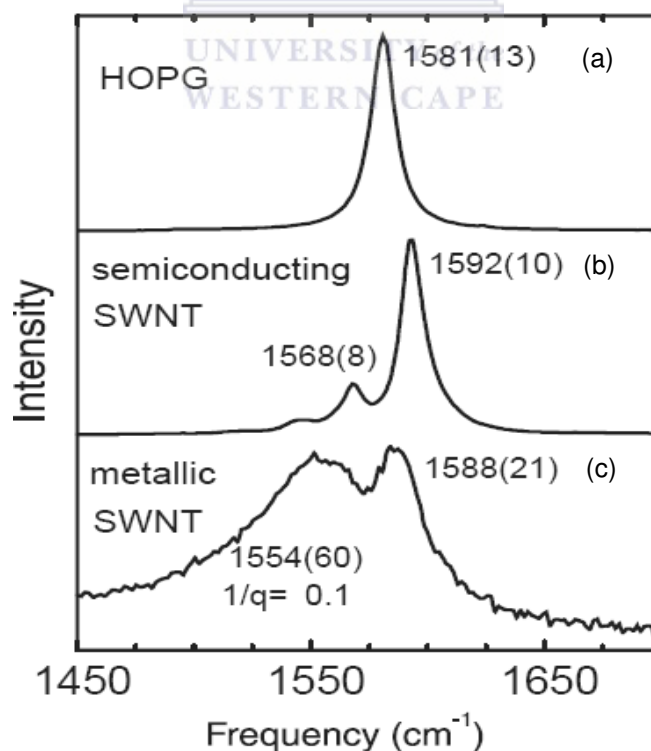
Figure 2.11: *Different line shapes associated with G-band for (a) highly orientated graphite (HOP), (b) semiconductor SWCNT and (c) metallic SWCNT [2.6]*

2.3.1.7   The D-band

The presence of the D-band stems from the disorder-induced mode in graphite and its frequency, ω_D, is spotted between the frequency range 1250 - 1450 cm^{-1} [2.4] for a laser energy in the range 1 - 2.5 eV. As for its graphitic parent structure, the D-band for a CNT is indicative of the amount of disorder in its structure such as heptagons, vacancies, and / or amorphous carbon impurities. In the case of MWCNTs, the D-band is usually present due to the interaction between the multiple walls.

2.3.2 Scanning Electron Microscopy

2.3.2.1   Introduction

The scanning electron microscope (SEM) has been used for information on the structural properties and elemental composition of CNTs and the carburized filament. Figure 2.12 presents a schematic diagram of a SEM. A SEM operates by the heating of a cathode resulting in the emission of electrons. Due to their low work functions and extreme melting points, lanthanum hexaboride (LaB$_6$) or W-filaments are commonly used as a source of electrons.

Electrons emitted via field emission may also be used, with the advantage that the cathode produces a much brighter beam due to the extremely high flux of electrons from an extremely small apparent source. Subsequently, these electrons are accelerated toward a sample-containing anode by an applied voltage. This results in a beam of electrons that eventually moves through a small opening (aperture) in the anode spiralling into the vacuum chamber of the microscope [2.8]. The initial lens influencing the beam-path as it moves through the pole piece is the condenser lens. This lens deflects the beam and thereby focuses it through a focal point above a condenser aperture. The condenser lens as well as the accelerating voltage determines the intensity of the electron beam [2.8].
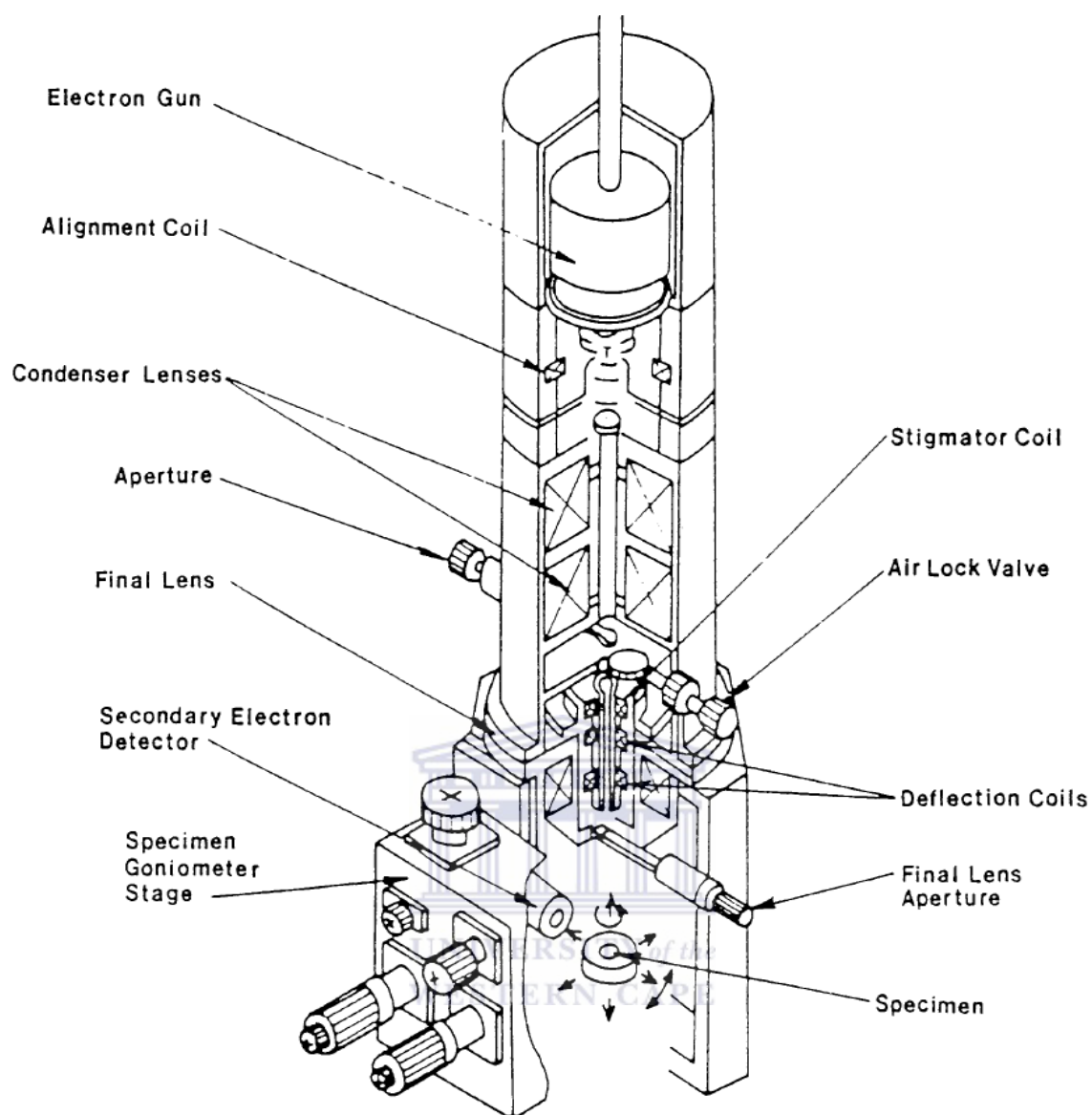
Figure 2.12: *Schematic diagram showing the various parts of a SEM [2.8]*

However, the electron beam diverges again below the condenser aperture. A final objective lens is therefore used to further focus the beam by converging (demagnifying) it to a focal point on the specimen-surface through an objective aperture. The scanning coils then scan the electron beam across an area of the sample. Utilizing positioned detectors, the emitted signals can then be used to form an image of the scanned near-surface area of the sample.

2.3.2.2   Resolution

Resolution refers to the smallest distance at which two objects can be viewed as distinct entities. To understand better the concept of resolution, a simple model of the headlights of an incoming car, that appears to be one spot from a distance, can be used. As the car approaches the two head lights will start to become apparent until both lights can be properly distinguished from each other, as shown in figure 2.13 [2.8].
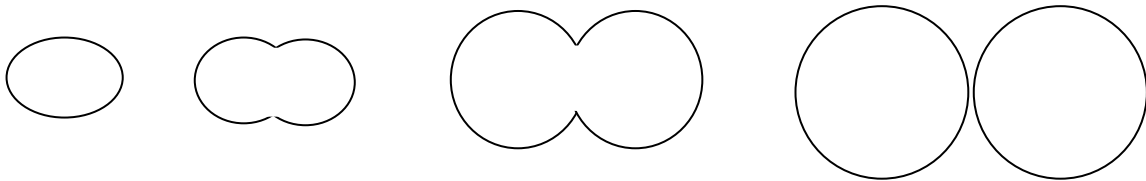
Figure 2.13: *Schematic representation of the concept of resolution using the headlights of an incoming car. From left to right of the sketch: at a far distance the two lights seems as one, but is slowly resolved into distinguishable parts as the car approaches [2.8].*

The resolution of a SEM, d_r, is mathematically express through Abbe's equation (2.2) [2.8]:

$$d_r = \frac{0.61\lambda}{\mu sin\alpha} \tag{2.2}$$

where λ is the wavelength of the electron beam, μ is the index of refraction (usually = 1 for vacuum) and α is the semi-angle that the microscope aperture subtends at the specimen. For a superior resolution the following adjustments can be made: decreasing the aperture size to allow a more focussed electron beam and increasing the accelerating voltage to establish a smaller wavelength according to the De Broglie relation.

2.3.2.3   Depth of field and working distance

The depth of field refers to the range of positions in which structures appear to be in focus. It is adjusted by changing the working distance (WD), i.e. the distance between the final lens and the specimen surface. Increasing the WD value result in a smaller aperture size and consequently a larger depth of field with a lower resolution. On the other hand, decreasing the WD results in an increase in aperture size. Consequently, a decrease in the depth of field occurs, as schematically illustrated in figure 2.14 [2.8].
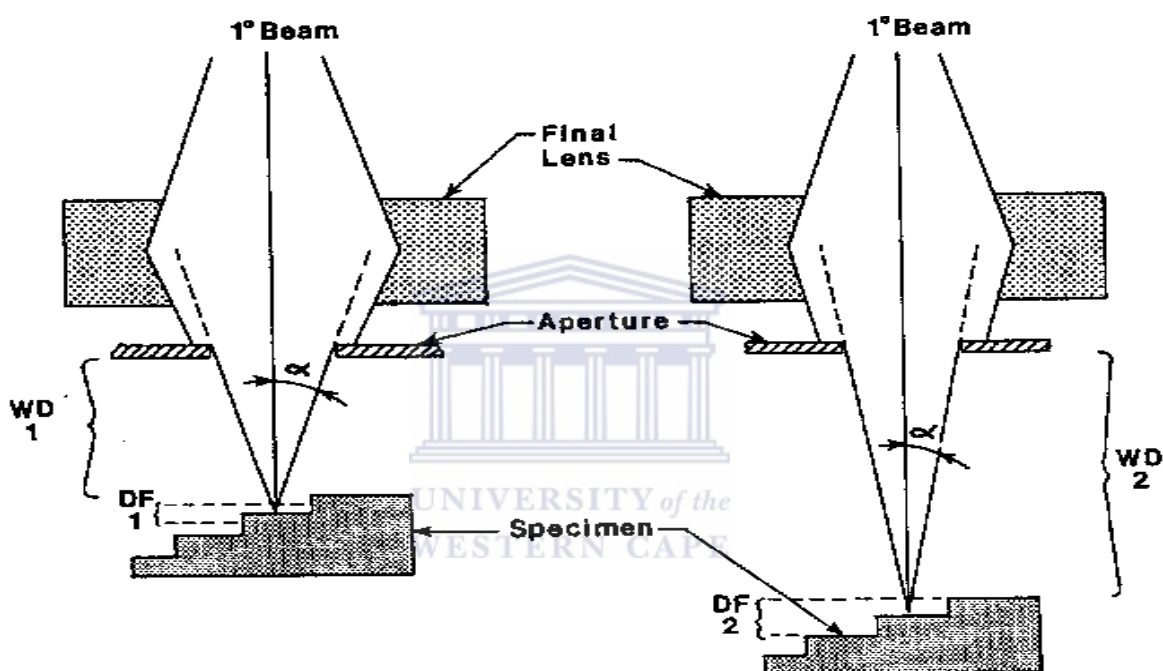
Figure 2.14: *Schematic showing the relationship between working distance, depth of field (DF) and the angle α [2.8]*

2.3.2.4   Signals produced during electron beam-specimen interaction

Figure 2.15 is a schematic representation of the different signals generated during beam-specimen interaction [2.8]. The electrons in the spiralling incident beam are scattered in the sample in a shape resembling that of a pear called the interaction volume, as schematically shown in figure 2.16.
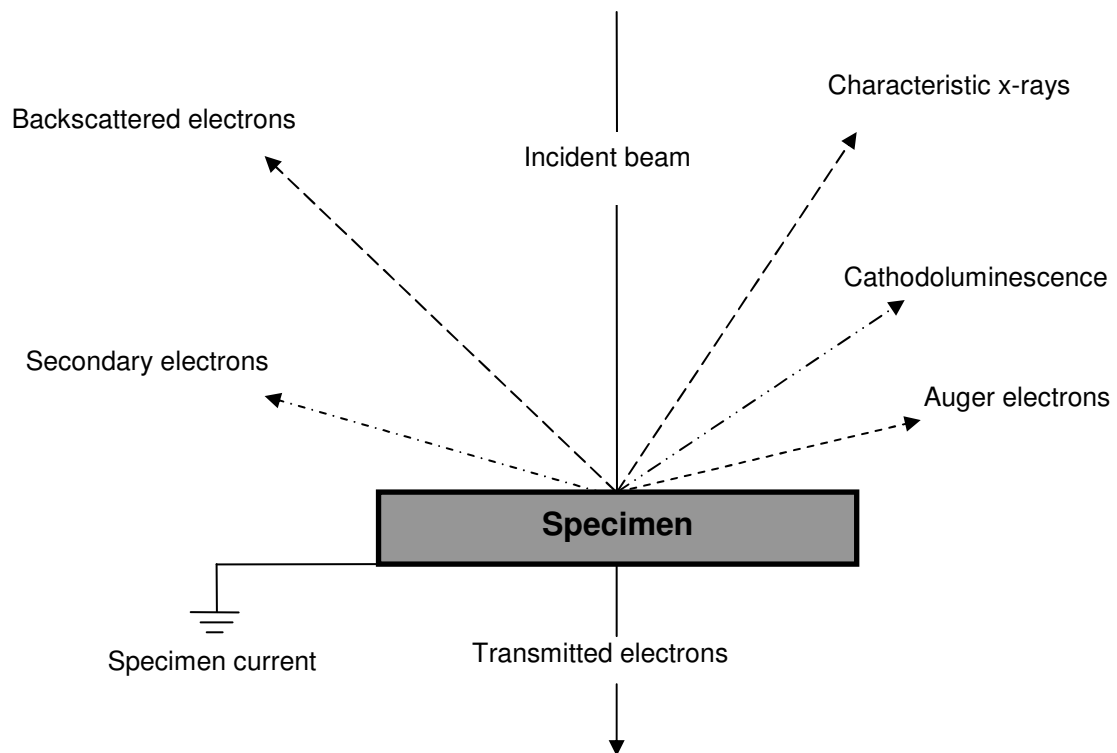
Figure 2.15: *Schematic illustration of the different signals that are produced after the electron beam strikes the sample [2.8]*
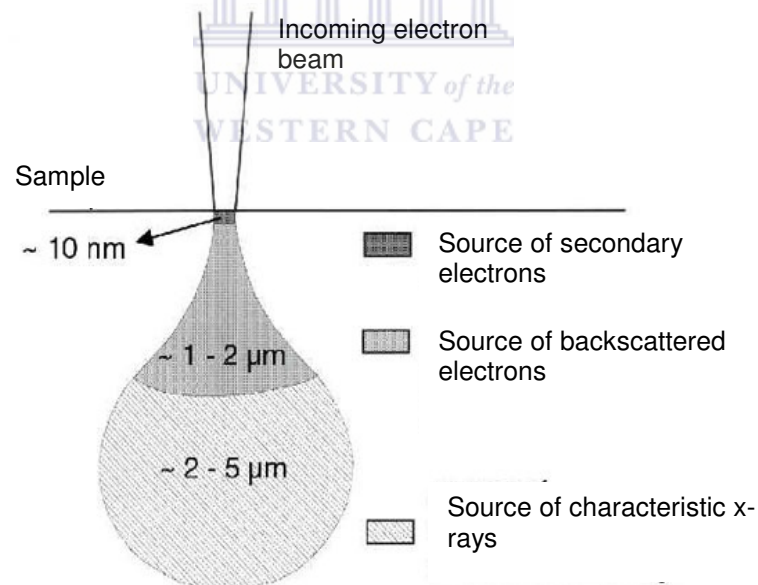
Figure 2.16: *Schematic illustration of the origin of the secondary and backscattered electrons as well as x-rays in the interaction volume [2.8]*

Atoms in this interaction volume are excited and emit signals from different depths of the interaction volume, depending on the energy of each signal. It is possible to perform an elemental or surface analysis, depending on the nature and origin of the emitted signal. The secondary electrons, backscattered electrons, specimen current and the transmitted signals all provide information of the sample-morphology. Information regarding the elemental composition of the specimen is determined by using the characteristic x-ray, cathodoluminescence and the Auger electron signals. For a more detailed description of the generated signals, the reader is referred to the text in reference [2.8].

2.3.2.5   Sputtering preparation

Since an electron beam illuminate the specimen, it is important to use conductive specimens to avoid charging effects that can ultimately lead to the damaging of the SEM and poor image quality. In this regard, non-conductive samples are usually coated with a conductive material (e.g. gold, silver, or carbon) using a sputter coater. During the sputtering, a non-metallic sample is inserted into a vacuum chamber. An inert gas, e.g. argon gas, is then introduced into the system to be ionised by an applied electric field. Positive argon ions are then attracted towards a negatively charged piece of conductive target. These positive ions bombard the surface of the target resulting in the release of its atoms that eventually settle on the surface of the specimen and therefore coat it with a thin, conductive layer [2.8].

2.3.2.6   Characterization of carbon nanotubes and filament carburization

Carbon nanotubes (CNTs) can be grown on a substrate that contains a transition metal catalyst during the hot-wire chemical vapour deposition (HWCVD). As an example, Makris *et al.* [2.9] heated a substrate with silica sandwiched between silicon and a thin layer of Ni. SEM images revealed that the treatment resulted in the formation Ni-nanoparticles having diameters in the range of 5 - 30 nm, as required. Sample preparation requires less effort as

CNTs are conductive and grown on a silicon substrate. In the case of filament carburization, images of the different layers formed on the filament can be viewed using a SEM. Elemental composition at different areas of the metal-carbide layers can be determined using EDS. Thicknesses of the different layers can be approximated using the SEM thus making a kinetic study on the carburization process possible.

2.3.3 X-ray Diffraction

2.3.3.1   Introduction

X-rays are highly energetic electromagnetic waves that have a wavelength in the dimension of Angstroms (10^{-10}), i.e. the same as that of inter-planes distance in a crystal. Consequently, x-rays can undergo diffraction in crystal planes and can therefore be use to study the structure of a material. An ideal crystal is a periodic array of atoms or group of atoms that form planes. An incoming electromagnetic wave sets the electrons of these atoms into an oscillation at the same frequency as that of the incident wave. Subsequently these oscillating electrons scatter x-rays with the same frequency as that of the incident wave.

Constructive interference of x-rays occurs if the Bragg condition is obeyed and is subsequently referred to as x-ray diffraction. Each material has a unique crystal structure related to the periodic arrangement of characteristic atoms that constitutes the crystal thereby allowing quantitative and qualitative material analysis. In this study, XRD will be use to identify the phases formed on the filament during carburization, if crystalline.

2.3.3.2   Geometry of crystals

A point lattice forms by assigning atoms in the crystal to a set of mathematical points called a lattice. The lattice is defined by 3 translation vectors $\vec{a}$, $\vec{b}$ and $\vec{c}$ [2.3] and each point in the lattice has identical surroundings. Figure 2.17 shows a point lattice and its unit cell [2.10].

(a)   (b)
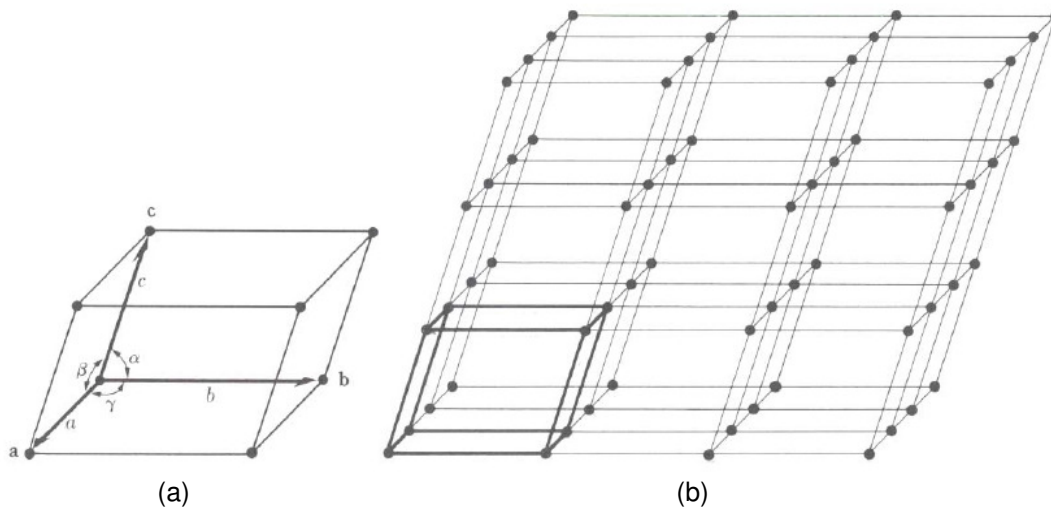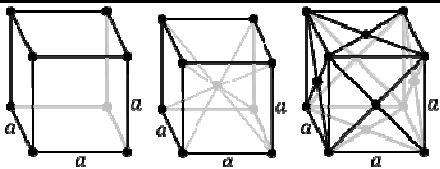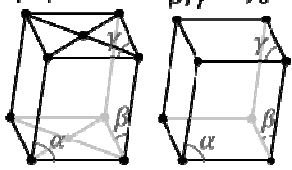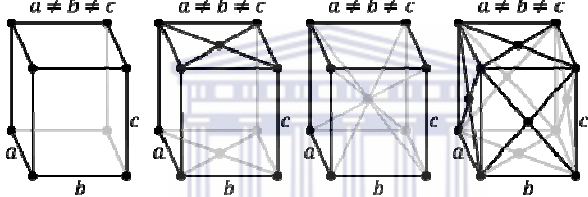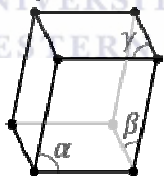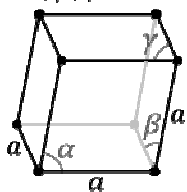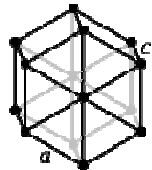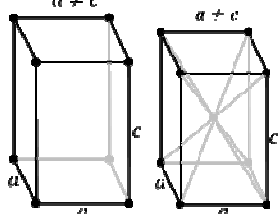
Figure 2.17: *Schematic of: (a) primitive cell and the angles between the translation vectors and (b) its point lattice [2.10]*

Any position in the lattice, $\vec{r}$, can be express as an integral multiple of the translation vectors, as expressed in equation (2.3):

$$\vec{r} = u\vec{a} + v\vec{b} + w\vec{c} \tag{2.3}$$

where *u*, *v* and *w* are integers. Equation (2.3) simplifies by labelling the position in the lattice more compactly as [*u v w*], as illustrated in figure 2.18 [2.10]. Also, shown in figure 2.18 is the norm in choosing the smallest set of integers in representing a crystallographic direction, e.g. the coordinates (1, ½, 0) are represented by [2 1 0] and denoting negative directions with a bar index.

Figure 2.18: *Schematic showing indices of directions [2.10]*

A lattice point group is the collection of symmetry operations (e.g. rotation and mirror reflection) that maintain a fixed point. There are fourteen different lattice types that, when some symmetry operations are performed, remain invariant. These lattices, known as Bravais lattices, are grouped under seven types of cells each being divided into systems according to axial relations that describe the cells. The crystal systems are called triclinic, monoclinic, orthorhombic, tetragonal, cubic, trigonal, and hexagonal. For example, the cubic system contains three lattices: the simple cubic (sc), body-centered cubic (bcc) and the face centered cubic lattice (fcc) [2.3]. Lattice symbols are used to describe a Bravais lattice according to the following assignments: Primitive centering (P), Face centered (F), Body centered (I) or Single face Centered (A, B or C). Table 2.2 tabulates the description of the 14 Bravais lattices [2.10]. The symmetry of crystals results in crystal planes labelled as (h k l), which are an important aspect of diffraction. Planes related by symmetry are called planes of a form denoted by {h k l}. Planes of a form have the same spacing but different indices. For example, the faces of a cube, (1 0 0), (0 1 0), (0 $\bar{1}$ 0), ($\bar{1}$ 0 0), (0 0 1) and (0 0 $\bar{1}$) are planes of the form {1 0 0}. Directions related by symmetry are called directions of a form denoted by <u v w>. For example, the four body diagonals of a cube, [1 1 $\bar{1}$], [1 $\bar{1}$ 1], [1$\bar{1}$ 1] and [$\bar{1}$ 1 1], may all be represented by <1 1 1>.

Table 2.2: *Description of the 14 Bravais lattices [2.10]*

System	Bravais Lattice	Centering
Cubic		P, I and F
Monoclinic	$\alpha \neq 90°$ $\beta, \gamma - 90°$ $\alpha \neq 90°$ $\beta, \gamma = 90°$	P and C
Orthorhombic	$a \neq b \neq c$ $a \neq b \neq c$ $a \neq b \neq c$ $a \neq b \neq c$	P, I, C and F
Triclinic	$\alpha, \beta, \gamma \neq 90°$	P
Rhombohedral	$\alpha, \beta, \gamma \neq 90°$	P
Hexagonal	$a \neq c$	P
Tetragonal	$a \neq c$ $a \div c$	P and I

2.3.3.3   Bragg's description of x-ray diffraction by crystals

W. Bragg presented a powerful explanation for XRD. Consider parallel lattice planes that specularly reflect incident x-rays elastically, i.e. the wave's incident angle is equal to its reflective angle. Suppose that two in phase waves are incident at an angle θ_B on parallel lattice planes spaced d apart, as schematically shown in figure 2.19 [2.10]. The path difference for waves reflected from neighbouring planes is $CB + BD = 2d\sin\theta_B$. The requirement for constructive interference from adjacent planes is that this path difference must be equal to an integral number n of the wavelength λ and is mathematically express in equation (2.4) [2.3]:

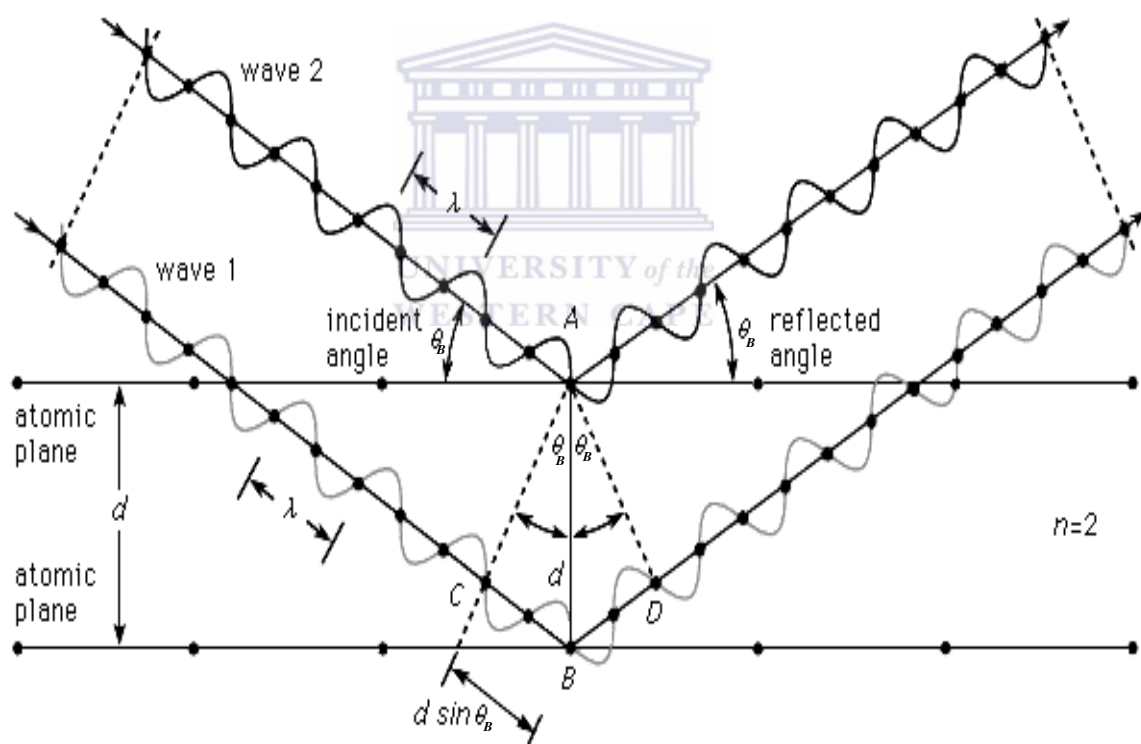$$2d\sin\theta_B = n\lambda \qquad\qquad (2.4)$$

Figure 2.19: *Visualization of diffraction from a perfect crystal plane according to Bragg's law [2.10]*

2.3.3.4   The x-ray diffractometer

An x-ray diffractometer, shown in figure 2.20, accurately measures the intensity of a diffracted beam by means of an electronic counter [2.10]. This instrument utilizes monochromatic x-rays, originating from S, and an x-ray detector that is positioned at G on the circumference of a circle with the sample at its center (C). X-rays diverge from the source S and are diffracted by the specimen in such a manner that it will converge to a focus point at the slit F (A & B are slits used for definition and collimation of the incident and diffracted beams).

The specimen, supported on a table H, can be rotated about an axis perpendicular to the drawing. The position T in figure 2.20 is the focal spot on the target of the x-ray tube. The supports E and H are mechanically coupled in such a way that a rotation of the counter through 2θ degrees is simultaneously accompanied by a rotation of the specimen through θ, thereby conserving focussing conditions.
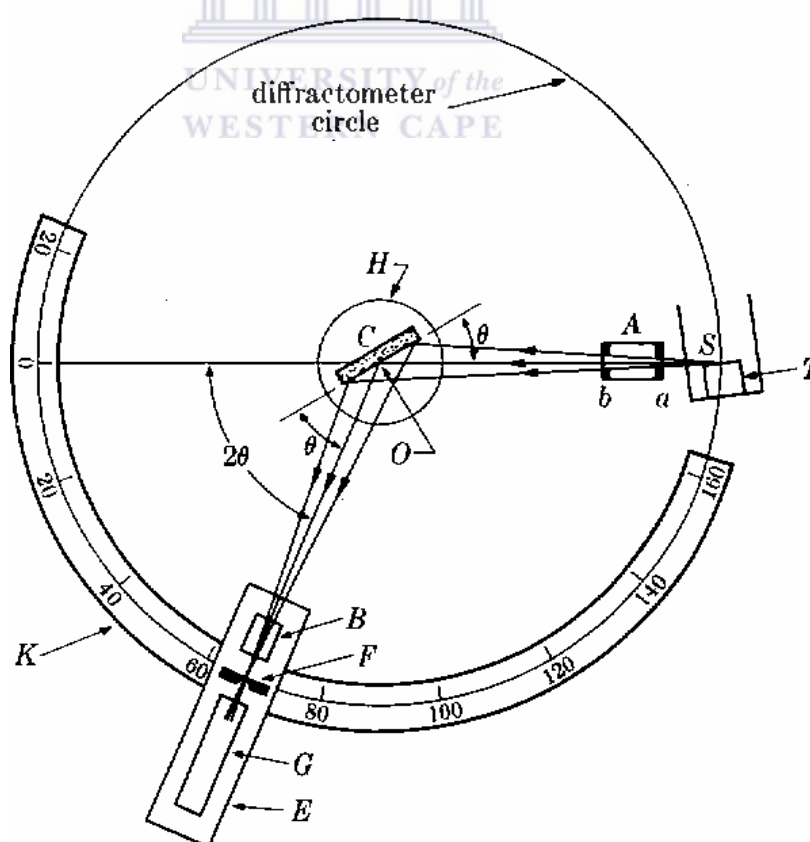

Figure 2.20: *Schematic of an x-ray diffractometer [2.10]*

2.3.3.5   The Laue equations

A unique geometrical description for diffraction is given by the Laue equations. The scattering vector, $\Delta \vec{k}$, is the change in wavevector on scattering and when added to the incident ($\vec{k}$) wavevector yields the scattered wavevector ($\vec{k}`$), as shown in figure 2.21 [2.3, 2.10]. This vector lies in reciprocal space, an abstract mathematical concept where distances are reciprocal to real space and Fourier analysis is used to describe x-ray diffraction based on the periodic arrangement of the electron clouds in the crystal [2.10]. Utilizing the orthogonal relationship between the scattering vector and the crystal lattice vectors as well as the condition that the resultant of the incident and diffracted waves must be a point in reciprocal space, one arrives at the Laue equations [2.3]:

$$\vec{a} \bullet \Delta \vec{k} = 2\pi h, \ \vec{b} \bullet \Delta \vec{k} = 2\pi k \ \text{ and } \ \vec{c} \bullet \Delta \vec{k} = 2\pi l \qquad (2.5)$$

where the integers *h*, *k* and *l* are the indices for the Bragg plane responsible for the diffraction. The simultaneous satisfaction of these equations provides the strict condition for diffraction to occur.
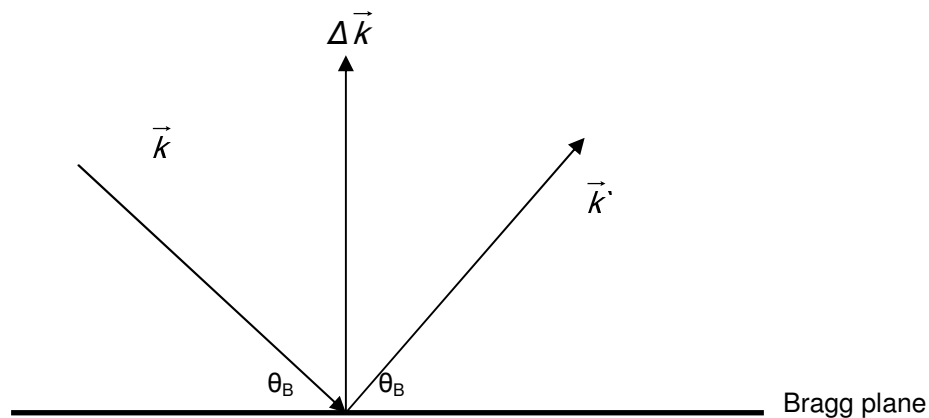

Figure 2.21: *Schematic showing the relationship between the scattering vector, incident and diffracted x-ray as well as the Bragg plane and diffraction angle during x-ray diffraction [2.3, 2.10]*

2.3.3.6   Structure and the atomic form factor of the basis

Bragg's law provides a simple geometrical explanation for the condition of diffraction. The intensity of the scattering from the basis of atoms requires a deeper analysis of diffraction. More specifically, the spatial distribution of electrons of each atom within each cell must be considered to predict and account for why only certain planes in certain crystal systems are allowed to diffract an x-ray. Consider a cell with a jth atom located in the Bravais lattice at a position relative to the origin given by equation (2.6) [2.3]:

$$\vec{r_j} = u_j \vec{a} + v_j \vec{b} + w_j \vec{c} \qquad (2.6)$$

Suppose that the amplitude of the scattered x-ray from a certain volume element is proportional to the local electron density. The scattered amplitude is therefore proportional to the geometrical structure factor F given by equation (2.7) [2.3]:

$$F \ (hkl) = \sum f_j \, exp\big[2\pi\big(u_i h + v_j k + w_j l\big)\big] \qquad (2.7)$$

where f_j is the atomic form factor, $(h\ k\ l)$ are the indices for the Bragg plane and j runs over the atoms of the basis. Physically, the atomic form factor is the ratio of the radiation amplitude scattered by the actual electron distribution in an atom to that scattered by a localized electron. The intensity (I) of the beam diffracted by all the atoms in the unit cell is directly proportional to the square of the amplitude of F, i.e. $I \ \alpha \ |F|^2$. To attain monochromated x-rays for each ($h\ k\ l$) reflection, a special monochromater is used at the expense of intensity, thereby allowing one to determine the relative intensity of any ($h\ k\ l$) reflection by knowing the lattice type representing the crystal structure of the material under investigation [2.3].

2.3.3.7   XRD study of a carburized filament

Tungsten has a bcc crystal lattice and therefore have atoms at the positions $u_1 = v_1 = w_1 = 0$ and $x_2 = y_2 = z_2 = \frac{1}{2}$. According to (2.7), $F (hkl) = f\{1 + exp[\ i\pi(h + k + l)]\}$, which means that $F = 0$ whenever the exponential value is -1, i.e. whenever the argument is $h + k + l = odd\ integer$. Else, $F = 2f$ if the indices of the planes gives $h + k + l = even\ integer$. This means that planes in the crystal structure of tungsten that will diffract intensely are those whose indices add to an even integer, e.g. (*110*), (*200*) and (*211*). In fact, these three planes, occurring at $2\theta = 40.3°, 58.3°$ and $72.2°$ respectively, are the most intense features of a XRD spectrum for a pure W-filament [2.11, 2.12]. As the carburization process proceeds, intensities of the W_xC_y phases increase whilst that of tungsten decreases. This indicates that the crystal structure of the W-filament is transforming into carbides, i.e. carburizing.

2.4 References

[2.1] M. S. Amer, M. M. El-Ashry and J. F. Maguire, *Journal of physical chemistry*, **121**, p 252 (2004)

[2.2] G. Dent and E. Smith, "Modern Raman Spectroscopy: A Practical Approach", *John Wiley & Sons Ltd.*, England (2005).

[2.3] C. Kittel, "Introduction to Solid State Physics", 8th edition, *John Wiley & Sons*, USA (2005)

[2.4] M. S. Dresselhaus, G. Dresselhaus, A Jorio, A. G. Souza Filho, and R. Saito, *Carbon*, **40**, 2043 (2002)

[2.5] M. Hulman, Carbon nanotubes and Raman spectroscopy, Institut für Materialphysik Universität Wien [Online]. Available www.fkf.**m**pg.de/conf/heraeus/**hulman**.pdf, accessed online on 12-11-2007

[2.6] M. S. Dresselhaus, G. Dresselhaus, R. Saito and A Jorio, *Physics Report*, **409**, 47 (2005)

[2.7] A. Jorio, R. Saito, J. H. Hafner, C. M. Lieber, M. Hunter, T. McClure, G. Dreselhaus and M. S. Dresselhaus, *Phys. Rev. Lett.*, **86**, p 1118 (2001)

[2.8] K. Howard, A. Johnson, K. McMichael and M. T. Postek, "Scanning Electron Microscopy - A Students Handbook", *Ladd Research Industries, Inc.*, Burlington (1980)

[2.9] E. Salernitano, T. D. Makris, R. Giorgi, N. Lisi, L. Pilloni, F. Sarto and M. Alvisi, *Diamond and Related Materials*, **13**, 305 (2004)

[2.10] B. D. Cullity, "Elements of X-ray Diffraction", 2nd edition, *Addison-Wesley Publishing Company Inc.*, USA (1978)

[2.11] S. Schwarz, E. Zeiler, S. M. Rosiwal and R. F. Singer, *Materials Science and Engineering A*, **335**, 236 (2002)

[2.12] A. Kromka, J. Janík, A. Šatka, J. Pavlov and I. Červeň, *Acta Physica Slovaca*, **51**, 359 (2001)

CHAPTER THREE

FILAMENT CARBURIZATION

3.1   Introduction

The hot-wire chemical vapour deposition (HWCVD) technique has been studied intensively due to its promise to be a low-cost, repeatable route for mass-production of carbon nanotubes (CNTs) [3.1, 3.2]. During the synthesis, the filament serves as a catalyst for the dissociation of the gas phase species that contribute to the growth of CNTs. However, for the duration of the deposition it was assumed that the filament-surface and temperature remained constant. This is not the case since it was showed that at elevated temperatures, tungsten (W) filaments carburize in a methane (CH_4) / hydrogen (H_2) environment and are consequently transformed into their carbides or covered by a solid carbon layer [3.3 - 3.9]. Carburization affects the dissociation rate of the precursor gases and ultimately the structural properties of the CNTs.

In order to understand these processes it is necessary to monitor the changes in the structural properties of the filament as a function of exposure time and temperature. This chapter investigates the structural changes of W-filaments at different temperatures and exposure times whilst keeping the mixture of CH_4 / H_2 precursor gases and deposition pressure constant.

3.2   Experimental

3.2.1   The Filaments

W-filaments were used in this study as catalysts for the dissociation process of the precursor gases and the supply of reactive species for the growth of CNTs on nickel catalysts. Each experiment started with a commercially pure W-filament 350 mm long and a diameter of 0.5 mm. The filaments were coiled and resistively heated to the desired temperatures in an environment consisting of 10 sccm CH_4 and 100 sccm H_2 at a deposition pressure of 150 Torr. Exposure times amounted to 5, 15, 30, and 60 minutes at each filament-temperature (T_{fil}) of 1600 - 2000 °C (in increments of 200 °C).

During the deposition the resistance of the filament as a function of time was calculated from the applied dc-electrical current and the potential difference over the filament. The temperature of the filament was measured using a Raytek® two-colour pyrometer that was placed approximately 1.5 m away from the filament. The temperature measurement was therefore independent of emissivity changes. The temperature of the filament was much lower at the electrical contacts. After deposition the filaments were allowed to cool down to room temperature, after which they were removed and then stored away for analysis. The filaments were highly brittle after the treatment and therefore great care was taken when removing the filaments in order to prevent any mechanical disturbance to its surface.

3.2.2   Characterization

The surface and cross-sections of the W-filaments were examined using a Hitachi® X-650 scanning electron microscope (SEM). The microscope was operated at accelerating voltages of 12 kV and 25 kV and had a resolution of approximately 15 nm. Micrographs were captured digitally using the AnalySIS® (Soft Imaging System) package and stored to a hard disk.

Qualitative elemental composition of the filament was performed at 12 kV and 25 kV using the EDAX® set-up for energy dispersive spectroscopy (EDS) with a detector resolution of 140 eV. Phase identification, performed on a coil from the central part of the filament, was measured using the Phillips® X-ray Diffractometer. The system was operated in a θ - 2θ geometry at 45 kV and 40 mA using Cu K_α radiation as an x-ray source. X-ray diffraction (XRD) spectra were collected from θ = 5 to 40°. The x-ray collection time per step was 20 seconds at a step size of 0.02°.

3.3   Results and discussion

3.3.1 The commercially pure tungsten-filament

The XRD spectrum of the pure W-filament, before it was operated at the experimental conditions, is shown in figure 3.1. The spectrum shows three characteristic peaks associated with a tungsten bcc crystal structure.
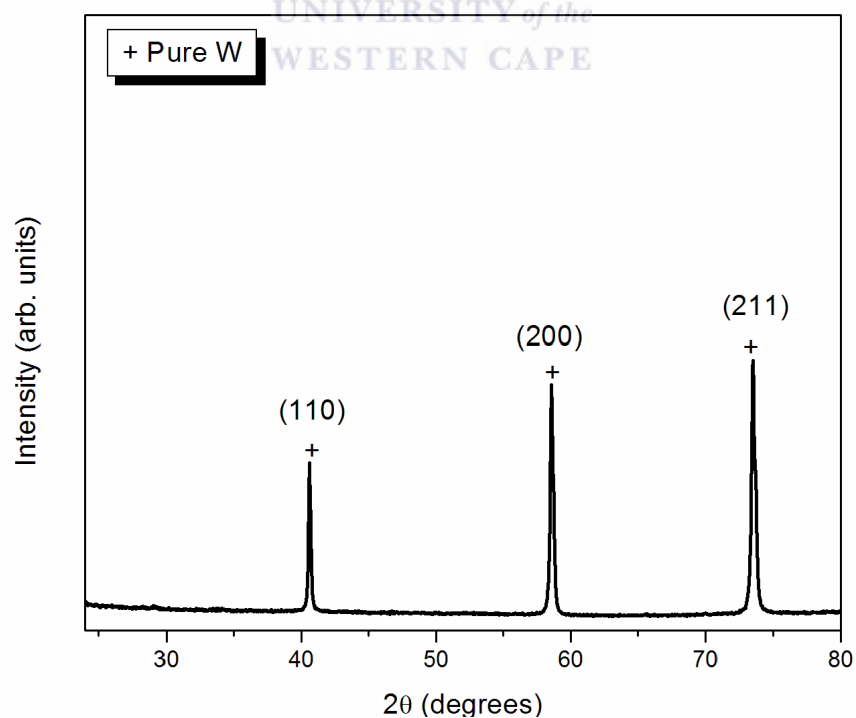

Figure 3.1:   *XRD spectrum of the filament before carburization*

SEM micrographs of the filament-surface before the treatment are shown in figure 3.2. The surface has grooves indicating that it was produced by an extrusion method. Furthermore, the surface is covered with dark spots (see figure 3.2b), which correspond to carbon impurities according to EDS analysis. This affirms the need to heat the filament prior to deposition in order to remove any impurities from its surface. Figure 3.3 presents a SEM micrograph showing the cross-section of the filament before carburization. The diameter of the filament is approximately 500 μm.
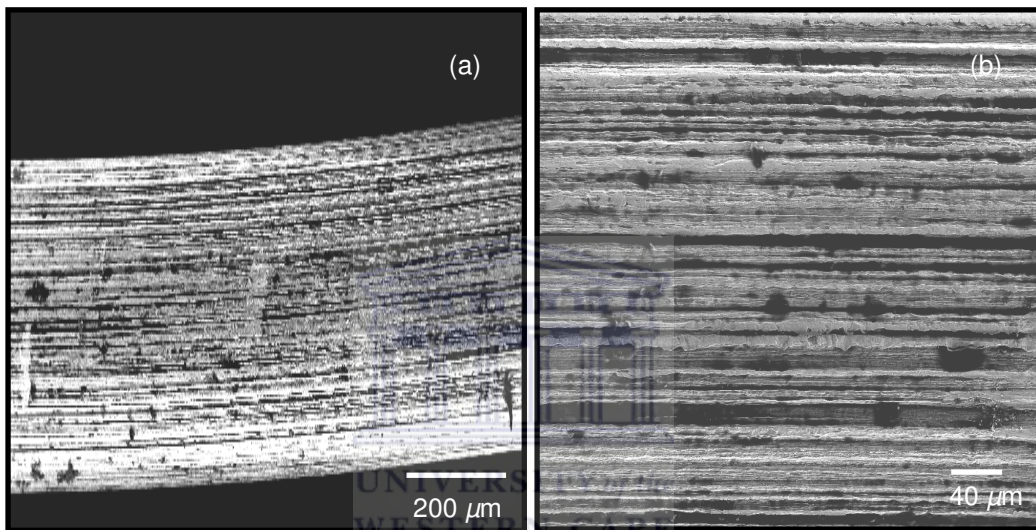

Figure 3.2: *(a) SEM micrograph of the filament surface before carburization and (b) a close up of the surface*
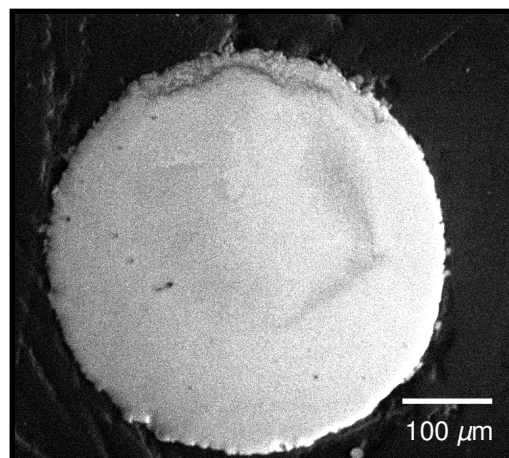

Figure 3.3: *SEM micrograph showing the cross-section of the filament before carburization*

3.3.2 Phase transitions

Figure 3.4 shows the XRD spectra of the W-filament carburized for different times at 1400 °C. After the filament was carburized for 5 minutes, the XRD analysis reveals the presence of W, ditungsten carbide (W_2C) and monotungsten carbide (WC) at the filament-surface, implying that carburization occurred. All of the XRD peaks were identified using the JCPDS cards listed in the Joint Committee for Powder Diffraction Studies (JCPDS) [3.10]. An increase in the XRD intensities of the WC phase at and above 15 minutes is noticeable. This implies that the WC phase is enhanced with time. Furthermore, the full-width at half maxima (FWHM) of the WC peaks decrease with exposure time, indicating that the sizes of the WC crystallites become larger with time.
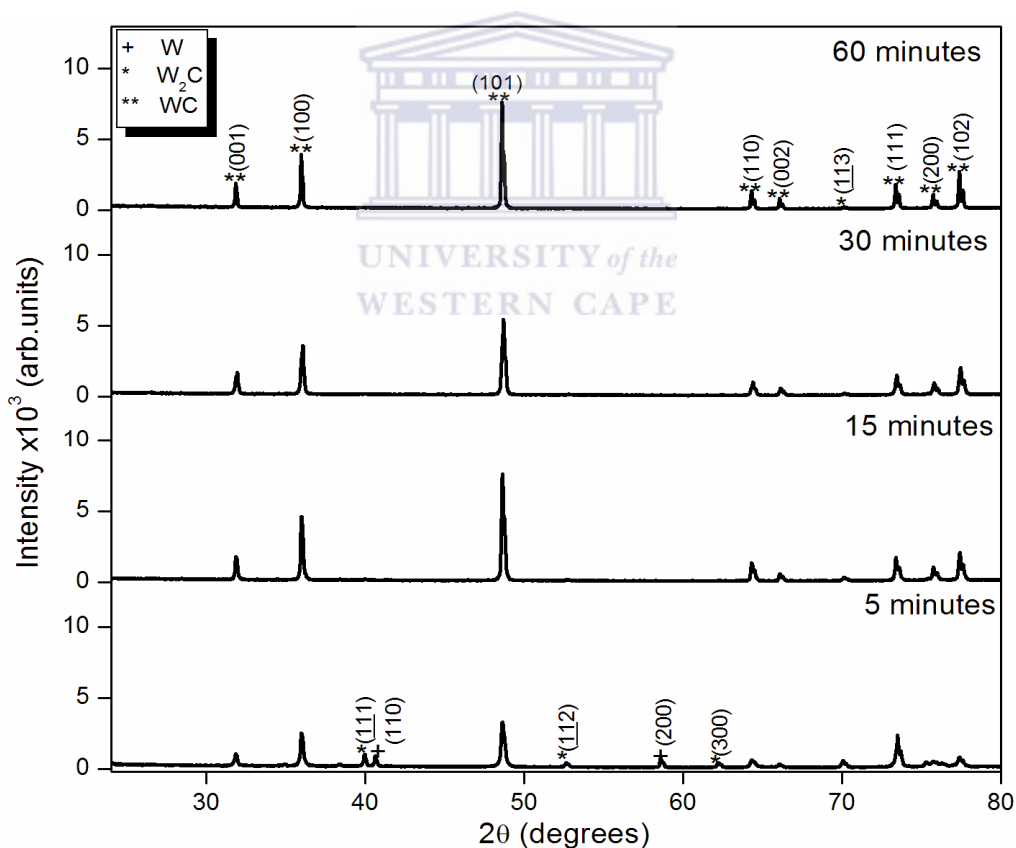

Figure 3.4:   *XRD spectra showing how the filament-surface changes as a function of time at a filament-temperature of 1400 °C*

The behaviour in the XRD spectra presented in figure 3.4 is explained as follows. Davidson *et al.* [3.8] studied the reaction kinetics of W-filaments being carburized in a CH_4 containing ambient. They found that the slowest step during the growth of the W_2C phase is the dissociation of CH_4 on the surface of the filament. Furthermore, they found that the slowest step during the formation of the WC phase is the supply of carbon (C) via diffusion. Zeiler et al. [3.6] confirmed the findings of Davidson *et al.* [3.8] and found through XRD analysis that the W_2C phase formed first and then the WC phase formed at the expense of the W_2C phase. Based on these findings, it is argued that the carburization process is dependent on the rates of CH_4 / H_2 dissociation, carbon (C) diffusion and C-accumulation on the filament-surface. Initially, the CH_4 molecule is catalytically reduced to C at a filament-temperature of 1400 °C. The produced C then diffuses into the W-filament resulting in the formation of the W_2C phase. When the W_2C layer becomes thick enough and the diffusion rate of C is reduced, the C-accumulation rate increases. Furthermore, the high CH_4 concentration and deposition pressure also enhances the C-accumulation rate. As a result, the stability region of the WC phase increases [3.8, 3.12], resulting in the formation of this phase within the first 5 minutes, which is much faster than previously reported [3.3 - 3.9]. Furthermore, the C-accumulation rate at the filament-surface increases as a function of time. This enhances the formation of larger WC-crystallites and the dominance of this phase at the surface with time, as confirmed by the reduction in the FWHM of the WC peaks.

Increasing the filament-temperature to 1600 °C, results in the phase evolution with respect to time as shown in figure 3.5. Similar to 1400 °C, the W_2C and WC phases are present at the filament-surface within the first 5 minutes. However, no W peaks were detected at 5 minutes and the FWHM of the WC peaks increased until 15 minutes, subsequently they remained constant. Similarly, the intensities of the WC peaks relative to the other peaks increased until 15 minutes and then remained relatively constant afterwards. This implies that the formation of the WC phase is hindered after 15 minutes at 1600 °C.

Interestingly, at the same time a graphitic phase is detected as seen by the broadened peak centred around 26 °. The crystallites of the graphitic phase are relatively small as can be seen by the broadened peak. Surprisingly, the intensity of the graphite peak decreases afterwards.
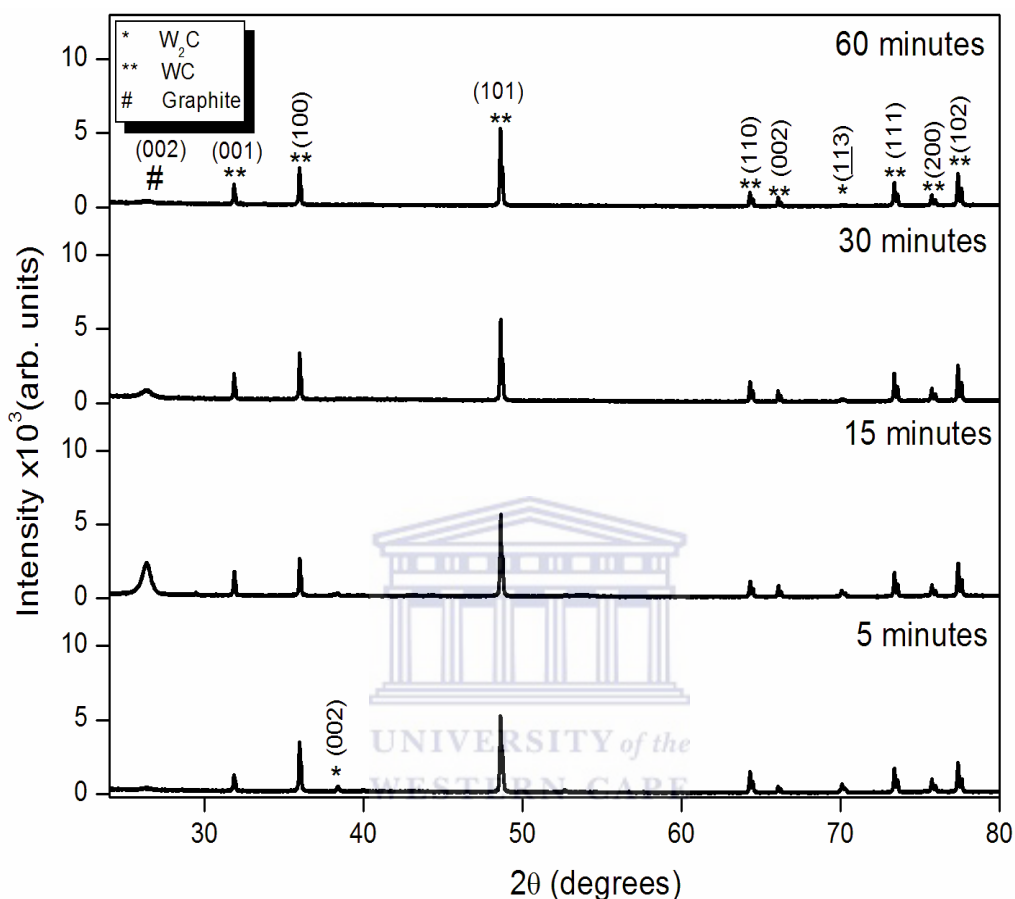

Figure 3.5: *XRD spectra of the filament-surface as a function of exposure time at 1600 °C*

When the filament was carburized at 1600 °C, an increase in the CH_4 dissociation and the C-accumulation rates occur. This is clearly seen in the absence of the W peaks and the higher intensities of the WC peaks compared to 1400 °C at 5 minutes. In contrast to 1400 °C, the CH_4 dissociation rate becomes much faster than the diffusion rate during the first 15 minutes, resulting in an enhanced C-accumulation rate at the filament-surface. Instead of diffusing into the filament, the C atoms combine to form a graphitic phase at the filament-surface.

The formation of the graphitic phase ultimately suppresses the formation of the WC phase as can be seen in the constant intensities and widths of the WC peaks after 15 minutes. In addition, the intensities of the WC peaks are lower than at 1400 °C. At this point it is not clear why the XRD intensity of the graphitic phase decrease after 15 minutes. Figure 3.6 shows the XRD spectra of the W-filament carburized for different times at 1800 °C, where a definite transition in the reaction rates at the filament-surface can be seen. The surface of the W-filament is transformed into W_2C and WC phases during the first 5 minutes. No W peaks were detected during the first 5 minutes. In contrast to lower filament-temperatures, at 1800 °C the detected W_2C planes becomes more pronounced. Furthermore, an intense and broadened graphitic peak is observed at 30 minutes. The intensity of the graphitic peak drops at 60 minutes of carburization. Interestingly, the intensities of the WC peaks are lower than at lower filament-temperatures, especially when the graphitic peak starts appearing.
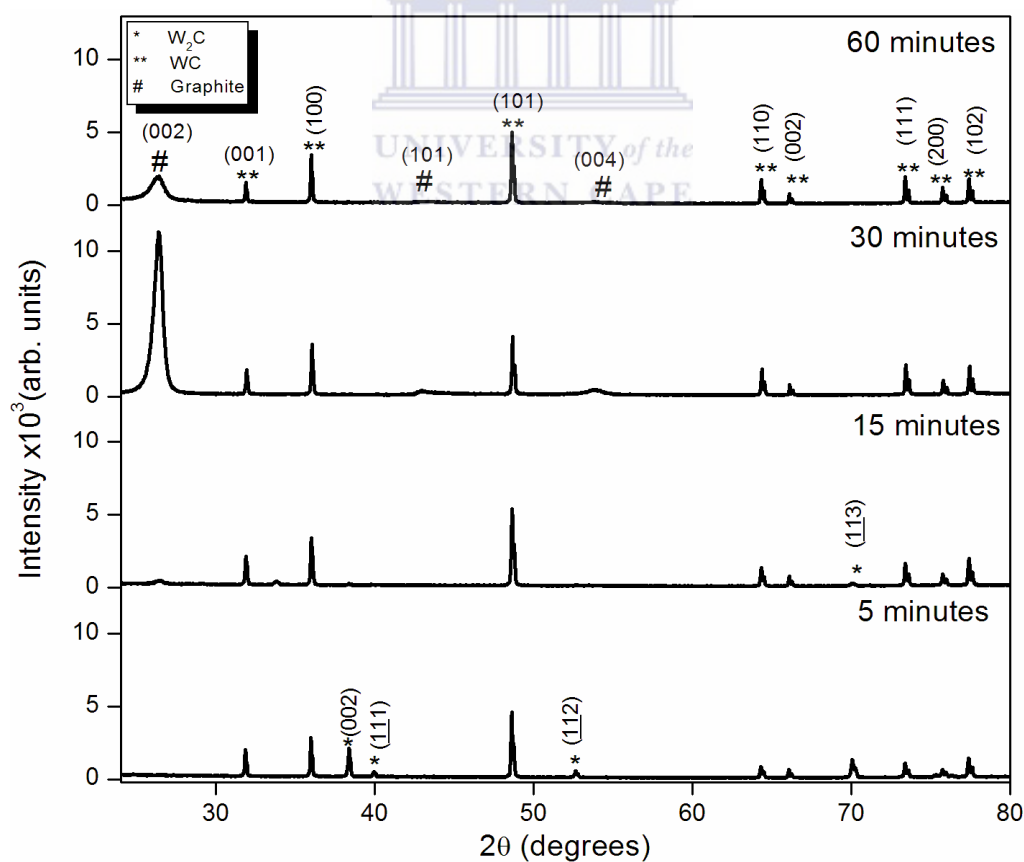

Figure 3.6: *XRD spectra showing the phase transition of the filament-surface as a function of time at 1800 °C*

As argued earlier, the growth of the W_2C phase occurs at a slow rate of CH_4 dissociation, i.e. a slow C supply rate. While the filament was carburized at 1800 °C, the CH_4 dissociation and C-diffusion rates are higher than at lower filament-temperatures. In addition, there is also another important reaction that occurs at elevated filament-temperatures, which also plays an important role during filament carburization. This reaction corresponds to the dissociation of the H_2 molecule to atomic hydrogen. By studying the emissivity of W-filaments at temperatures in excess of 2000 °C, Sommer *et al.* [3.9] found that atomic hydrogen etches carbon and by forming gaseous hydrocarbons. Furthermore, Mastubara *et al.* [3.4] stated that the generation of atomic hydrogen increases exponentially with the filament-temperature. This etching process effectively reduces the C-accumulation rate and therefore enhances the stability region, i.e. low carbon concentration, of the W_2C phase at 5 minutes for a W-filament carburized at 1800 °C.

However, with an increase in the exposure time and temperature, the C-diffusion rate decreases because of thicker W-carbide layers. Consequently, the CH_4 dissociation rate becomes too overwhelming compared to the C-diffusion rate. This results in a higher increase in the rate of C-accumulation on the filament-surface than at lower filament-temperatures and exposure times. Consequently, this leads to the dominating graphitic peak at 30 minutes. Moreover, the graphite layer may be so thick that it will start to diffract more x-rays during XRD, which further accounts for the drastic decrease in the WC peaks at 30 minutes.

Figure 3.7 presents the XRD spectra of the filament-surface carburized for different times at 2000 °C. Contrary to lower filament-temperatures, only the W_2C phase is present on the filament-surface at 5 minutes. However, at 15 minutes only the WC phase is detected by XRD. The intensities of the WC peaks increased whilst their widths decreased with exposure time until 30 minutes. At 60 minutes a graphitic peak is present and the relative intensities of the WC peaks decreased.
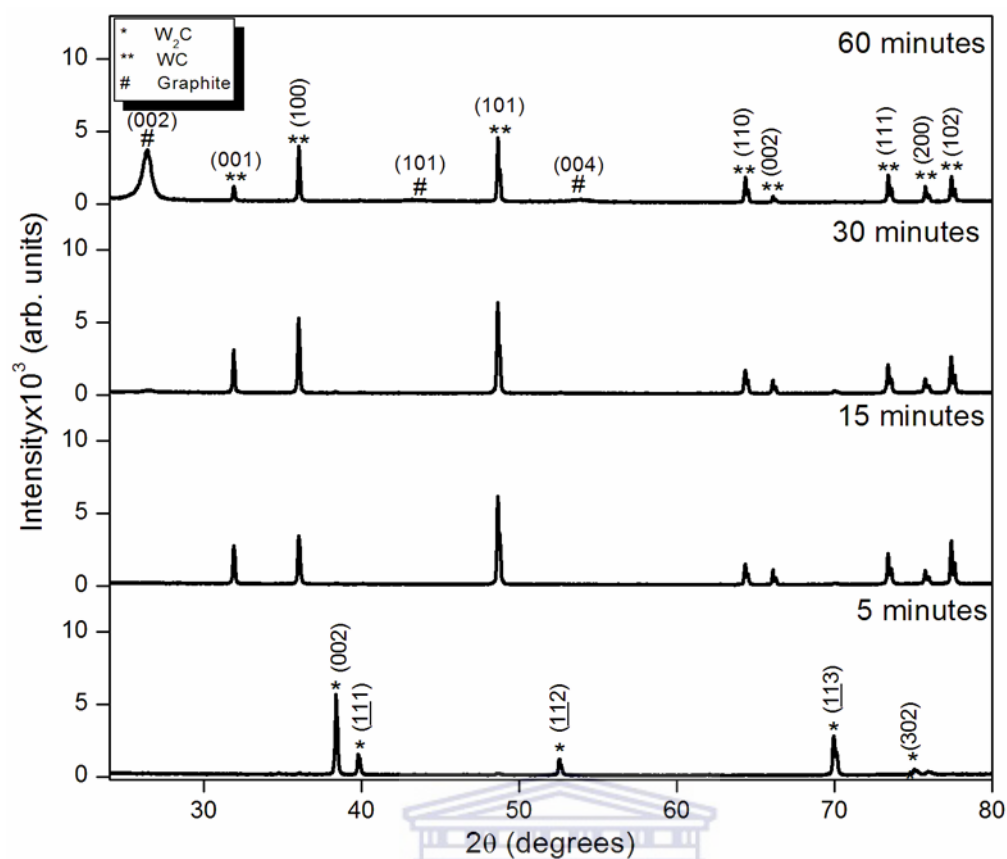
Figure 3.7: *XRD spectra showing the phase transition in the filament-surface with respect to exposure time at $T_{fil} = 2000$ °C*

The XRD spectra showed in figure 3.7 confirm the earlier argument regarding the increase in the rate of atomic hydrogen generation with the increase of the filament-temperature. This is suggested by the presence of only the W_2C peaks at 5 minutes and the delay in the appearance of the graphitic peak.

The emphasis of this section will now be shifted to determining the most stable region of the surface of the filament, based on the XRD analysis on CNT deposited by HWCVD. During the deposition of CNTs using the HWCVD technique, it is agreed that there must be a region of compromise between the various kinetic factors during the deposition of CNTs on transition metal catalysts. These factors occur at nano-sized transition metal particles and include the dissociation of the hydrocarbon gas, diffusion of C into the catalyst until the catalysts is supersaturated and the eventual precipitation of C in a tubular form [3.13].

Furthermore, Cojocaru *et al.* [3.14] found that by varying the H_2 dilution in ammonia (NH_3), the atomic hydrogen acts as a good amorphous carbon etching agent for a purer CNT deposition. Zeiler *et al.* [3.6] found that the W_2C phase is a transition phase between a W-filament and a fully carburized, WC-filament. They also found, by studying the mass spectroscopy of the exhaust gas, that the carbon containing species decrease when the W_2C forms and increased drastically when the WC phase start to form. Based on these findings, it is thus apparent that a WC-filament surface free of a graphitic phase is important for a stable CNT deposition using HWCVD.

It is therefore suggested that the highest XRD intensities of W_2C and WC, i.e. at $2\theta = 38.39°$ (0 0 2) and $48.65°$ (1 0 1), respectively, as well as the graphitic-like carbon peak will be monitored as a function of filament-temperature. Since CNTs grow rapidly within the first few seconds of deposition [3.15], carburization times of 5 and 15 minutes will be considered. Figure 3.8 shows a plot of the diffracted intensity of W_2C versus T_{fil} at 5 minutes of exposure time. The plot clearly show that during the first 5 minutes the W_2C intensity increased with filament-temperature, which means an increase in the concentration of the W_2C phase at the filament surface.

The trend shown in figure 3.8 suggests that the instability of the carburized filament-surface increases with the filament-temperature. During the growth of the W_2C phase the diffusion rate of C is higher than the CH_4 dissociation rate. This means that the rate of C incorporation into the filament is enhanced and the available carbon for CNT deposition is reduced as a function of temperature during the first 5 minutes.
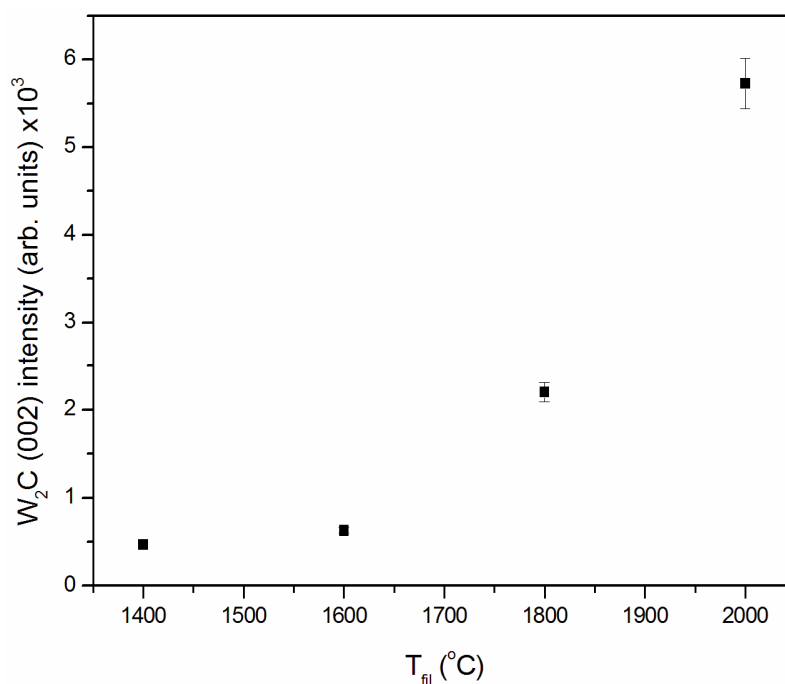
Figure 3.8: *Plot of the XRD intensity of the W₂C (002) plane as a function of T_fil at an exposure time of 5 minutes*

Figure 3.9 shows a plot of the WC intensity versus T_{fil} at 5 minutes and 15 minutes carburization time. During the first 5 minutes, the WC phase intensity increases until $T_{fil} = 1600$ °C, subsequently decreasing at and above 1800 °C. This behaviour agrees well with the increase in the W₂C concentration of the surface, shown in figure 3.8. It is argued that during the first 5 minutes from 1400 °C to 1600 °C, the CH_4 dissociation rate increased faster relative to the carbon diffusion rate. This resulted in an increasing XRD intensity of the WC phase from 1400 °C to 1600 °C. At higher filament-temperatures, the carbon etching rate is higher than the carbon generation and diffusion rates. Since the growth of the WC phase is diffusion controlled [3.8], this leads to a decrease in the XRD intensities of the WC phase. However, at 15 minutes of carburization, the C-diffusion rate displays the slowest step because of the lower C-diffusion coefficients in carbides [3.7]. When the filament was carburized at a temperature of 1400 °C, the C-diffusion rate is lower than at higher filament-temperatures, resulting in a higher WC intensity. At 1600 °C and 1800 °C the C-accumulation rate is higher than the C-diffusion rate, resulting in the formation of a graphite-like carbon layer on the filament-surface.

The formation of the graphite-like carbon phase results in a lower supply of C for the WC phase formation as well as an enhanced diffraction of x-rays by the graphite layer as it becomes thicker. These processes lead to the lower WC diffraction intensity at 1600 °C and 1800 °C. As the filament-temperature increases further to 2000 °C, the diffusion rate of C decreases after 5 minutes, consequently enhancing the C-concentration at the filament-surface and thereby increasing the WC concentration in the filament matrix.
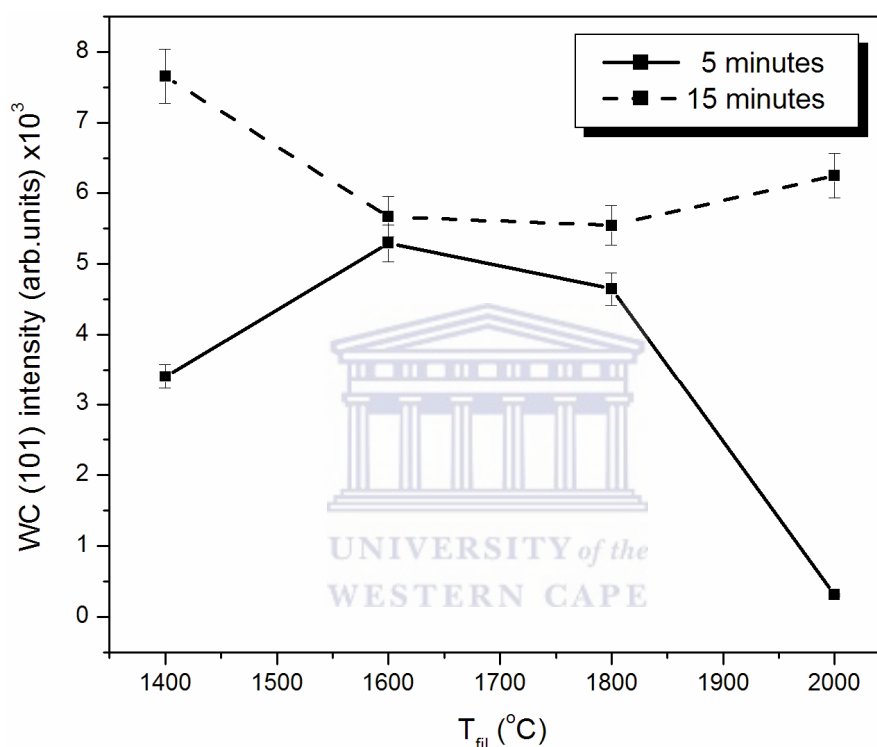

Figure 3.9: *Plot showing the XRD intensity of the WC (101) plane as a function of the filament-temperature for 5 and 15 minutes. The lines are drawn to guide the eye.*

Based on the XRD analysis, the optimized filament-temperature where the filament surface is more stable after 5 minutes of carburization is gauged at 1400 °C. At this temperature the W-filament carburized to the WC phase at 15 minutes and remains free of a graphite layer up to 60 minutes of carburization, thereby ensuring a more stable supply of carbon for CNT deposition. This filament-temperature is also the lowest reported for filament carburization in previous studies [3.4 – 3.9].

Previous investigations suggest that XRD is the characterization method of choice to study the carburization process of W-filaments [3.4 – 3.9]. However, the XRD studies need to be corroborated by other techniques that probe into the morphology of the filament-surface and its internal structure, which will be the topic of the next section.

3.3.3 Morphology

Figure 3.10 presents the SEM micrographs of the filament-surface carburized at 1400 °C for different times. The grooves observed on the pure W-filament are still present in all exposure times. However, it is noticeable that the surface roughness increases with exposure time. Subsequently, hemispherical deposits form and grow along the grooves at an exposure of 60 minutes, as shown in figure 3.11. Similar deposits on a carburized W-filament surface were observed by Moustakas [3.5]. According to Moustakas [3.5] and Davidson *et al.* [3.8], the incorporation of C into the filament results in the increase of the crystallite size for the WC phase. Subsequently, this leads to a roughened appearance of the surface. This serves as a clear indication of the filament carburization and therefore confirms the XRD analysis presented in figure 3.4. Furthermore, Moustakas [3.5] found that the deposits are carbonaceous and that their formation is related to the adhesion and release of C from the filament-surface. Zeiler *et al.* [3.6] argued that the diffusion lengths of C are shortened at defect regions within the surface of the filament. It is therefore argued that during carburization, C accumulates at defect-rich regions, for instance the grooves of the filament. As was shown by the XRD analysis, there seems to be a critical C-accumulation level that results in the formation of graphite. However, at the same time C is also released at some places from a WC surface according to results by Zeiler *et al.* [3.6]. Furthermore, the high surface tension associated with the heated WC surface also prevents the graphite layer from covering the surface. These two processes contribute to the hemispherical form of the deposits.
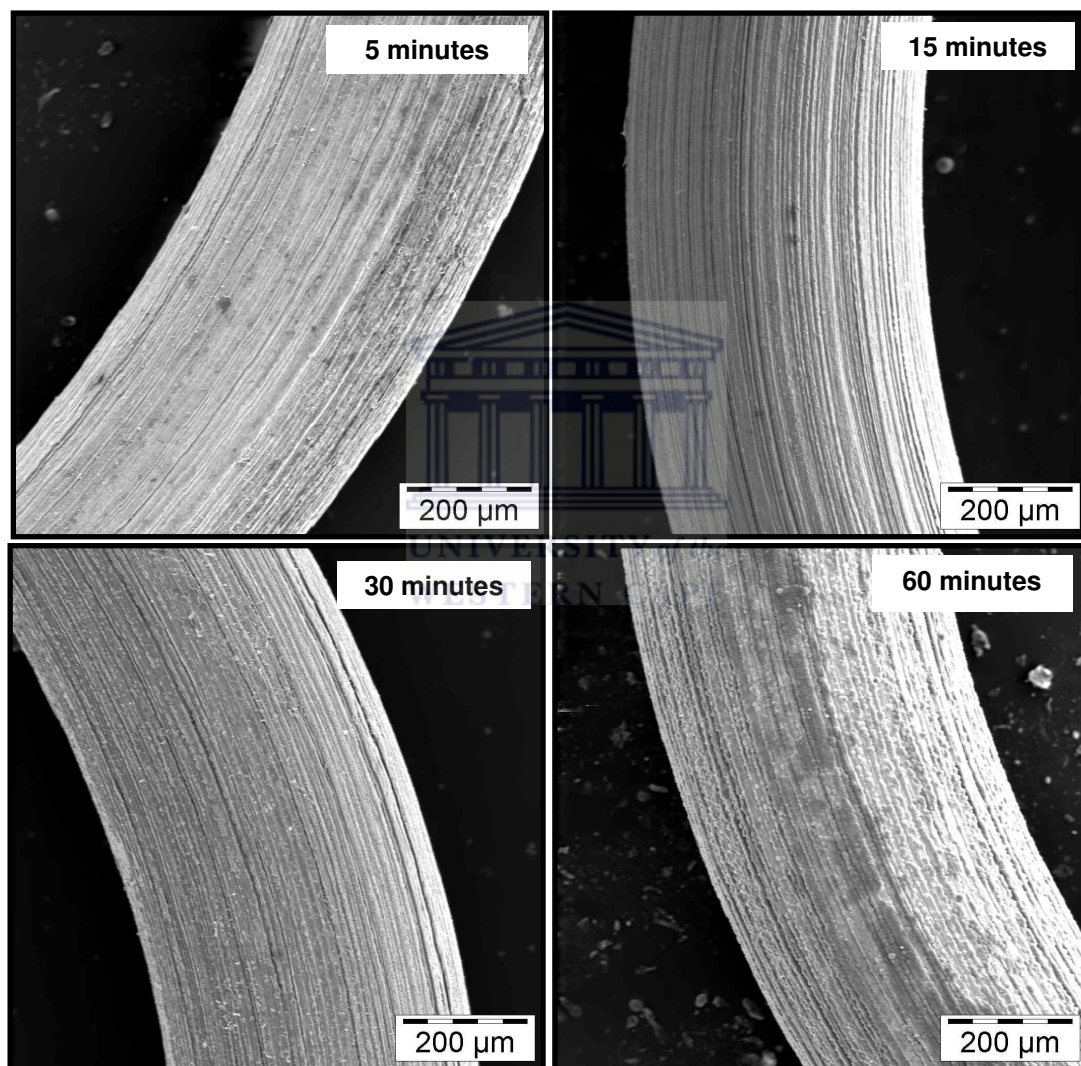
Figure 3.10: *SEM micrographs showing the W-filament heated at 1400 °C for different times at the operating conditions*
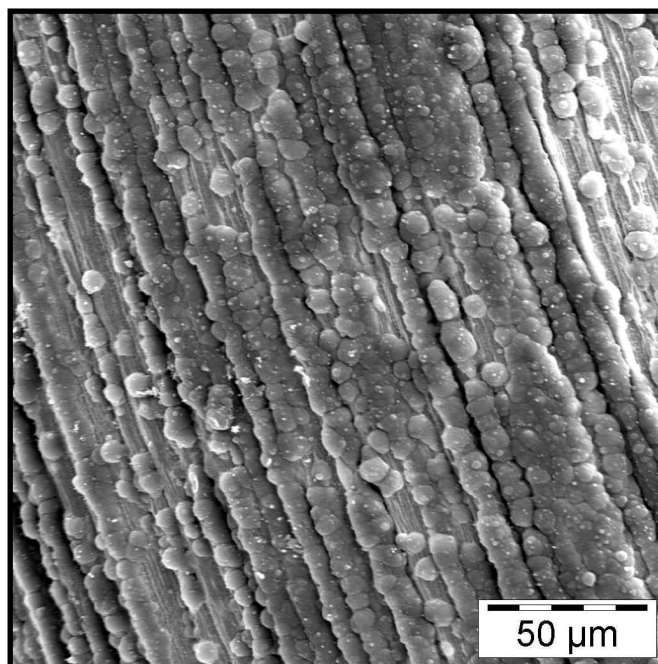
Figure 3.11: *SEM micrograph at a higher magnification of the filament-surface heated at 1400 °C for 60 minutes showing the presence of hemispherical deposits along the filament-grooves*

As mentioned in *Section 3.3.2*, a coil from the central, hotter section of the filament was placed next to the corresponding cross-section. The ensemble was then sputtered with gold prior to the SEM analysis, since the resin was not conductive and would therefore minimize the charging of the sample during the SEM measurements. The EDS analysis performed in this study therefore shows the presence of a gold peak centred around 2.25 keV.

However, it is well known that metals are good x-ray absorbers. This will severely inhibit the characteristic x-rays produced during the EDS analysis to escape from the surface and be detected, especially the low energy C K_α x-ray centred on 0.25 keV. Consequently, the EDS analysis was not conclusive especially in the presence of both W and C on the filament. Therefore, the EDS analysis will only be presented at cases when there is only C present, which is expected based on the XRD analysis that showed the presence of graphitic carbon on the surface of the filament at and above 1600 °C.

Figure 3.12 shows SEM micrographs of the filament cross-section heated at 1400 °C as function of time. At 5 minutes the internal structure of the filament resembles that of a pure W-filament and the diameter is unaffected as it amounts to ~ 500 μm. This contradicts the XRD analysis, which illustrated the phase formation of W_2C and WC at this time. However, the carbide layer at an exposure times of 5 and 15 minutes may not be thick enough to be noticeable at this magnification. In contradiction with previous studies [3.4 – 3.9], at 1400 °C there are no cracks present resulting from the volume expansion of the filament as a function of time during carburization. The carbide layers at 1400 °C are not thick enough to induce the formation of cracks within the filament.
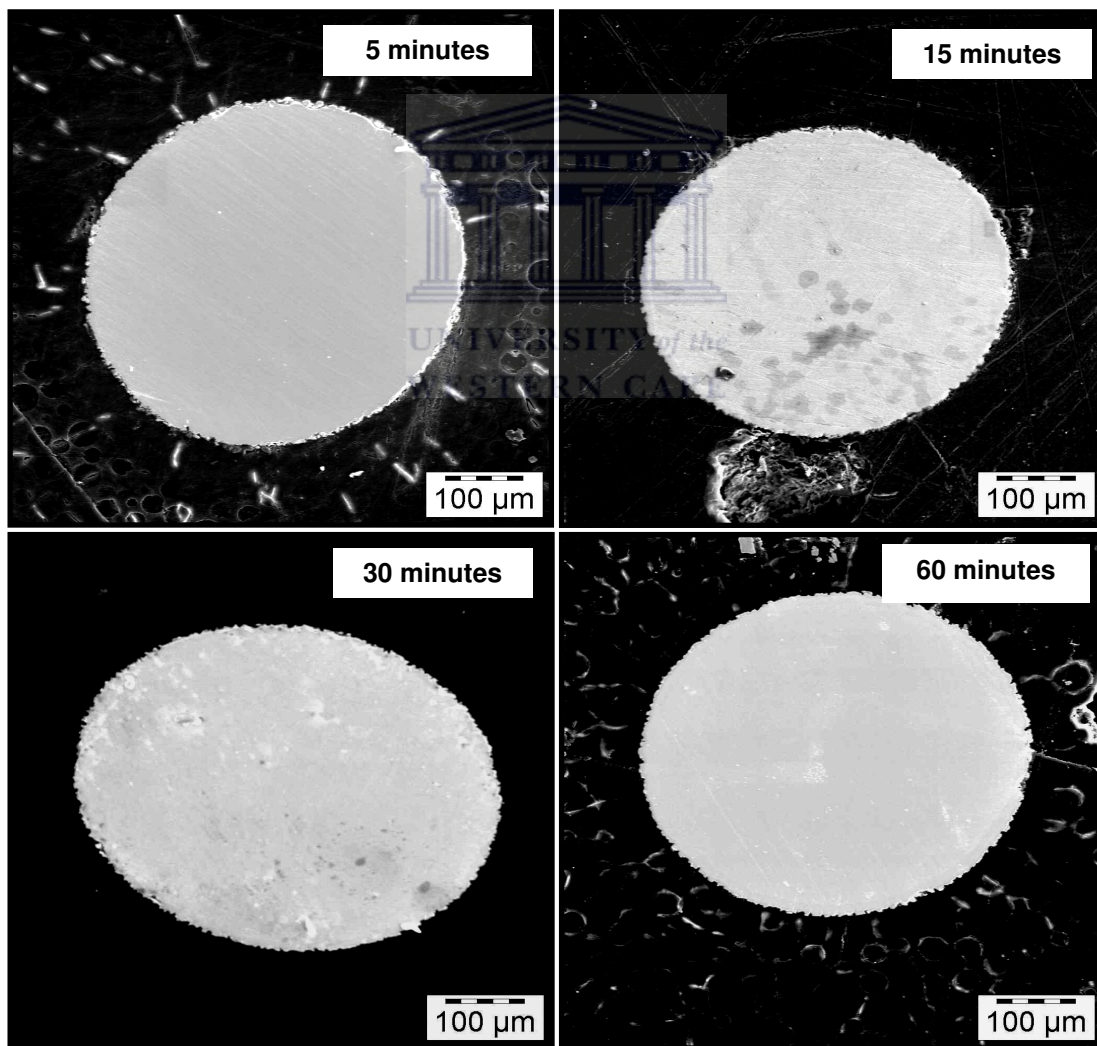

Figure 3.12: *SEM micrographs showing the internal structure of the filament after it was heated at 1400 °C for various durations*

SEM micrographs at a higher magnification of the cross-section at 30 and 60 minutes as presented in figure 3.13, reveal the presence of regions with different contrasts corresponding to the occurrence of W-carbides. The W_2C + WC layer is approximately 15 μm thick at 30 minutes. The carbide layer at 60 minutes has a total thickness of approximately 15 μm.
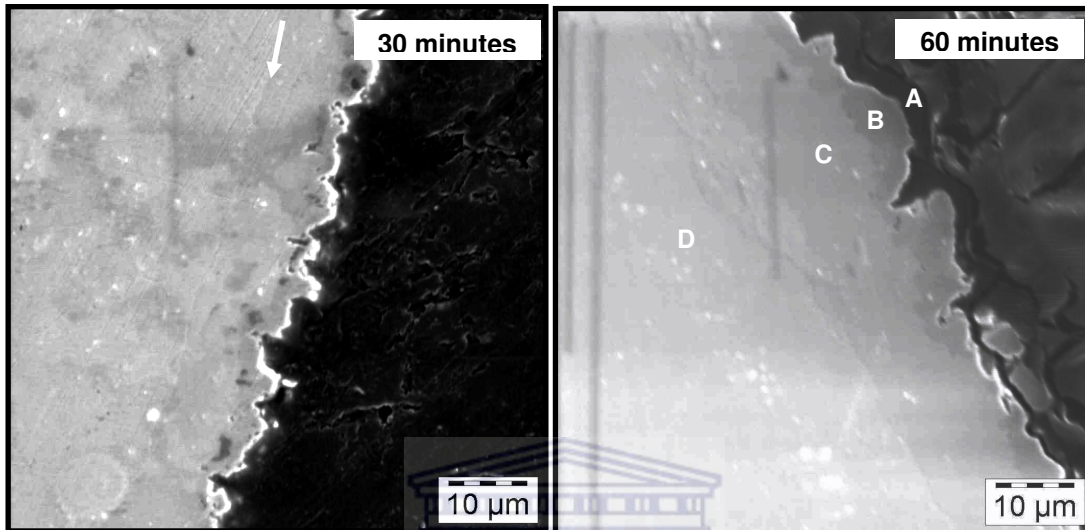

Figure 3.13: *SEM micrographs of the cross-sections' edges at 30 and 60 minutes showing the presence of carbides*

As proposed in the previous section, the W-filament carburized first to W_2C and then to WC. At 15 minutes and 30 minutes the two phases are not resolved. This indicates that the outer layer at 15 minutes and 30 minutes may be designated as a W_2C + WC phase. Furthermore, based on the XRD analysis, the WC content of the layer is more enhanced at 30 minutes than at 15 minutes. It was argued that the C-accumulation rate at the surface of the filament increases with time. This can be clearly seen in the cross-section at an exposure time of 60 minutes. There is a definite increase in the brightness of the edge radially inward and it is explained as follows. Low atomic number elements such as C appear "darker" in SEM pictures. The deposits seen at the outer edge (region A) corresponding to 60 minutes have a darker appearance, indicating a high concentration of C, which is in accordance with results by Moustakas [3.5].

Furthermore, the region B is a WC phase because of its stability at higher C-concentrations, region C corresponds to a W_2C phase and region D is a W inner core.

Figure 3.14 displays SEM pictures of a pure W-filament after being carburized for different durations at 1600 °C. The SEM micrographs show that the carbonaceous deposits occur within the first 5 minutes, much earlier than at 1400 °C. At 15 minutes the deposits increase in size and seem to grow preferentially along the grooves. A slight decrease in the sizes of the deposits occurs at 30 minutes while the deposit-coverage increases. Interestingly, the deposits coalesce and form an encapsulating layer at 60 minutes, which has a weak adherence to the filament-surface and can therefore easily flake off as a result of a minimal mechanical disturbance. A SEM micrograph at a higher magnification of an individual deposit that occurred at 15 minutes is shown in figure 3.15. According to the XRD analysis presented in figure 3.5, the roughened surface underneath the deposit corresponds to the WC phase. The EDS spectrum shown in figure 3.16 reveals that the deposit is carbonaceous, in agreement with results by Moustakas [3.5]. More specifically, the deposit consists of graphitic-like carbon according to the XRD analysis presented in figure 3.5. The layer labelled X in the SEM micrograph presented in figure 3.17 has a sheet-like structure as shown. Furthermore, this layer is carbonaceous according to the EDS analysis presented in figure 3.18.

The SEM micrographs shown in figure 3.14 corroborate well with the XRD analysis. At 5 minutes the weight percentage of the carbonaceous deposits relative to the underlying carburized layer is lower than the measuring limit of the diffractometer. However, the increase in the size of the deposits at 15 minutes creates a pronounced intensity of the graphite peak. The decrease in the size of the deposits and consequently the intensity of the graphite peak at 30 minutes may be attributed to the etching effect of atomic hydrogen on graphitic carbon, in accordance with the results of Sommer *et al.* [3.9].

Disturbing the graphite-like carbon layer by breaking a piece off from the filament for analysis results in it flaking off from the filament-surface. This accounts for the drastic decrease in the intensity of the graphite peak at 60 minutes as showed in figure 3.5.
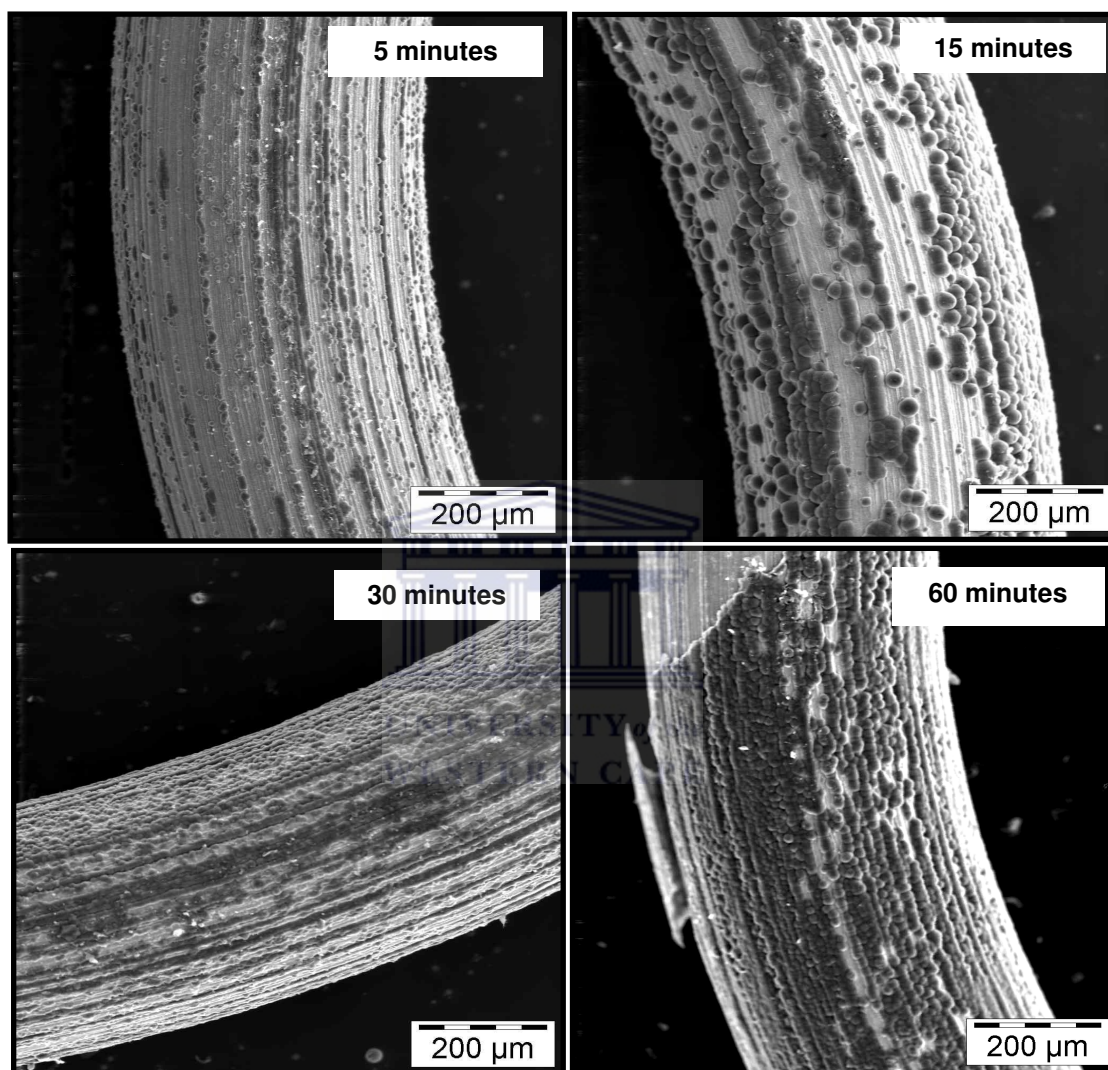

Figure 3.14: *SEM images showing the surface of a W-filament carburized for different durations at a temperature of 1600 °C*
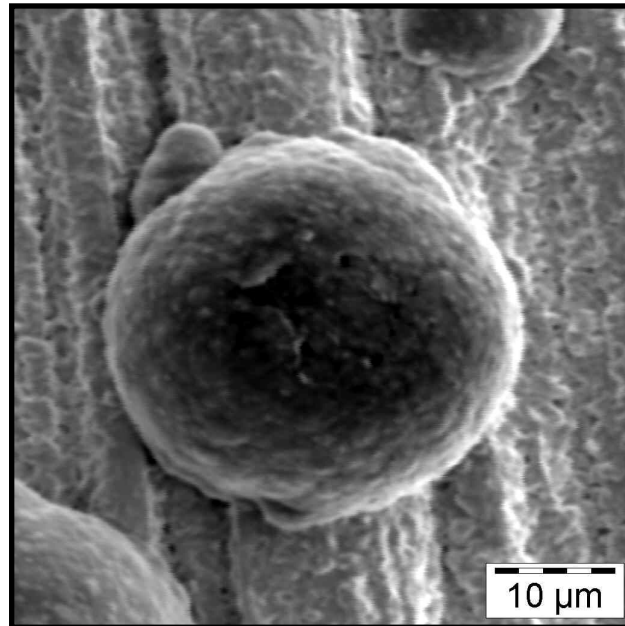
Figure 3.15: *An SEM micrograph showing the morphologies of an individual deposit and the underlying, roughened WC surface*

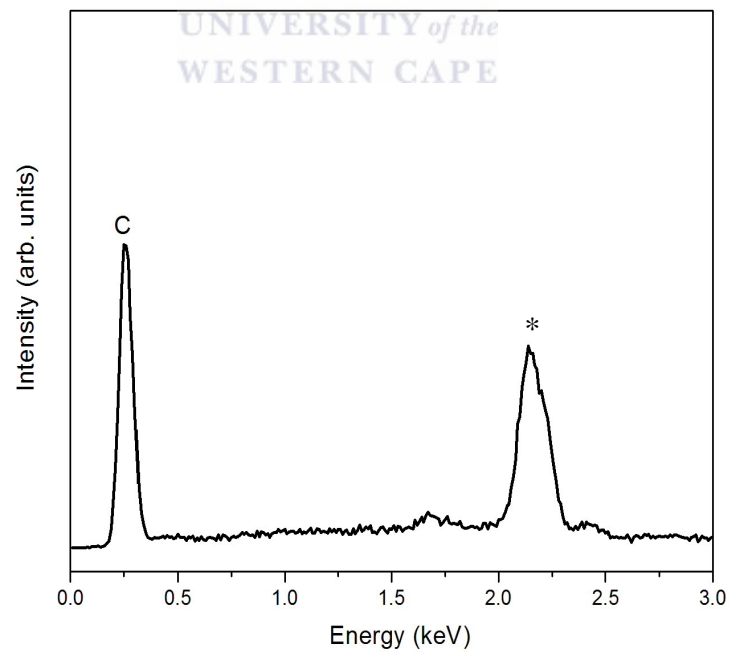**Figure 3.16:** *An EDS spectrum showing that the hemispherical deposit presented in figure 3.15 is carbonaceous. The peak labelled with "*" corresponds to the sputtered gold used as a conductive coating.*
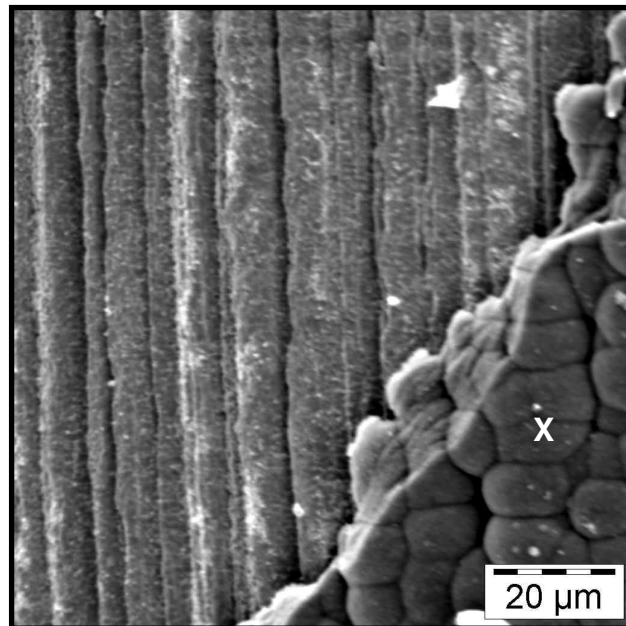
Figure 3.17: *SEM micrograph showing the sheet-like structure of the encapsulating layer (labelled X) at 60 minutes*
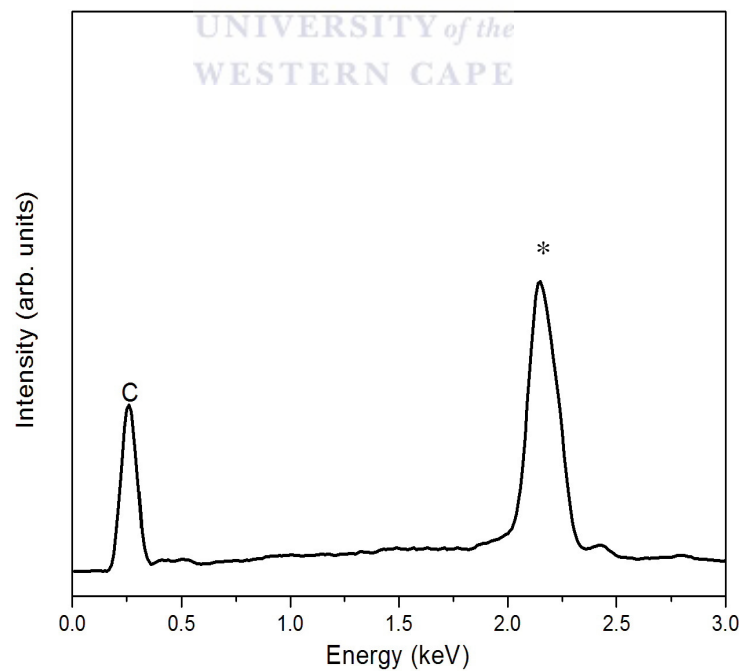

Figure 3.18: *The elemental composition of the encapsulating layer shown in figure 3.17*

Metallographic cross-sections of the W-filament carburized at 1600 °C for different times are shown in figure 3.19. At 5 minutes a W_2C + WC layer approximately 20 μm thick is present at the edge. However, at 15 minutes no carbide can be observed at this magnification. A higher magnification SEM micrograph presented in figure 3.20 shows that a W_2C + WC layer approximately 40 μm is present at the edge. The thickness of the carbide layer increased to approximately 50 μm at 30 minutes and the carbonaceous deposits are seen at the outer regions of the cross-section. Most interestingly, there seem to be brighter areas within the bulk material, indicating that C is less prominent at these regions. Surprisingly, the diameter of the carburized filament at 60 minutes appears to be smaller than at lesser exposure times, possibly due to the carbide layer being flaked off during sample preparation.

Kromka *et al.* [3.12] stated that carbon may be in different dissolved states within carbides to account for the behaviour in their resistance versus time curves. Based on this result, it is proposed that C was less dissolved at some areas resulting in brighter regions within the carbides. Switching off the electrical power to the filament ensured its rapid down-cooling and therefore increased the chances of actually "freezing" the carburization process. At 15 minutes, the C is homogenously dissolved within the first 40 μm of the filament-surface. At 1400 °C the diffusion rate of C within the carbides and W regions is slower than at higher filament-temperatures according to the XRD results. This ensures a stable rate of C-diffusion within the different phases and therefore a faster transition from the brighter areas to a more homogenous carbide region. Zeiler *et al.* [3.6] did not observe the brighter areas because they worked at 2450 °C. At this temperature the diffusion rate of C is high, which encourages a more homogenous carbide layer.
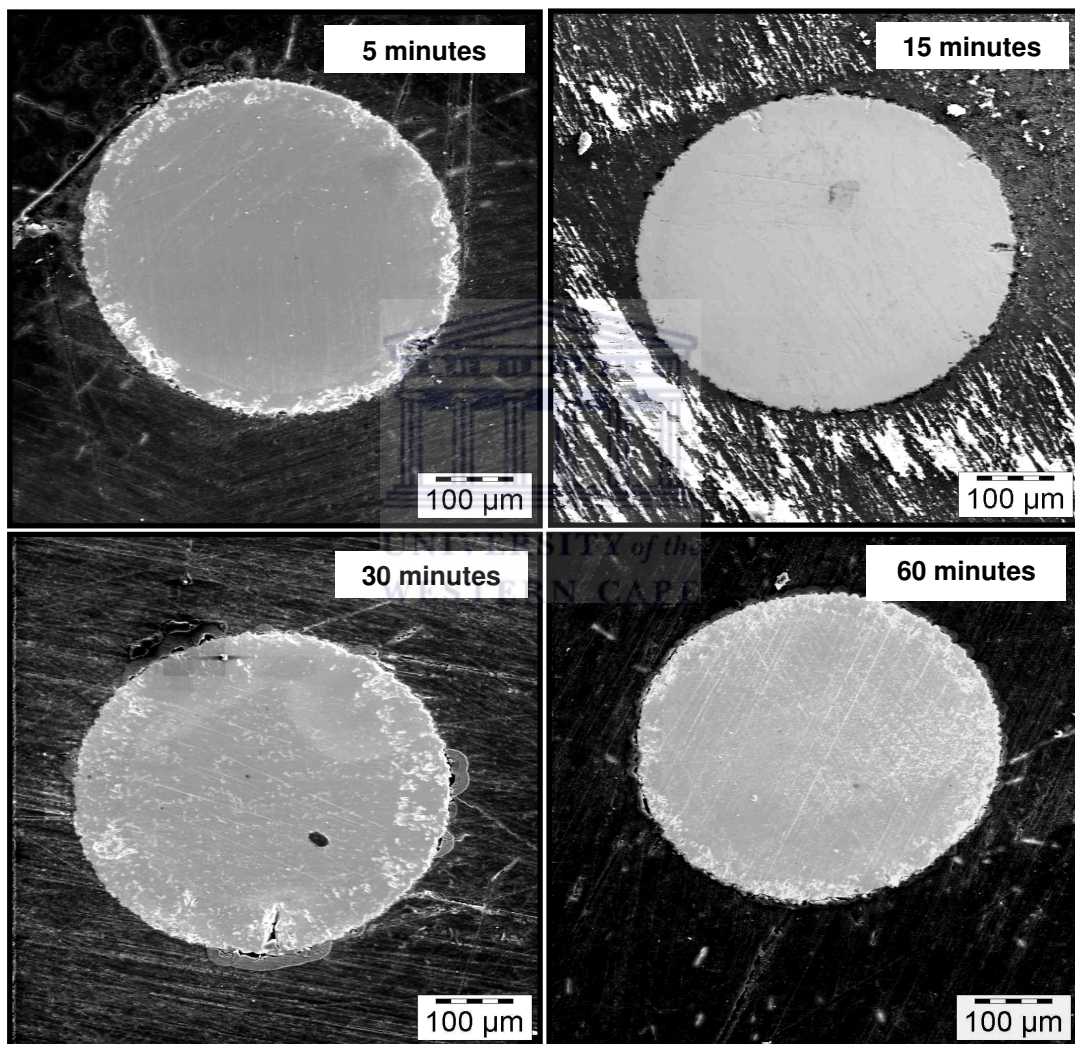
Figure 3.19: *Metallographic cross-sections showing the internal structure of the carburized W-filament at 1600 °C for different exposure times*
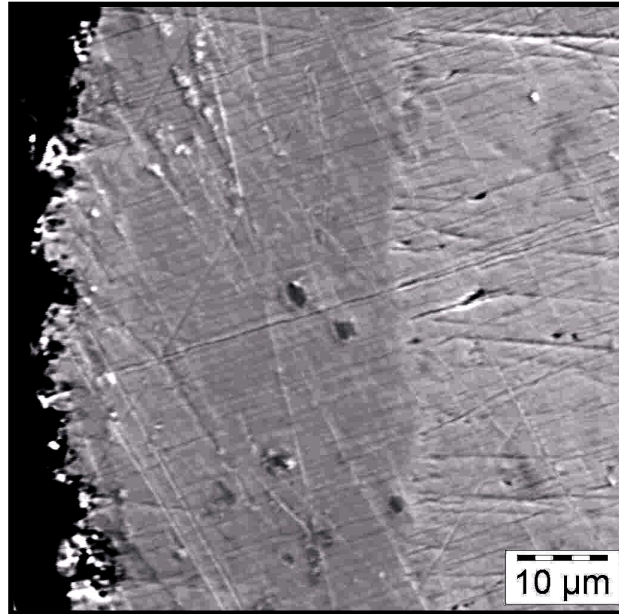
Figure 3.20: *A higher magnification image showing the edge of the cross-section at 15 minutes showing an approximately 40 µm thick W_2C + WC layer at the perimeter*

Figure 3.21 presents SEM micrographs showing the morphological evolution of the filament-surface carburized at a temperature of 1800 °C. Within the first 5 minutes a crack formed at the surface. Furthermore, no deposits are present on the surface of the filament at 5 minutes. The SEM micrograph presented in figure 3.22 reveals that inside the crack the filament crystals re-align themselves perpendicular to the filament-axis. Moustakas [3.5] stated that this crystal rearrangement is indicative of a diffusion based growth mechanism during carburization. The deposits appear at 15 minutes and have diameters of approximately 40 μm. The deposits increased in size to 110 μm at 30 minutes, accounting for the pronounced graphite peak observed in figure 3.6. At 60 minutes the deposits decreased in size and formed an encapsulating layer, similar to 1600 °C. A region where the layer flaked off reveals the presence of a crack on the surface of the filament.
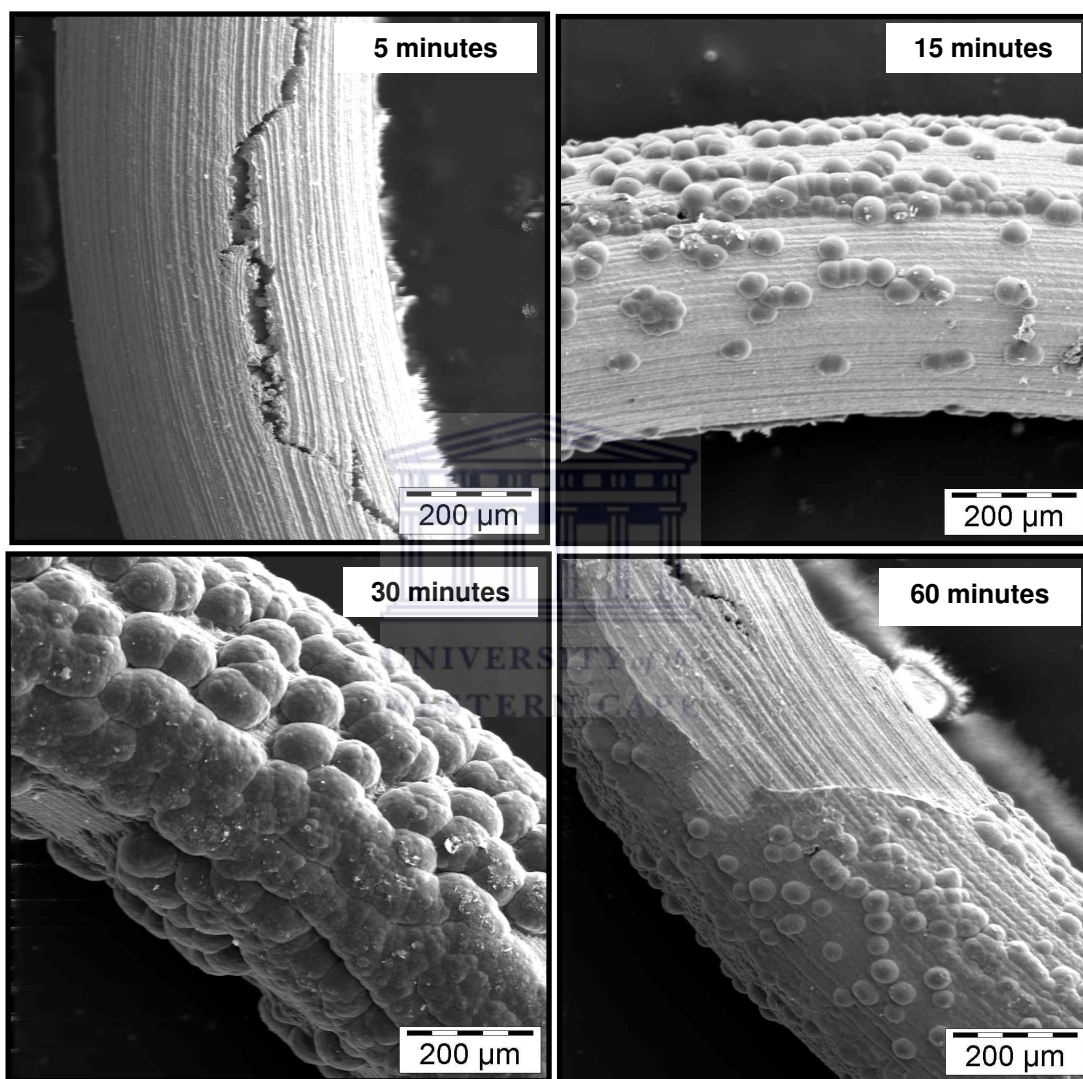
Figure 3.21: *The W-filament after being carburized for different durations at 1800 °C*
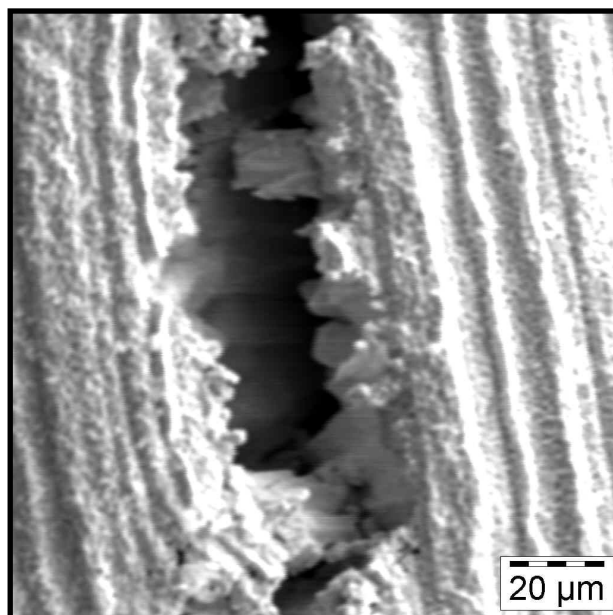
Figure 3.22: *SEM micrograph of the crack on the filament-surface carburized for 5 minutes at 1800 °C*

The formation of cracks at a filament-temperature of 1800 °C indicates that much thicker carbides have formed. This is in agreement with results by Zeiler *et al.* [3.6]. Furthermore, operating the filament at 1800 °C might have resulted in a larger thermal expansion compared to lower filament-temperatures. As argued earlier, the CH_4 dissociation rate is higher at a filament-temperature of 1800 °C than at lower temperatures. This resulted in the drastic increase in the size of the carbonaceous deposits at 30 minutes. It appears from figures 3.14 and 3.21 that the C layer reaches a certain thickness and then is etched by atomic hydrogen. In addition, with time the rate of C-accumulation increases again and subsequently the deposits form an encapsulating layer. Figure 3.23 confirms that thicker carbide layers formed within the filament. Moreover, the SEM micrographs show that the cracks extend from the perimeter to the interface of the carbide and the W-inner core. Noticeable in the micrographs are the brighter areas corresponding to carbide regions with a lower C content. The diameter of the filament at 5 and 15 minutes is approximately 510 μm. The carbide layers at 5 and 15 minutes have almost the same thickness of approximately 120 μm, indicative of a slow growth rate.

At 30 minutes the thickness of the carbide increased slightly to approximately 140 μm. Moreover, cracks extend right through the filament and the concentration of the brighter regions decreased. The diameter of the filament increased to approximately 550 μm at 30 and 60 minutes. Furthermore, the graphite layer is not present in the micrographs shown in figure 3.23. As mentioned earlier, the graphite-like carbon layer is easily disturbed from the filament-surface when a piece of the filament is broken off for analysis.
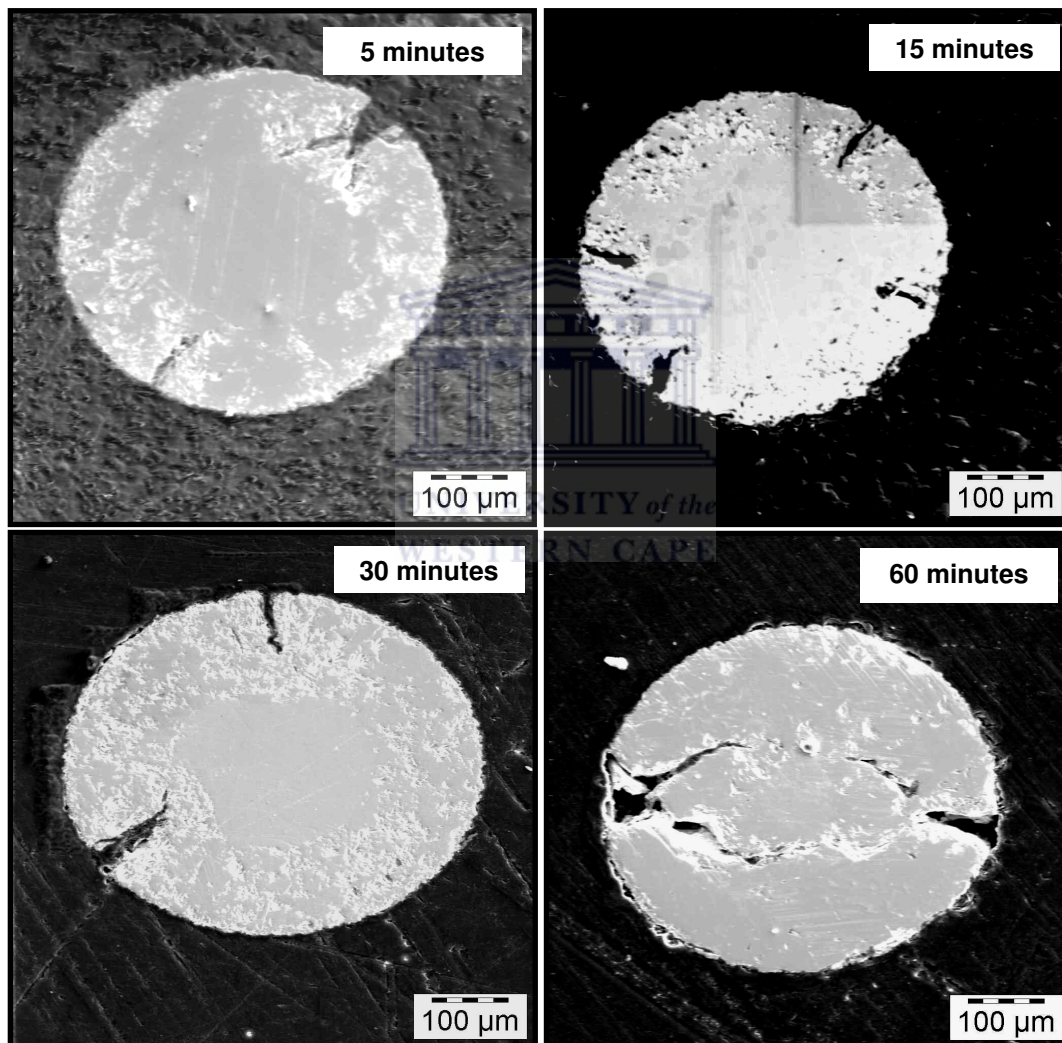

Figure 3.23: *Metallographic cross-section of the W-filament carburized at 1800 °C for different times*

According to Davidson *et al.* [3.8], the crack formation is due to the increase in the tensile stress at the outer region of the filament resulting from the volume expansion during carburization. In contrast to results by Kromka *et al.* [3.12], there are few cracks present within the carbides. Zeiler *et al.* [3.6] found that a filament which is much harder than a normal W-filament exhibits only a single crack during carburization. Furthermore, the diameter of the filament did not increase profusely during the carburization, confirming the superior hardness of the W-filament used in this study. The extension of the cracks right through the filament is a clear indication that the filament is completely carburized at 60 minutes, in accordance with results by Zeiler *et al.* [3.6].

Figure 3.24 shows that a much wider crack formed during the first 5 minutes at 2000 °C. Similar to 1800 °C, inside the crack it is apparent that crystal re-growth occurs, during which the crystals of the filament re-aligned themselves perpendicular to the filament axis. Interestingly, at 15 and 30 minutes the deposits grow preferentially inside and along the crack. Furthermore, at 30 minutes the crack does not have the same thickness throughout.

The EDS analysis shown in figure 3.25 reveals that the deposits inside the crack at 30 minutes are carbonaceous. At 60 minutes the filament is grossly deformed because deposits with sizes in excess of 200 μm formed on the surface. This layer is the graphite layer identified by the XRD analysis in figure 3.7.
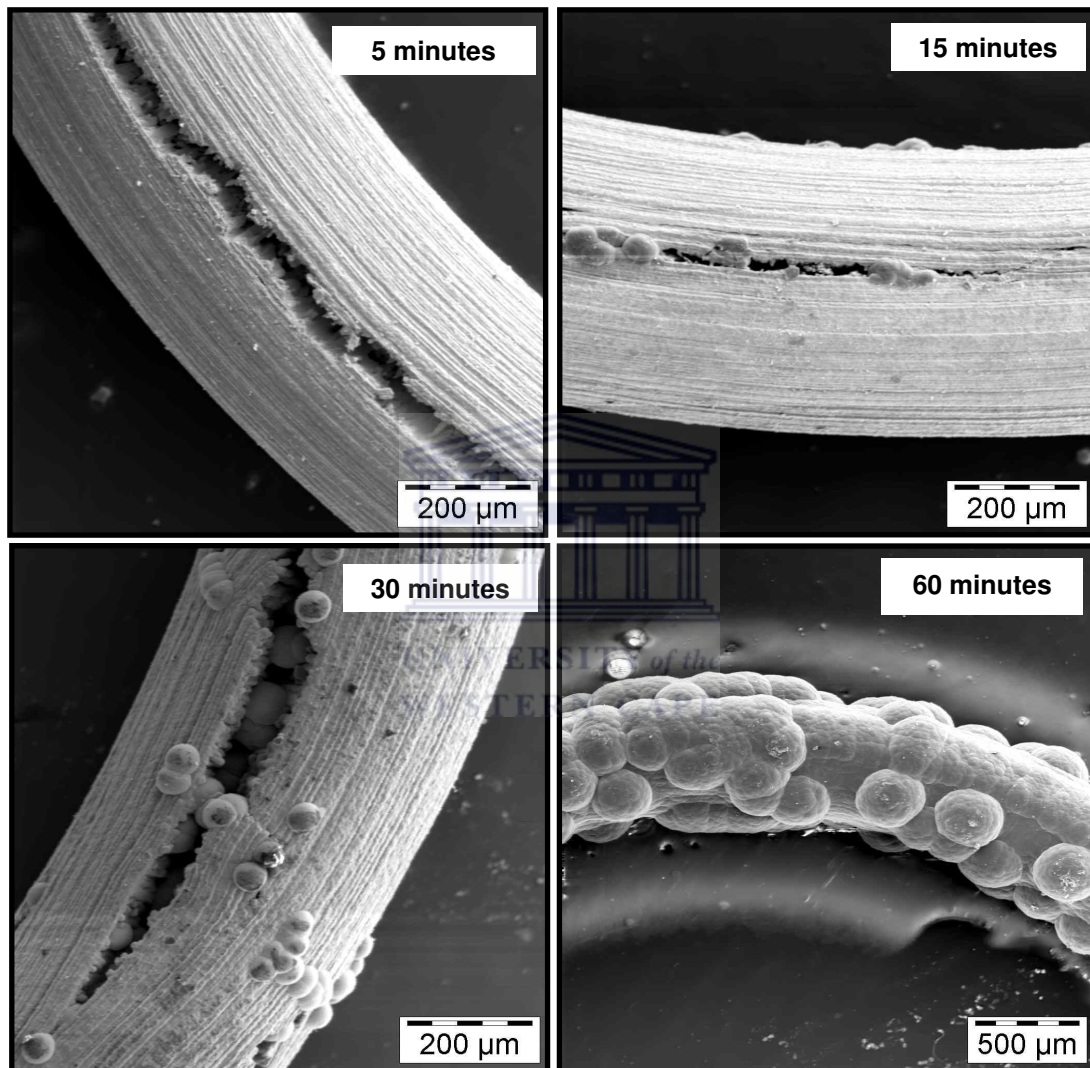
Figure 3.24: *SEM micrographs showing the surface of the W-filament carburized at 2000 °C for different durations*
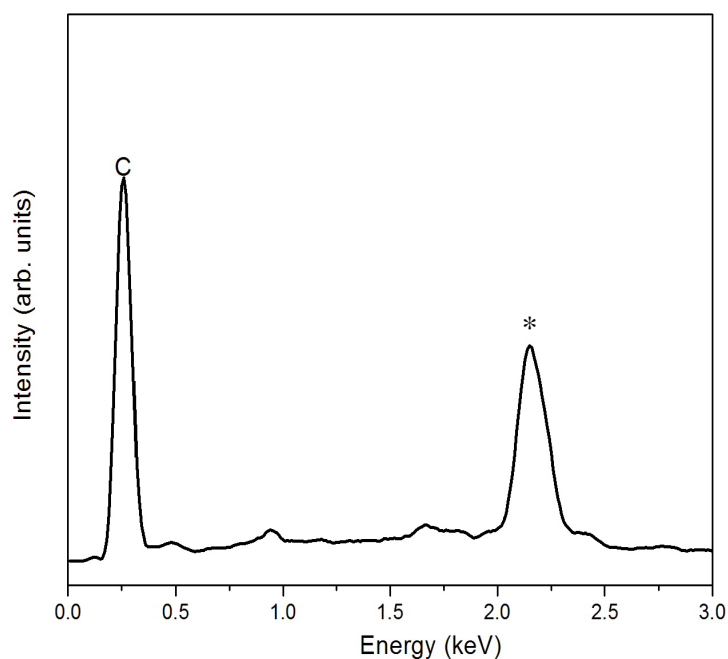
Figure 3.25: *An EDS spectrum of the deposits inside the cracks at 30 minutes*

Figure 3.24 reveals that the formation of cracks has an influence on the diffusion rate during carburization as described in *Section 3.3.2*. This result is in accordance with findings by Zeiler *et al.* [3.6], who stated that the C-diffusion paths are shortened at the cracks. Therefore, the preferential growth of the deposits in and along the cracks is attributed to shorter diffusion paths. Consequently, this leads to a more enhanced C-accumulation rate on the surface and therefore the faster rate of deposit formation. Furthermore, it was put forward that during the first 5 minutes the stability of the filament decreases as a function of temperature, due to the increase in the W_2C content of the filament-surface, as showed in figure 3.8. This can clearly be seen in the formation of cracks at 5 minutes corresponding to the formation of W_2C, which has a much larger unit cell than W [3.16]. The instability of the filament carburized during the first 5 minutes at 2000 °C is confirmed by studying the internal structure of the filament presented in figure 3.26. Large cracks form during the first 5 minutes and the diameter of the filament increases to approximately 520 μm at 15 minutes. Bright areas are present within the bulk material during the first 30 minutes. Furthermore, the carbonaceous deposits are also noticeable on the edges at 30 minutes. Strangely, the diameter at 30 minutes is smaller than at 15 minutes.

Referring to figure 3.24, it can be seen that the size of the crack at 30 minutes is not constant throughout. This means that at some regions the diameter of the filament is not the same. The higher contrast at the cracks at 30 minutes substantiate that the C-diffusion paths are indeed shortened at these regions. At 60 minutes the filament is covered with a layer approximately 200 μm thick, similar in size to the deposits observed on the surface at this time. This results in an increase in the diameter of the filament to approximately 750 μm. The layer is carbonaceous as shown in the EDS spectrum in figure 3.27. Similar to 1800 °C, at 60 minutes the cracks extend through the filament, indicative of a fully carburized filament.

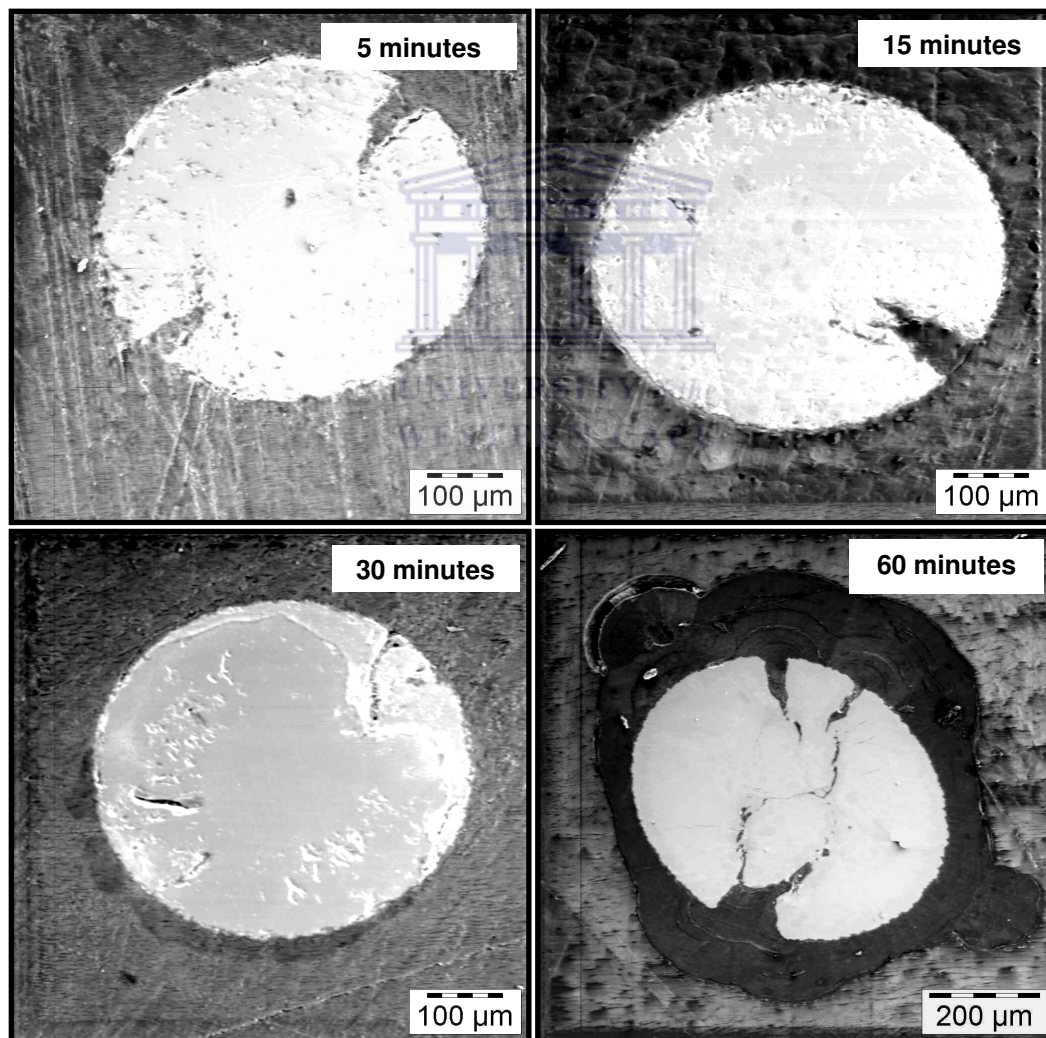**Figure 3.26:** SEM micrographs showing the internal structure of the filament as a function of time at 2000 °C
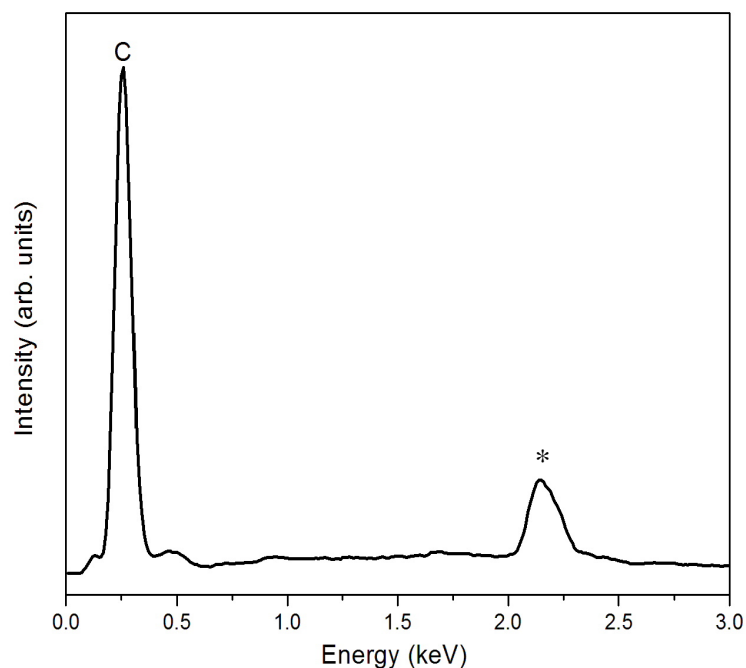
Figure 3.27: *An EDS spectrum showing that the outer layer is carbonaceous, more specifically graphite-like carbon according to the XRD analysis*

The morphological studies confirm the XRD analysis that the structural properties of the filament change as a function of temperature and exposure time. Metallographic cross-sections showed different regions of different brightness and structure, corroborating with the XRD analysis and previous studies [3.4 – 3.9] that concluded on the formation of carbides at the surface. The thickness of the W_2C + WC layer increase with time, suggesting that the diffusion of C becomes more difficult. Complete filament carburization occurs at 60 minutes for filament-temperatures at and above 1800 °C. The appearance of the carbonaceous deposits on a roughened WC surfaces signals the onset of "filament poisoning". This leads to an encapsulating graphite layer that prevents direct contact between the CH_4 / H_2 molecules and the catalytic surface of the filament. At 1600 °C the deposits develop within the first 5 minutes whilst at 1800 °C they form at 15 minutes. The coverage of the deposits during the first 30 minutes is much lower at 2000 °C, suggesting that the C-etching rate by atomic hydrogen hinders the growth of the deposits, in accordance with results by Sommer *et al.* [3.9].

The deposits initially decrease in size and then form an encapsulating layer at 60 minutes for filament-temperatures at 1600 °C and 1800 °C. In some case the graphite layer flaked off from the layer because of mechanical disturbance when a piece was broken off from the filament. This resulted in a decrease in the XRD intensity of the graphite peak. The morphological studies substantiate the XRD analysis that a filament-temperature of 1400 °C is an optimum deposition temperature. At this temperature no carbonaceous deposits nor any encapsulating graphite-like carbon layer or crack formed below the first 30 minutes of exposure. This ensures a stable WC surface which is vital for a stable HWCVD synthesis of CNTs in a CH_4 containing ambient. Past studies [3.6 and 3.12] have shown that the changes in the structural properties of a carburized filament can be monitored by studying the resistance of the filament as a function of deposition time. Furthermore, the temperature of the filament depends on the condition of its surface. These two factors will be considered in the following section.

3.3.4 Resistance and temperature measurements

Each phase that forms during carburization has a characteristic resistivity. This means that the resistance of the filament as a function of time may be used to monitor its carburization process. Figure 3.28 shows the resistance versus time curves when the filament was operated at different temperatures for 60 minutes. The error in the measurements was taken as the power supply sensitivity of 5 % for both voltage and current, and 0.3 % for the resistance. At a filament-temperature of 1400 °C, the resistance increased to a maximum of 1.09 Ω during the first few minutes and remained relatively constant until 30 minutes. However, at 1600 °C the resistance of the filament shows a stepwise drop to a final value of 0.82 Ω at 60 minutes. At temperatures of 1800 °C and 2000 °C the resistance undergoes a rapid increase in the first few minutes of deposition. The resistance of the filament reached a maximum of 1.49 Ω at 5 minutes and 1.80 Ω at 90 seconds for filament-temperatures of 1800 °C and 2000 °C, respectively. The resistance then decreases between 5 - 8 minutes at 1800 °C and 90 seconds to 3

minutes for 2000 ℃. Interestingly, the resistance recovers slightly around 12 minutes at 1800 °C and around 6 minutes at 2000 °C, subsequently decreasing until 60 minutes in both cases. It was noticed that the resistance at 2000 ℃ decreases at a faster rate after 10 minutes compared to other temperatures. The behaviour of the resistance versus time curves can be accounted for based on the phase transitions and morphological changes presented in the previous sections. In this regard, the circles in figure 3.28 show changes in the slope of the curves. These changes reveal transitions in the structural properties of the filament that occurred during carburization.
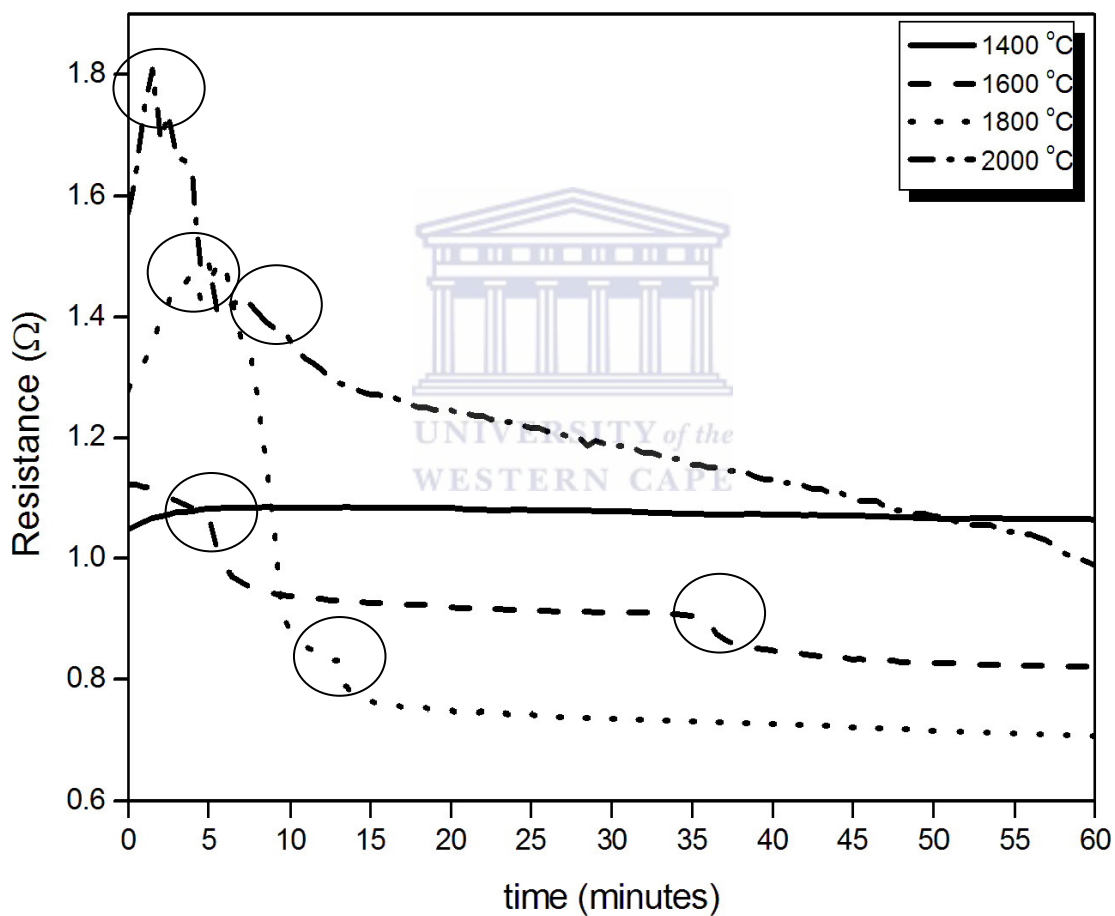

Figure 3.28: *Resistance versus time curves when the W-filament was carburized at different temperatures*

The increase in resistance during the first 5 minutes at T_{fil} = 1400 °C, 1800 °C and 2000 °C correspond to the formation of W_2C, which has a higher resistivity than W and WC [3.6]. In addition, cracks also formed during the first 5 minutes at and above 1800 °C, contributing to an increase in the resistance. However, after 5 minutes the WC phase becomes thick enough to result in a decrease in the resistance at 1800 °C and 2000 °C, which is why the slope of the curve changes around this point. This result agrees well with the SEM and XRD analysis. At 1400 °C, the thickness of the WC layer is not sufficiently high enough to cause a noticeable drop in the resistance of the filament. The decrease of the resistance within the first 5 minutes at 1600 °C is a result of the carbonaceous deposits on the surface of the filament. Around 10 minutes for temperatures at and above 1800 °C, cracks formed again at some regions of the filament, resulting in a slight increase in the resistance. This is evident from figure 3.23, which showed that at 15 minutes more cracks were noticeable whilst at 30 minutes there were fewer cracks. Nevertheless, with time the cracks are filled by carbonaceous deposits, leading to the sudden drop in resistance. Afterwards, the resistance decreases because of the growth of the solid carbon layer. The rate of resistance drop is higher for 2000 °C because of the rapid evolution from a W_2C surface to a WC phase after 15 minutes. A rapid transition from a surface partially covered by deposits to an approximately 200 μm thick graphite-like carbon layer also occurs, as shown by figure 3.24, further contributing to the rapid decrease.

Figure 3.20 showed that after 30 minutes at 1800 °C the carbonaceous layer decrease in size because of atomic hydrogen etching. Consequently, the drop in resistance at 1800 °C is not as rapid as at 2000 °C. As was shown in figure 3.14, the deposits decrease in size at 30 minutes for a carburization temperature of 1600 °C. This was attributed to the etching effect of atomic hydrogen. This argument is reinforced by considering the relatively constant resistance between 15 and 35 minutes.

Subsequently, at 35 minutes the carbonaceous deposits started to combine to form an encapsulating layer. This leads to the sudden decrease in the resistance around this time. It is apparent from the relatively constant resistance after the sudden drop at 40 minutes that the solid C layer formed rapidly but seems to grow at a slower rate afterwards. The same can be deduced for 1800 °C after 15 minutes.

During the deposition process, the temperature of the filament plays a key role by contributing to the reactions between the filament and the gases that generates the gas phase species for material growth. However, during carburization at T_{fil} = 1400 °C and 1600 °C, the filament-temperature dropped at 60 minutes to final values of 1396 °C and 1521 °C respectively. At T_{fil} = 1800 °C and 2000 °C the filament-temperature dropped more considerably to final values of 1486 °C and 1719 °C, respectively. The temperature of the filament as a function of the deposition time is presented in figure 3.29.
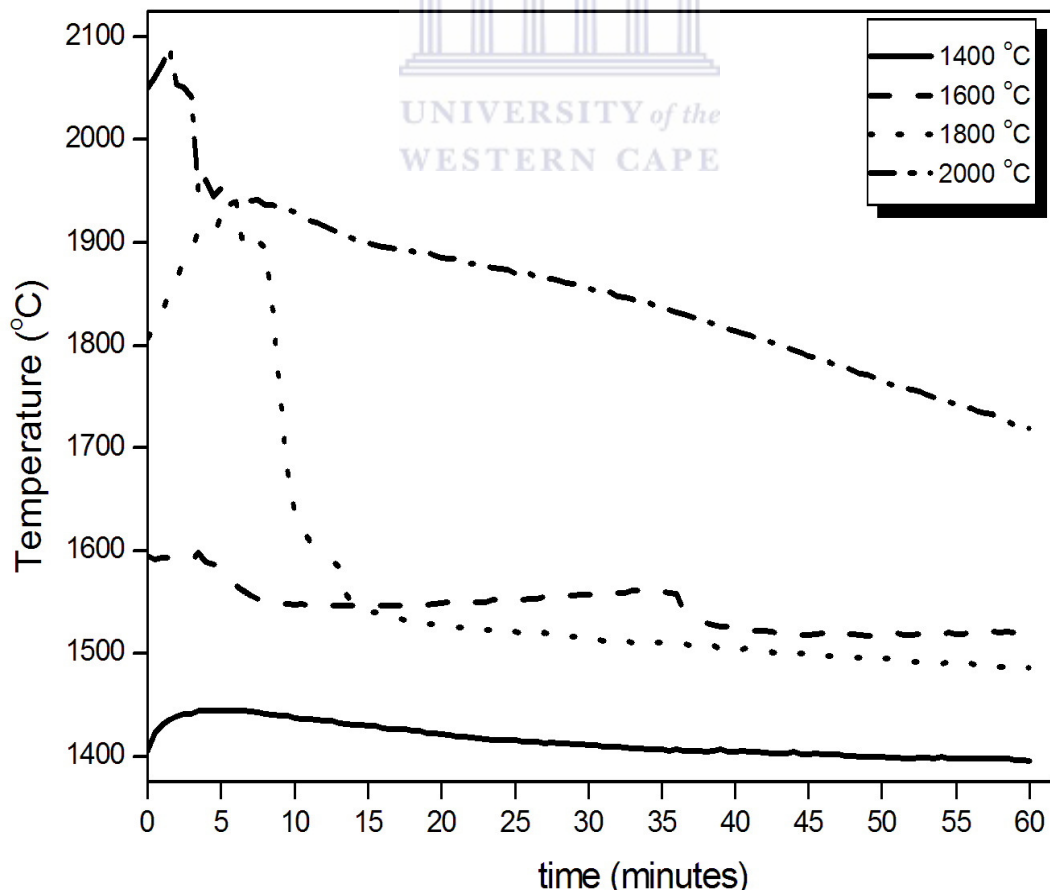

Figure 3.29: *A plot of the filament-temperature versus carburization time*

The plot presented in figure 3.29 has a similar behaviour to the resistance curves shown in figure 3.28, i.e. changes in slopes occur at the same time. This is expected since the W_2C phase with its higher resistivity requires a higher power input to maintain the same current. Afterwards the potential difference over the filament reduces since WC and graphite have lower resistivities. Since the power supply operates in a constant current this result in a drop in the power output. Interestingly, at 1600 °C between 15 and 35 minutes the temperature of the filament increased slightly. As outlined in the previous chapter in *Section 2.2.3*, it was found that T_{fil} varies linearly with the current in a pre-deposition pressure of 30×10^{-3} Torr. However, figure 3.29 clearly shows that during carburization at a constant current the temperature of the filament varies with time. The drop in the temperature of the filament is explained as follows.

Due to the conservation of energy, the electrical power input (P_E) must equal the power dissipated by the filament. The filament dissipates P_E via four mechanisms comprising of the power lost to thermal radiation (P_{RAD}), the power lost to gas convection (P_{CONV}), conduction via the electrical contacts (P_{COND}) and the dissociation of the hydrogen molecules (P_H). The mechanisms are related to P_E through the energy balance expressed in equation (3.1):

$$P_{input} = P_E = P_{COND} + P_{CONV} + P_{RAD} + P_H \qquad (3.1)$$

The power lost to radiation depends on the filament-temperature (T_{fil}), the emissivity of the surface (ε) and the filament surface area (A) as given by:

$$P_{RAD} = \sigma \varepsilon A T_{fil}^{4} \qquad (3.2)$$

where σ is the Stefan–Boltzmann-constant (5.7×10^{-8} W m^{-2} K^{-4}). A filament that is covered completely with graphite has a surface emissivity of 0.95 [3.6].

In this study at T_{fil} = 2000 °C, the electrical power supply to filament was initially 600 W and the area of the filament was approximately 2.45 x 10^{-4} m^2. The calculated radiation power density Q_{RAD} is given by equation (3.3):

$$Q_{RAD} = P_{RAD}/A = IV/A \qquad (3.3)$$

where V and I are the applied potential difference and the current flowing through the filament, respectively. The power lost to radiation for a filament covered with graphite according to equations (3.2) and (3.3) is Q_{RAD} = 1.45 x10^6 Wm^{-2} and is in the same order of magnitude to the applied electrical power density Q_E = 2.45 x10^6 Wm^{-2}. Zeiler *et al.* [3.6] reported similar results and stated that the energy transport via convection and conduction are insignificant and may be neglected henceforth.

The power dissipation during the dissociation of hydrogen molecules at the filament-surface is given by [3.6]:

$$P_H = n \ (T_{fil}, p)\gamma(T_{fil}) \ E_{diss} A \qquad (3.4)$$
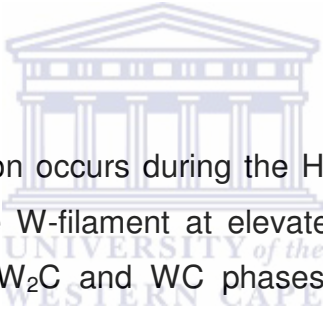
where *p is the pressure,* $n(T_{fil}, p)$ is the number of collisions between the H_2 molecules and the surface of the filament per unit time and area, $\gamma(T_{fil})$ is the probability of H_2 dissociation and E_{diss} represents the bonding energy of a H_2 molecule, which is 4.5 eV. Re-arranging equation (3.1) yields the power dissipation by the filament:

$$P_E = P_{RAD} + P_H = \sigma\varepsilon A T_{fil}^{4} + n \ (T_{fil}, p)\gamma(T_{fil}) \ E_{diss} A \qquad (3.5)$$

Equation (3.5) shows that the decrease in the temperature of the filament can be brought about by an increase in the area of the filament, the formation of phases with higher emissivities than a W-surface and an increase in the probability of H_2 dissociation. It was shown in the previous sections that the formation of carbides and graphite occurs. This results in an increase in the radiating area and the surface emissivity of the filament-surface.

This is in accordance with results by Zeiler *et al.* [3.6] and Sommer *et al.* [3.9]. In the period from 15 to 35 minutes at 1600 °C a decrease in the size of the deposits occurred, which results in a decrease in the emissivity of the surface and consequently an increase in the temperature during that interval of time. Furthermore, when the surface is not covered with graphite an increase in the probability of H_2 dissociation occurs at the surface of the filament. Collectively, these changes result in an increase of power loss to radiation and H_2 dissociation, leading to the observed decrease in the temperature of the filament. The XRD results, the morphological studies, the filament-resistance and temperature measurements all suggest that a filament-temperature of 1400 °C is the ideal deposition temperature required for a stable synthesis of CNTs using the HWCVD technique.

3.4   Conclusion

Filament carburization occurs during the HWCVD of CNTs due to the incorporation of C into the W-filament at elevated filament-temperatures. It was found that both the W_2C and WC phases formed during the first 5 minutes at and below filament-temperatures of 1800 °C. This is much faster than previously reported [3.3 - 3.9] and was attributed to the much higher CH_4 concentration used in this study. When the filament was operated at 2000 °C only the W_2C phase was detected by XRD at an exposure time of 5 minutes. It was suggested that during the first 5 minutes the etching rate of C by atomic hydrogen increased with temperature. Regardless of the high CH_4 dissociation rate, this led to a decrease in the C-accumulation rate and consequently an increase in the stability of the W_2C phase region. After 5 minutes the WC content in the surface of the filament increased, which indicated that the C-diffusion rate decreased with longer exposure times [3.8]. The slower C-diffusion rate also led to an increase in the C-accumulation rate. Consequently, this resulted in "filament poisoning", i.e. the formation of a solid graphite-like carbon phase at and above filament-temperatures of 1600 °C. This C layer reduces the contact between the precursor gases and the catalytically active filament surface.

The stability of the filament decreased with filament-temperature. It was found through the morphology and elemental analysis that cracks, carbonaceous deposits and ultimately an encapsulating graphite layer formed with longer exposure time at and above filament-temperatures of 1600 °C. Full filament carburization occurred after 60 minutes of exposure at and above filament-temperatures of 1800 °C.

It was possible to monitor the carburization process of the W-filament by using resistance versus carburization time curves. A model was developed that related the temperature changes to the properties of the filament namely the surface area, surface emissivity and the probability of H_2 dissociation on the surface.

Based on the results presented in this chapter, the optimal filament-temperature, as far as the stability of the structural properties of a carburized W-filament is concerned, was found to be 1400 °C. At this temperature, the filament undergone minimal structural changes and its electrical and thermal properties remained relatively constant, which ensured a stable deposition process.
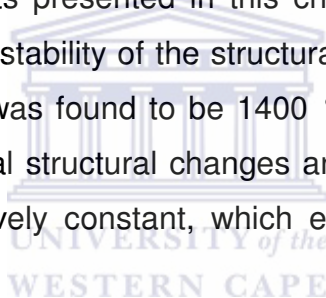
3.5 References

[3.1] E. Salernitano, T. D. Makris, R. Giorgi, N. Lisi, L. Pilloni, F. Sarto and M. Alvisi, *Diamond and Related Materials*, **13**, 305 (2004)

[3.2] A.C. Dillon, A.H. Mahan, J. L. Alleman, M. J. Heben, P.A. Parilla and K.M. Jones, *Thin Solid Films*, **430**, 292 (2003)

[3.3] S. Matsumoto, Y. Sato, M. Tsutsumi and N. Setaka, *J. Mater. Sci.*, **17**, 3106 (1982)

[3.4] H. Matsubara and T. Sakuma, *Journal of Material Science*, **25**, 4472 (1990)

[3.5] T. D. Moustakas, *Solid State Ionics*, **32-33**, 861 (1989)

[3.6] S. Schwarz, E. Zeiler, S. M. Rosiwal and R. F. Singer, *Materials Science and Engineering A*,**335**, 236 (2002)

[3.7] S. Okoli, R. Haubner and B. Lux, *Surface and Coatings Technology*, **47**, 585 (1991)

[3.8] C. F. Davidson, G. B. Alexander and M. E. Wadsworth, *Metallurgical Transactions A*, **10A**, 1059 (1979)

[3.9] M. Sommer and F. W. Smith, *J. Mater. Res.*, **511**, 2433 (1990)

[3.10] Joint Committee for Powder Diffraction Studies (JCPDS): W (89-3012), W_2C (79-0743), WC (89-2727) and graphite (75-1621)

[3.11] A. S. Kurlov and A. I. Gusev, *Inorganic Materials*, **42**, 121 (2006)

[3.12] A. Kromka, J. Janík, A. Šatka, J. Pavlov and I. Červeň, *Acta Physica Slovaca*, **51**, 359 (2001)

[3.13] E. Lamouroux, P. Serp and P. Kalck, *Catalysis Reviews,* **49**, 341 (2007)

[3.14] J-E Bourée, C. S. Cojocaru, D. Kim and D. Pribat, *Thin Solid Films*, **501**, 227 (2006)

[3.15] R. Sharma, P. Rez and M. M. J. Treacy, *Microsc Microanal*, **11**(Suppl 2), 212 (2005)

[3.16] E. K. Storms, "The refractory carbides", *Academic Press*, New York and London, p 147 (1967)

CHAPTER FOUR

MORPHOLOGY AND STRUCTURAL PROPERTIES OF CARBON NANOTUBES

4.1   Introduction

Since their discovery [4.1, 4.2], carbon nanotubes (CNTs) have become one of the most researched materials in the scientific community. Single-walled CNTs (SWCNTs) can be envisioned as graphene sheets wrapped seamlessly in a specific direction [4.3, 4.4]. On the other hand, multi-walled CNTs (MWCNTs) comprise of multiple SWCNTs enclosed in each other. These materials are one-dimensional structures that exhibit extraordinary properties. CNTs are ballistic conductors at room temperature, have a Young's modulus greater than 1 TPa and have a very high thermal conductivity [4.4]. These properties led to CNTs being identified as ideal candidates for improving the properties of different materials, for instance enhancing the performance of solar cells and the mechanical properties of polymers [4.5].

Currently, the synthesis of CNTs can be accomplished by various deposition techniques. Some of the most commonly used techniques are laser ablation, arc-discharge and chemical vapour deposition (CVD) [4.4]. However, because of its gas phase based mechanism, CVD is considered the most feasible route for a low cost and mass-production of CNTs. During the CVD synthesis of CNTs, a carbon precursor is dissociated by an energy source; e.g. microwaves. At the optimum deposition conditions, the carbon produced from the dissociation process then precipitates on nanoparticles in a tubular

form, i.e. CNTs. Unlike laser ablation or arc-discharge, it is possible to synthesise CNT aligned perpendicular to the substrate using CVD, which is important for applications such as field emission [4.4]. By introducing a heated filament to CVD, the synthesis method is referred to as hot-wire (HW) CVD. A heated transition metal filament acts as an efficient catalyst in dissociating the carbon precursor and hydrogen (H_2) into atomic hydrogen [4.6].

The optimum atomic hydrogen concentration was found to be vital during the synthesis because it decreases the concentration of impurities relative to CNTs and prevent the transition metal particles from becoming inactive during the deposition [4.7, 4.8]. Furthermore, the temperature of the filament determines the dissociation rate of the precursor gases, which leads to a more localised dissociation region. As a result, the hot-filament has the added advantage of catalytically producing more atomic hydrogen species as well as a more controlled concentration of hydrocarbon derivatives. However at elevated temperatures tungsten (W) filaments react with the carbon and are consequently converted into W-carbides. This process is known as carburization and it affects the catalytic action of the filament and reduces the carbon concentration in the deposition atmosphere, thereby influencing the entire deposition process. Moreover conclusive evidence has shown, in the previous chapter, that the carburization process is dependent on the exposure time and the filament-temperature. This implies that the reactive species released from the filament-surface will depend on the surface and temperature of the filament.

A conclusion can thus be made that the morphology and structural properties of the synthesised CNTs are dependent on the structural changes and temperature of the filament. Currently, there are no literature reports relating the temperature and the structural properties of the filament to the synthesised CNTs. This chapter will focus on how the temperature and structural properties of the filament affects the properties of the CNTs synthesised by HWCVD.

4.2   Experimental

Approximately 10 nm-thick nickel (Ni) thin films were deposited onto 1 $\times$ 1 cm^2, single-side polished, thermally oxidized silicon (100) substrates, using electron-beam deposition. The pre-deposition pressure in the Bell-jar system was approximately 10^{-7} Torr and increased to 10^{-6} Torr during the deposition process. The Ni-deposition rate amounted to 1.7 Å / s. The Ni / SiO$_2$ / Si substrates were then loaded into the HWCVD system approximately 10 cm away from the central, hottest part of the filament. Subsequently, the system was pumped down to a pre-deposition pressure of 30 mTorr. The substrates were then annealed at a temperature of 500 °C for 20 minutes in a 100 sccm H$_2$ ambient at 100 Torr with the aim of producing Ni-nanoparticles. The Ni-nanoparticles are nucleation sites for CNTs and the oxidised Si acts as a diffusion barrier preventing the formation of Ni-silicides [4.3, 4.9].

After the substrate annealing, 10 sccm methane (CH$_4$) and 100 sccm H$_2$ was introduced into the quartz tube. Once the pressure in the system reached 150 Torr, the tungsten (W) filaments were heated by supplying a dc electrical power until the desired temperatures of 1400 - 2000 °C (in increments of 200 °C) were attained. The deposition time amounted for 15 minutes for each filament-temperature. After the deposition, the samples were allowed to cool down to room temperature and then stored for analysis.

A MultiMode atomic force microscope (AFM) was operated in the tapping mode at ambient conditions and was used to determine the topography of the sample after annealing. Morphology studies of the deposited materials were performed using a LEO 1525 field emission scanning electron microscope (FESEM). The FESEM was operated at 6 kV and a working distance of 6 mm. Energy dispersive x-ray spectroscopy (EDS) was used to determine the elemental composition of the annealed substrate and the deposited material.

The structural properties of the materials were investigated using a Horiba Jobin Yvon HR800 micro-Raman spectrometer, where an excitation laser light of 514 nm wavelength was directed perpendicular to the sample. The power and the spot size at the sample surface amounted to 5 mW and 3 μm, respectively. The Raman spectra were collected in backscattered geometry in the region 100 – 3000 cm^{-1} with a spectral resolution of 0.33 cm^{-1}. The measurements were taken at different spots to determine the homogeneity in the structural properties of the synthesised materials.

4.3   Results and Discussion

Figure 4.1 shows the SEM micrographs of the sample before and after it was annealed at 500 °C. Before the annealing, the thin film is smooth and covers the entire substrate. Large, irregular shaped agglomerates with sizes ranging from ∼ 50 – 200 nm are present after the annealing process. This indicates that the substrate annealing was successful in creating the required nanoparticles. Presented in figures 4.2 and 4.3 are an AFM three-dimensional (3D) image and a line scan over an area of the substrate, respectively. The nanoparticles are approximately 70 – 90 nm high and have a wider base compared to the height. The nanoparticles form due to the surface tension in conjunction with the establishment of thermal stresses owing to a difference in thermal expansion coefficients of Ni and SiO_2 during annealing [4.11, 4.12]. This accounts for the wider particle base compared to its height. During annealing the nanoparticles may also coalesce to form the observed larger agglomerates, a process referred to as Ostwald ripening [4.7]. Figure 4.4 presents EDS spectra normalized to the Si peak of the substrate prior to and after the annealing. The higher intensities of O and Si correspond to the underlying SiO_2 support whilst the lower Ni-intensity corresponds to the nanoparticles.
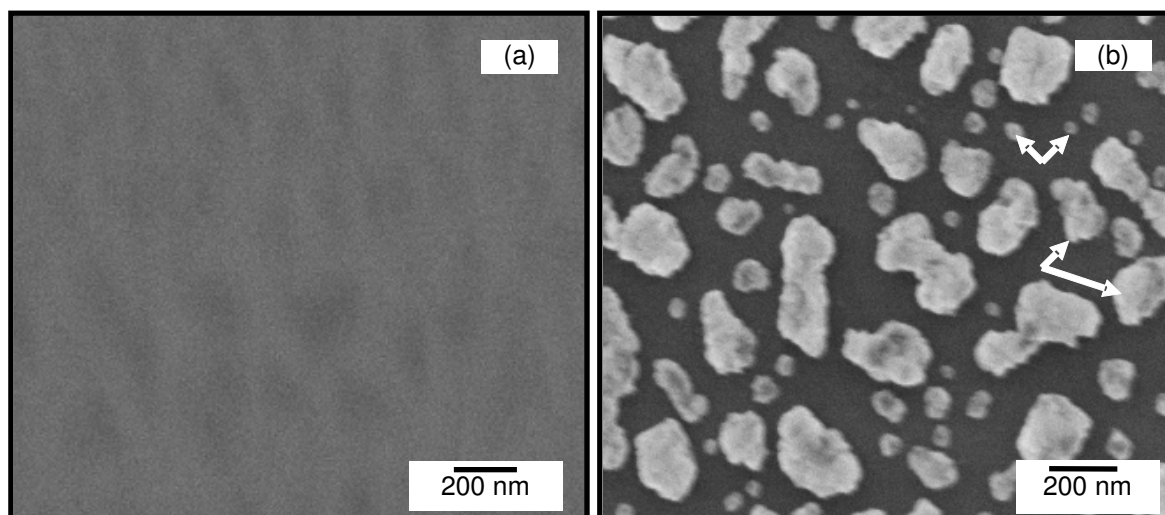
Figure 4.1: *SEM micrographs before (a) and after (b) annealing the substrate at 500 ℃*
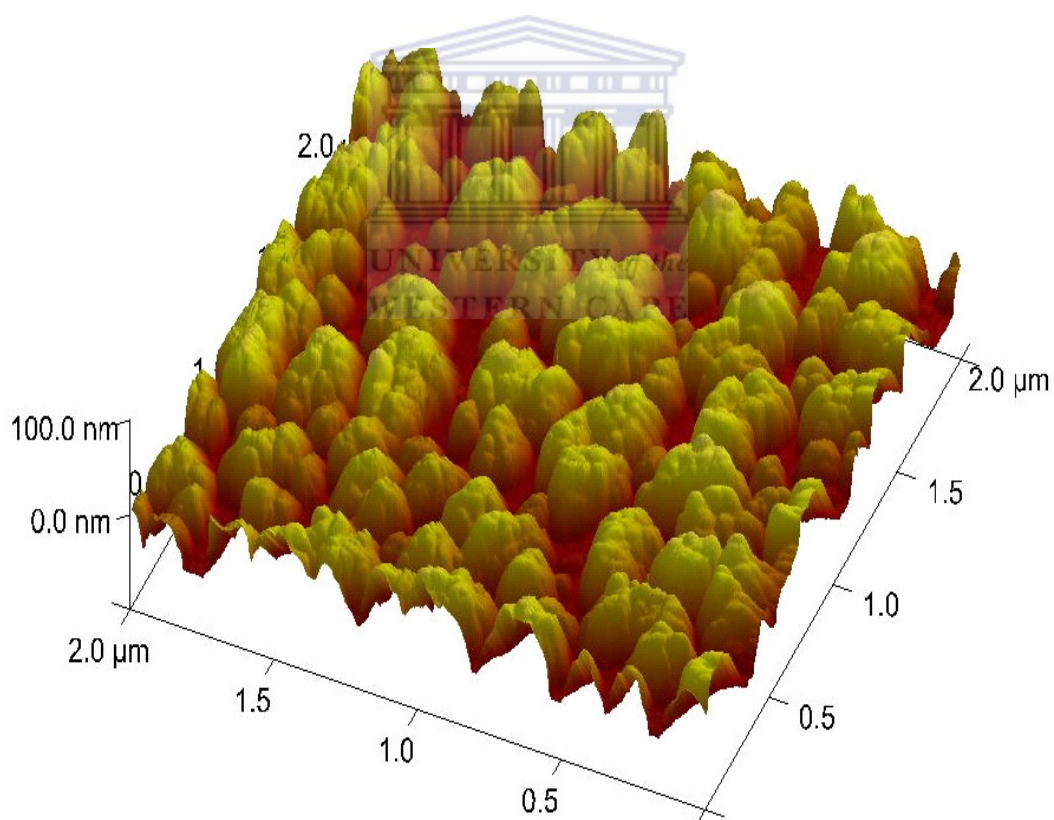

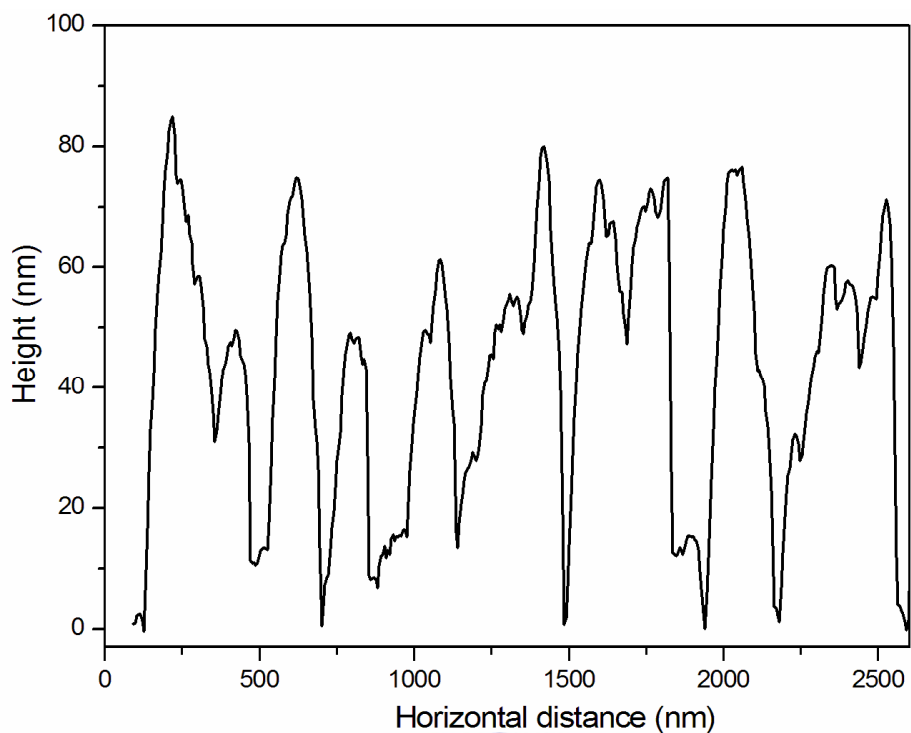**Figure 4.2:** *AFM 3D image of the annealed substrate*

Figure 4.3: *A line scan showing the height and width of the particles shown in figure 4.2*
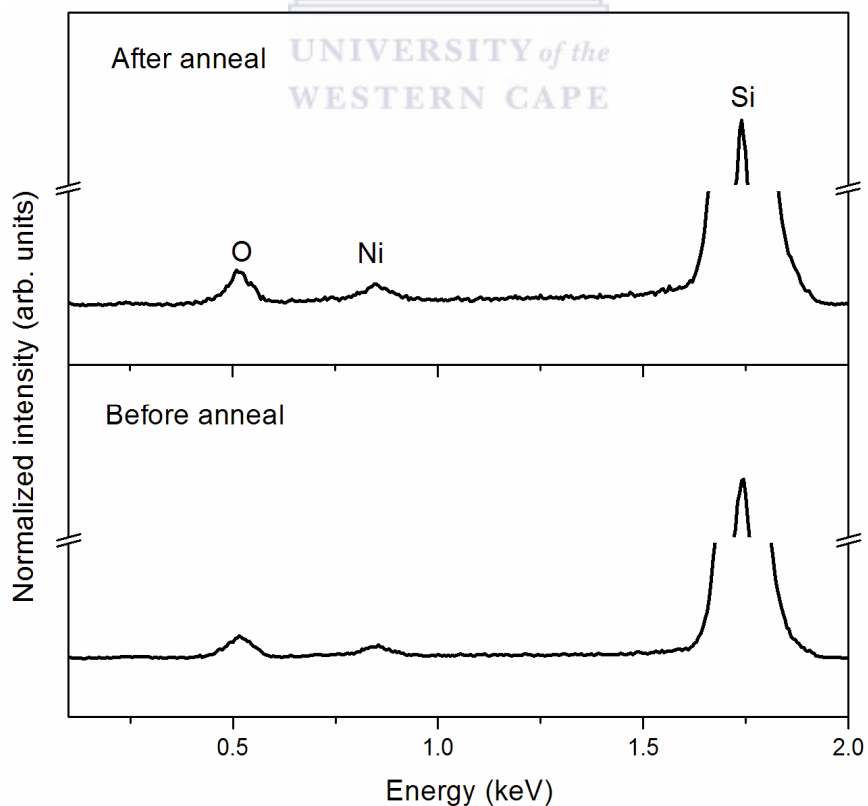

Figure 4.4: *Elemental composition of the substrate before and after the annealing at 500 ℃ in a H_2 ambient*

Figure 4.5 shows SEM micrographs of the material grown on the annealed substrates at different filament-temperatures. Present are entangled, fibre-like material at and below filament-temperatures of 1800 °C. At 2000 °C, agglomerates similar to that observed on the annealed substrate are present. The presence of carbonaceous particles within the sample is characteristic of CNTs deposited by HWCVD at non-ideal conditions [4.9]. The density of the fibre-like material relative to the carbonaceous particles is higher at T_{fil} = 1400 °C and 1800 °C than at 1600 °C. Ni nanoparticles at the terminating sites of the fiber-like material are noticeable in figure 4.5.

The micrographs presented in figure 4.6 show higher magnification images of the materials deposited at different filament-temperatures. It is clear from the micrographs that the diameter-range of the materials decreases with the increase of the filament-temperature. Chhowalla *et al.* [4.7] reported on MWCNTs with diameter-range between 50 - 400 nm. Their diameter-range corresponds well with that shown in figure 4.6; this suggests that these materials are MWCNTs. The much larger diameter CNTs grown at 1400 °C have a minimal degree of buckling and are generally stiffer compared to smaller diameter CNTs.

The arrows in the SEM micrograph of CNTs grown at 1600 °C shown in figure 4.6(b) indicate that the terminating sites are irregularly shaped and much larger than the corresponding CNT diameter. At 1400 °C and 1800 °C the ends appear to be much more spherical and similar in size compared to the CNT diameter.
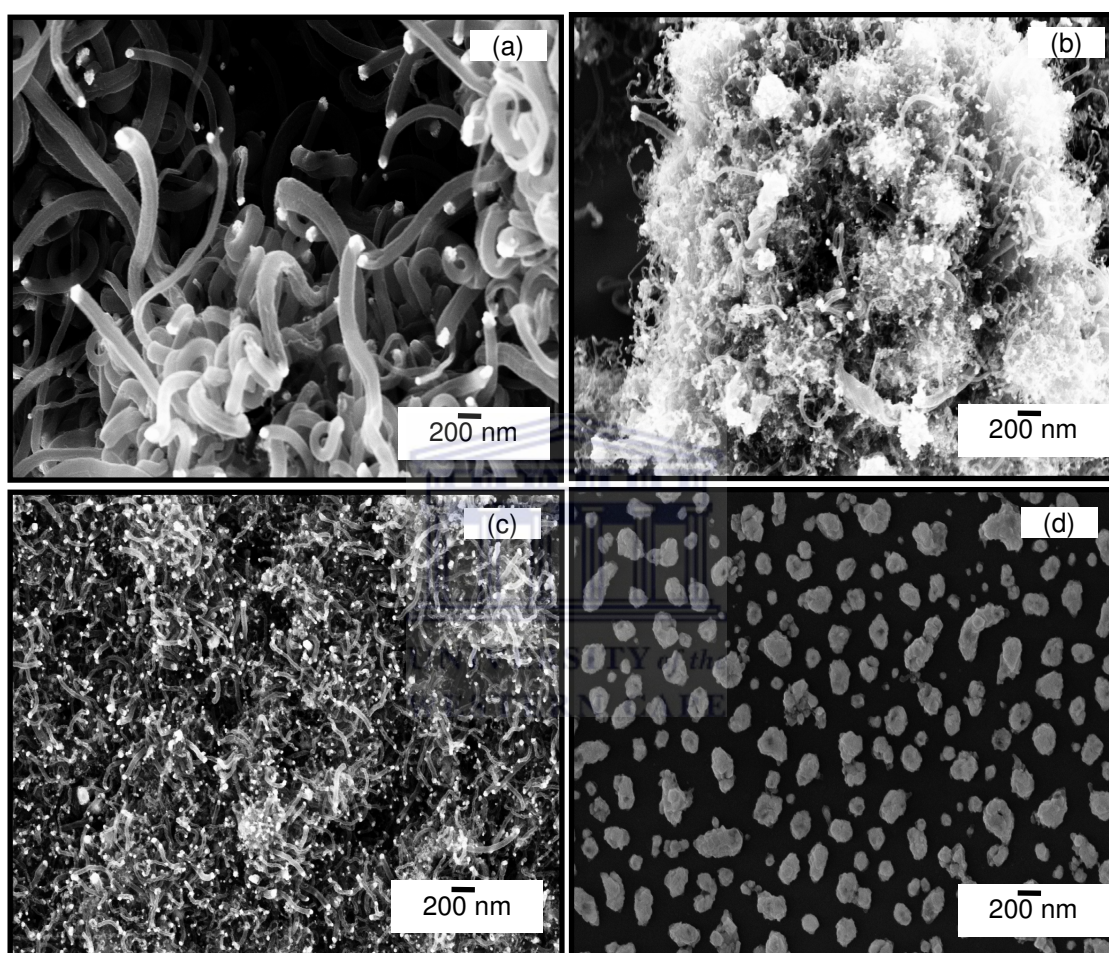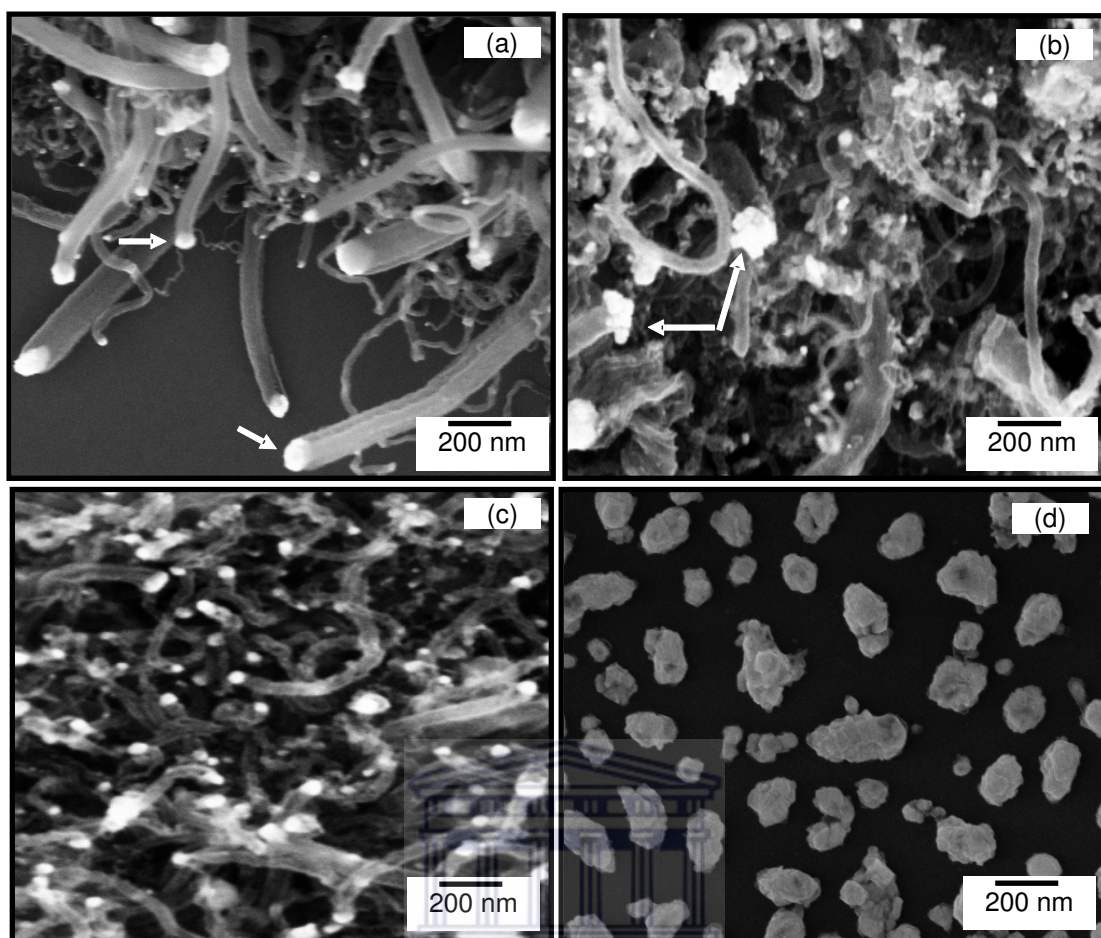
Figure 4.5: *SEM micrographs of the materials deposited at filament-temperatures of: (a) 1400 °C, (b) 1600 °C, (c) 1800 °C and (d) 2000 °C*

Figure 4.6: *Higher magnification SEM micrographs of the materials deposited at filament-temperatures of: (a) 1400 °C, (b) 1600 °C, (c) 1800 °C and (d) 2000 °C*

Figure 4.7 presents EDS spectra of the samples as a function of filament-temperature. The spectra are normalized to the highest peak intensity and reveal the presence of Si, C, Ni and O. The interesting fact here is that the intensities of the C-peaks vary with the filament-temperature, with the highest C-concentration occurring at 1600 °C. Furthermore, the relatively low concentration of Ni to C may be beneficial for a purification process. At 2000 °C, the EDS analysis detects a very low amount of C in the sample compared to other filament-temperatures. Furthermore, the EDS analysis indicates that the brighter particles at the terminating sites of the tubes likely contain the most content of Ni.
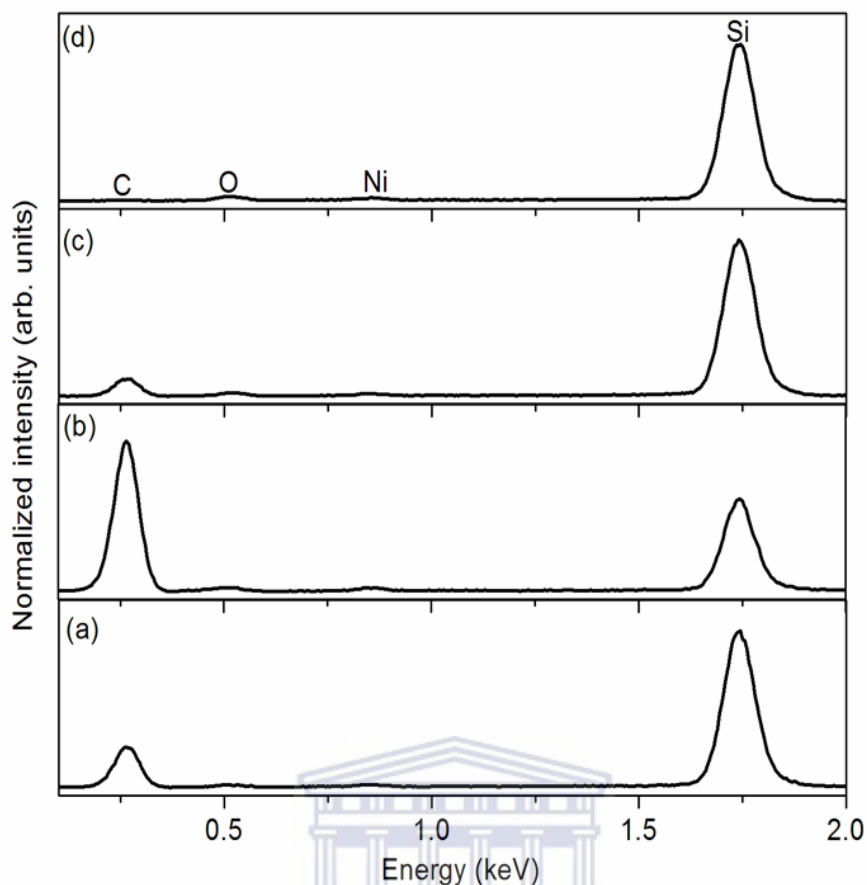
Figure 4.7: *Elemental composition of the samples at a filament-temperature of: (a) 1400 °C, (b) 1600 °C, (c) 1800 °C and (d) 2000 °C*

The morphology results will now be quantified using Raman spectroscopy, which is a useful and non-destructive method for the structural characterization of CNTs. Figure 4.8 shows Raman spectra from two extreme spots on the sample deposited at 1600 °C. The two main features in the spectra are the D-band (disorder-band) and the G-band (graphitic-band) centred around 1350 cm^{-1} and 1580 cm^{-1}, respectively [4.4]. The identical spectra illustrates that the structural properties of the sample are homogeneous over the substrate. Figure 4.9 presents the Raman spectra of the material deposited at different filament-temperatures. The raw spectra did not show any low frequency peaks, i.e. radial breathing modes (RBM), which implies that SWCNTs were not deposited in this study [4.14]. The absence of SWCNTs is ascribed to the low growth temperature of 500 °C compared to the reported CVD-growth temperature range of 800 °C - 950 °C for SWCNTs [4.3].
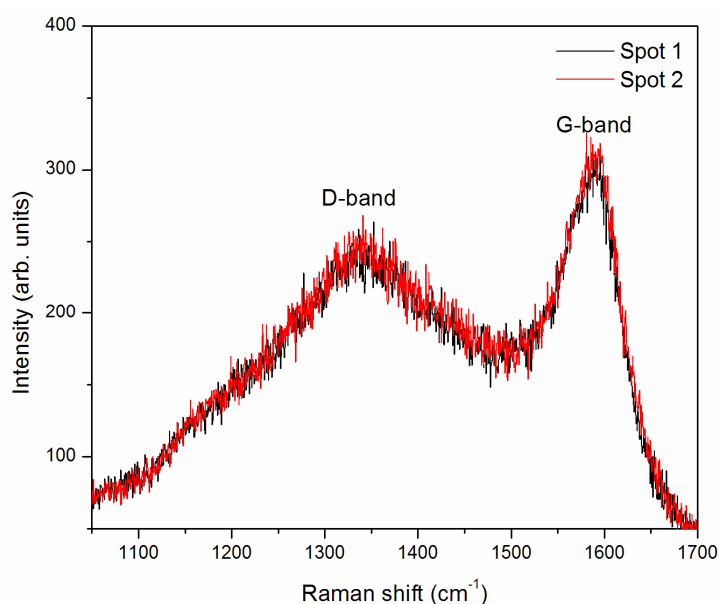
Figure 4.8: *Raman spectra collected at two extreme spots of the sample deposited at 1600 ℃*

The slightly-asymmetrical broadening of the G-band indicates the presence of graphitic material [4.14]. A third order polynomial was used to apply a baseline correction to the Raman spectrum and a smoothing procedure to minimise the noise-to-peak ratio. Applying a Gaussian fit to the spectra provides a quantitative analysis of the sample. The area under the G-band corresponds to the amount of graphitic species and the area under the D-band corresponds to the amount of non-graphitic features, i.e. carbonaceous particles, internal defects such as bamboo-like structures, defects in and interactions between the tube-walls. The width specified by the full width at half maximum (FWHM) of the G-band reveals the structural perfection of the MWCNTs. On the other hand, the FWHM of the D-band is indicative of the distribution of impurities and defects on and within the tube-walls. Furthermore, the ratio of the G- to D-band peak intensities (I_G / I_D) is used as an index to determine the overall structural perfection of the CNTs [4.7]. However, in this study it was found that the FWHM of both the G- and D-bands varies with the filament-temperature, and therefore the ratio of the area of the G- to D-band (A_G / A_D) will be used for determining the structural perfection of CNTs. Presented in figure 4.9 are the raw Raman spectra, whilst the Gaussian-fitting curves as a function of filament-temperature are shown in figure 4.10.

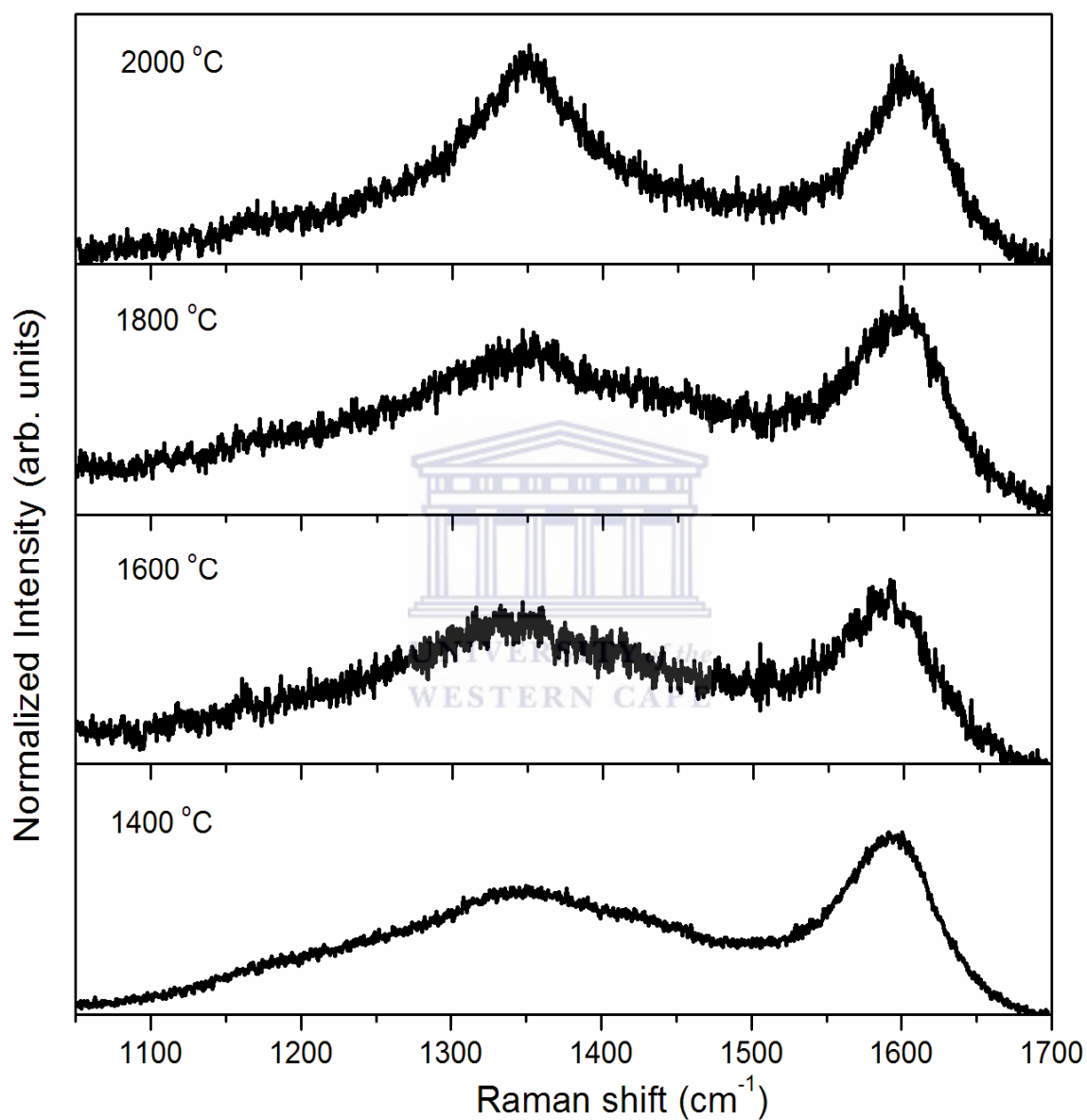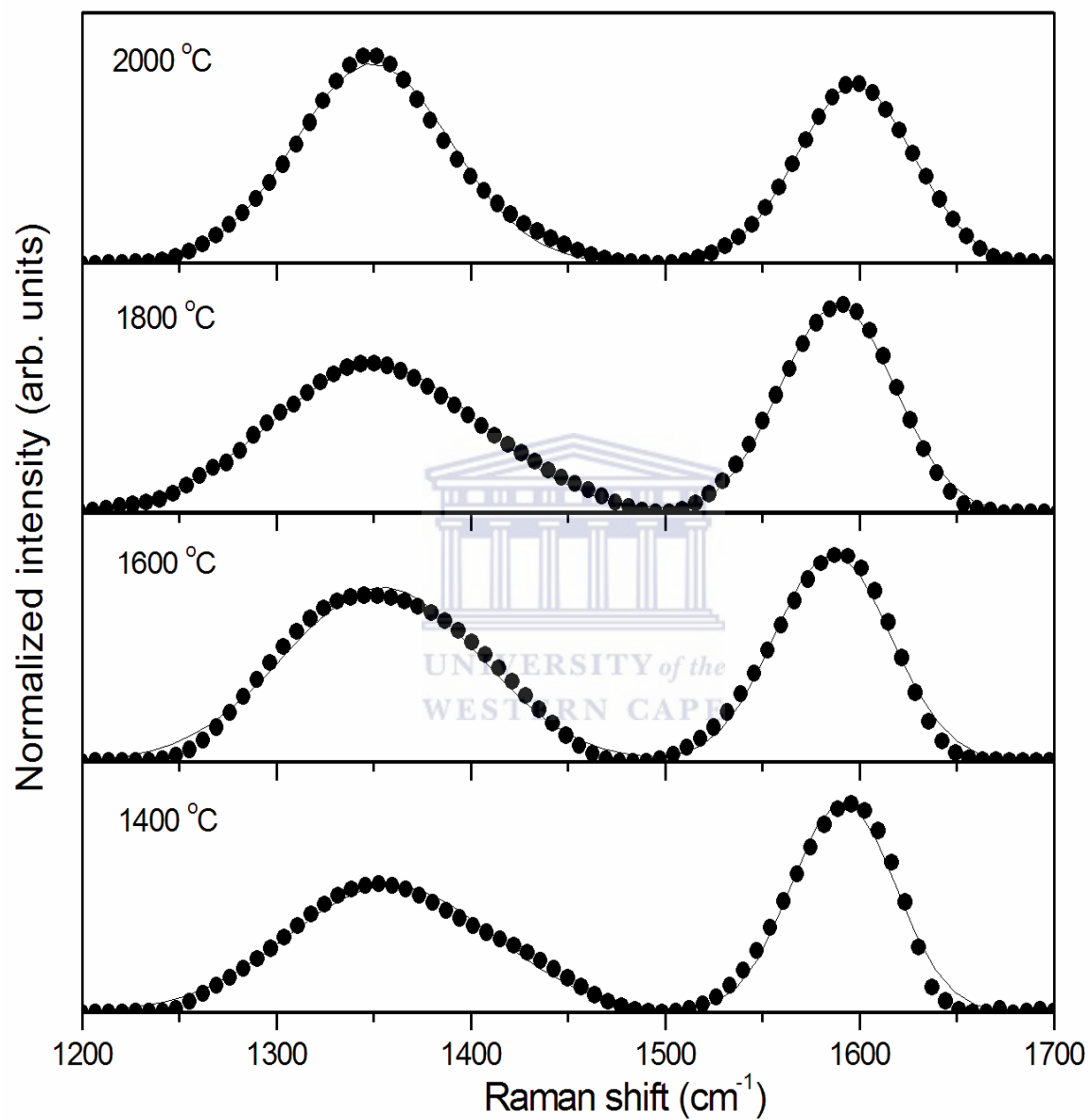**Figure 4.9:** *Raman spectra of the material deposited at different filament-temperatures*

Figure 4.10: *Raman spectra of the material deposited at different filament-temperatures with the Gaussian fitting curves (the black solid line in each case)*

The information obtained from the Gaussian-fitting curves is better illustrated by plotting the Raman features versus the filament-temperature. Figure 4.11 presents a plot that shows the relationship of the A_G / A_D to the filament-temperature. The plot shows that the highest concentration of MWCNTs with respect to defect structures is present at 1400 ℃, in accordance with figure 4.5. At 1600 ℃, the A_G / A_D ratio decreases and recovers slightly at 1800 ℃. This is acceptable, since the SEM micrographs presented in figure 4.5 disclosed that the concentration of carbonaceous particles versus MWCNTs is lowest at 1400 ℃, increased at 1600 ℃ and then decreased slightly at 1800 ℃. The A_G / A_D ratio subsequently reaches a minimum at 2000 ℃, indicating less graphitised species versus the amount of disorder in the sample.
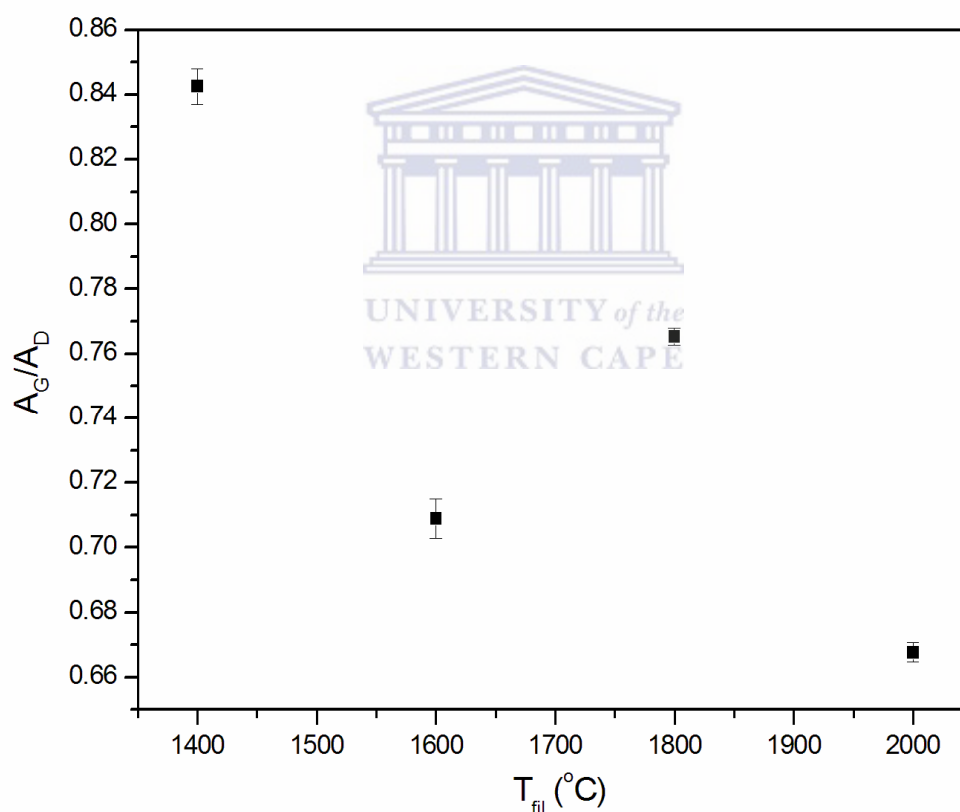

Figure 4.11: *A_G / A_D ratio versus the filament-temperature*

Figure 4.12 shows the $FWHM_G$ as a function of filament-temperature. The superior structural perfection of the MWCNTs at 1400 ℃ is apparent from the narrowest G-band width found at this temperature. However, at 1600 ℃ the $FWHM_G$ increases, implying that there is a decrease in the structural

perfection of the MWCNTs. At 1800 ℃ there is a slight recovery in the structural perfection of MWCNTs, as seen in the lower FWHMG compared to 1600 ℃. At 2000 ℃, the $FWHM_G$ is the widest compared to other filament-temperatures, indicating major structural imperfections in the graphitic material deposited at this temperature.
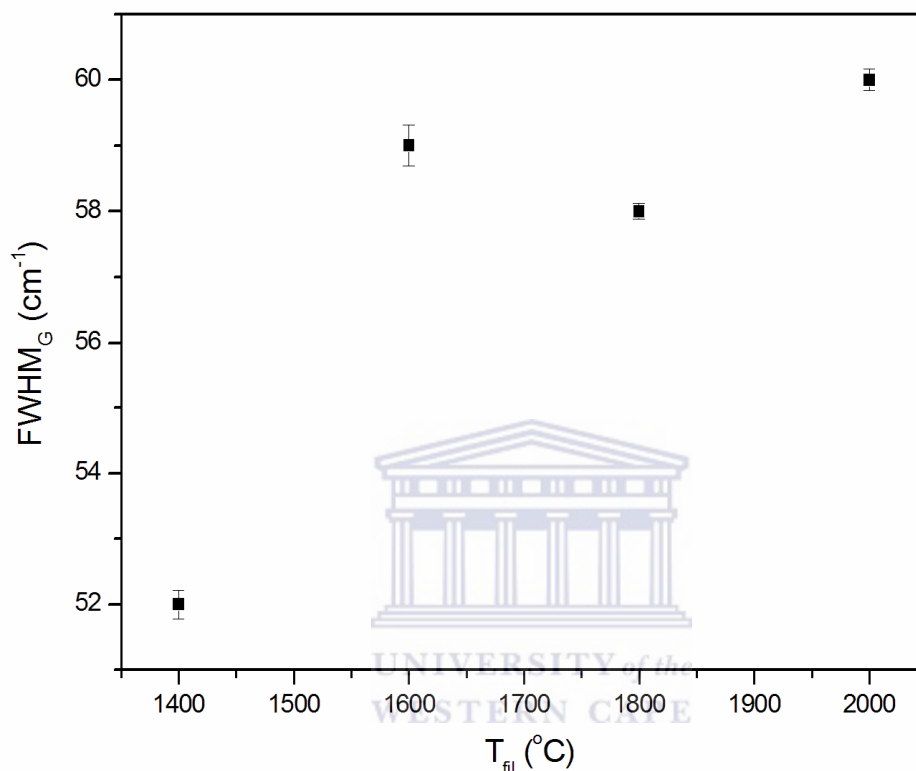
Figure 4.12: *Plot showing the FWHM$_G$ feature of the synthesised material deposited at different filament-temperatures*

Figure 4.13 presents a plot relating the $FWHM_D$ to the filament-temperature. The width of the D-band at 1400 ℃ and 1800 ℃ is wider compared to 1600 ℃. This indicates that the distribution of defects is larger at 1400 ℃ and 1800 ℃ compared to 1600 ℃. Using a transmission electron microscope (TEM), Chhowalla *et al.* [4.7] found that in some cases, sections form in MWCNTs resembling a bamboo-like structure. This may also be the case at 1400 ℃ and 1800 ℃, which would result in the observed broadened $FWHM_D$, regardless of the higher concentration of defects at 1600 ℃.

Figure 4.13: Plot of the $FWHM_D$ feature versus the filament-temperature

The effect of the surface and temperature of the filament on the morphology and structural properties of CNTs is based on a three stage mechanism consisting of various competing kinetic factors. The first stage is at the filament-surface where the CH_4 dissociation rate, the carbon (C) diffusion rate into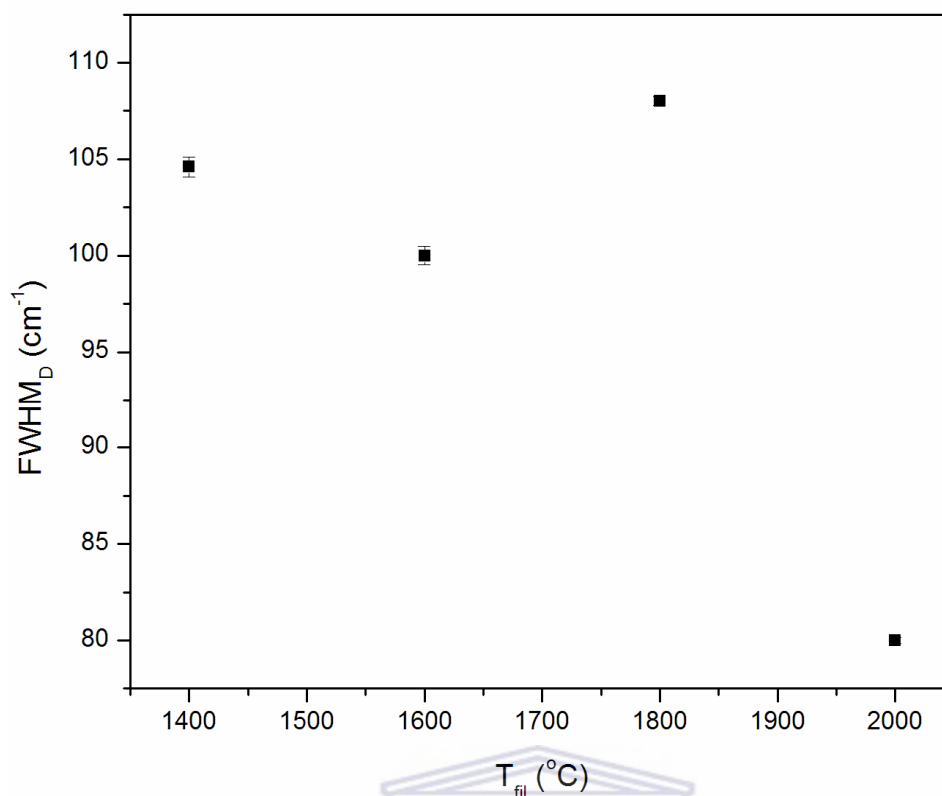 the filament and the rate of atomic hydrogen etching of C occurs [4.6, 4.13]. These factors depend on the temperature of the filament as discussed in *Chapter 3*.

Subsequently, these factors influence the species that will participate in secondary gas phase reactions within the substrate to filament distance, which is the second stage. The third stage is the suggested growth mechanism of CNTs at the catalysts sites, which involves a level of compromise between the dissociation of hydrocarbon species generated in the first and second stages, diffusion of C into the catalysts until the catalyst is supersaturated and the eventual precipitation of C in a crystallized tubular form [4.3, 4.4]. It is therefore obvious that the reactions during the second and third stages are intimately linked to the reactions at the filament surface.

During the first 15 minutes at a filament-temperature of 1400 ℃ the surface of the filament evolves into a WC phase. This ensures a stable filament-temperature and steady rates of C-etching by atomic hydrogen and C-supply for the deposition process. Consequently, at these deposition conditions, this temperature leads to the establishment of a region of compromise between the kinetic factors in all three stages. Subsequently, the synthesised MWCNTs have a decreased concentration of carbonaceous particles compared to other filament-temperatures.

On the other hand, at 1600 ℃ the CH_4 dissociating rate at the filament-surface is higher than the rate of C-diffusion into the filament. Consequently, this resulted in the formation of carbonaceous hemispherical deposits on the filament-surface. The presence of the deposits hinders direct contact between molecular hydrogen and the catalytically active WC-surface, which leads to a decrease in the carbon etching and subsequently an increase in the size of the graphitic deposits. Also, the temperature of the filament varied during the first 15 minutes. Collectively, these factors result in an imbalanced oversupply of C to the second and third stages, leading to an increase the concentration of carbonaceous particles within the sample.

According to the XRD analysis presented in the previous chapter, an increase in the W_2C-content at the filament-surface occurred at 1800 ℃ during the first 5 minutes. Consequently, the C-diffusion rate into the filament increased leading to a depletion in the C-supply for the two subsequent stages. However, at 15 minutes the surface is covered with carbonaceous deposits. This resulted in variations in the temperature of the filament. Regardless of the deposits at 15 minutes, the production of atomic hydrogen is still higher than at a filament-temperature of 1600 ℃. As a result, an enhanced C-etching rate by atomic hydrogen during the secondary reaction and third stages occurs at 1800 ℃. Consequently, these factors result in fewer carbonaceous impurities compared to 1600 ℃.

During the first 5 minutes at 2000 °C only the W_2C phase was detected. As a result, the CH_4 dissociation rate is slower than the C-diffusion rate into the filament, which leads to C-depletion from the ambient. At 15 minutes the surface of the filament was mostly composed of WC and its temperature dropped by almost 100 °C. Nevertheless, an extreme rate of C-etching by atomic hydrogen occurs at this temperature, leading to a decreased probability of MWCNT formation. Consequently, only graphite-like carbon with an increased concentration of defects is deposited at 2000 °C during the first 15 minutes.

The results presented in this chapter also suggest that the heated filament affects the morphology and size of the nanoparticles observed at the terminating sites of the MWCNTs and it is explained as follows. Jehng *et al.* [4.8] argued that the atomic hydrogen species, which increase exponentially with the temperature of the filament [4.6], assists to maintain the activity of the catalysts and weakens the metal-metal bonding. This results in the formation of smaller, more active and a higher density of Ni-nanoparticles at higher filament-temperatures. This process occurs regardless of the direct thermal radiation from the filament, which should result in increased levels of Ni-migration and consequently a higher likelihood of Ostwald-ripening. Chhowalla *et al.* [4.7] showed that the diameter of the CNT increases linearly with the available catalyst area, i.e. the diameter of the Ni-nanoparticles.

Based on these findings, it is proposed that the decrease in the diameter-range of the MWCNTs with increasing filament–temperature is attributed to the decrease in the catalyst diameter brought about by higher levels of atomic hydrogen generation. This suggests that during the first few minutes at 1600 °C the surface of the filament was most likely not covered by the carbonaceous deposits, which led to the preparation of smaller Ni-nanoparticles. This assumption is reasonable considering the relatively constant temperature for the first few minutes at 1600 °C as shown by figure 3.29 in the previous chapter. However, the formation of the carbonaceous deposits below 15 minutes at 1600 °C led to a decrease in the atomic

hydrogen species. Eventually, this led to the observed irregular shaped particles at the terminating sites of the MWCNTs.

Therefore, based on the SEM, EDS and Raman spectroscopy measurements, at the present deposition parameters 1400 °C is the optimum filament-temperature for the deposition of MWCNTs with a superior structural perfection and a relatively lower impurity concentration. This confirms the prediction made in the previous chapter that this temperature will be favourable for CNT deposition because it corresponds to a WC-surface free of carbonaceous deposits and cracks.

4.4   Conclusion

It was found that the temperature and the structural properties of the filament indeed influence the structural properties of the synthesised MWCNTs. Furthermore, the filament-temperature and the state of its surface influenced the morphology and size of the Ni-nanoparticles at the terminating sites of the MWCNTs. During the substrate annealing, Ni-based pyramid shaped nanoparticles formed with different sizes. The diameter-range of the MWCNTs synthesised from these nanoparticles decreased with increasing filament-temperatures between 1400 °C to 1800 °C.

However, even though the tube diameter decreased at 1600 °C, the terminating sites were found to be disfigured and not similar in size to the diameter of the MWCNTs. This was attributed to the decreased atomic hydrogen etching resulting from the occurrence of carbonaceous deposits on the surface of the filament. The density of the MWCNTs relative to the defects in the sample was found to be at a maximum at 1400 °C, but decreased drastically at 1600 °C. On the other hand, at 2000 ° C graphitic material was deposited on the substrate. It was proposed that the depletion of C and extreme etching of atomic hydrogen during the formation of the W_2C phase at 2000 °C collectively prevented the formation of MWCNTs.

A suitable level of atomic hydrogen etching not only played an important role in the creation of regular sized nanoparticles and the prevention of catalysts deactivation, but also during the actual growth by acting as an effective carbonaceous particles etching agent.

Based on the above findings, the optimum temperature and structural properties for a W-filament at the present deposition conditions was determined to be 1400 °C. At this temperature, optimum levels of atomic hydrogen etching and reactive C-species were supplied for the deposition from a relatively stable WC-surface. Consequently, a high density of MWCNTs was synthesized with a minimal concentration of carbonaceous particles and a superior degree of structural perfection.

4.5 References

[4.1] S. Iijima, *Nature*, **354**, 56 (1991)

[4.2] S. Iijima and T. Ichihashi, *Nature*, **363**, 603 (1993)

[4.3] E. Lamouroux, P. Serp and P. Kalck, *Catalysis Reviews,* **49**, 341 (2007)

[4.4] P. Avouris, G. Dresselhaus and M. Dresselhaus, "Carbon Nanotubes: Synthesis, Structure, Properties, and Applications", *Springer*, Germany (2001)

[4.5] R. Raffaelle, B.J. Landi, J. D. Harris, S. G. Bailey and A. F. Hepp, *Materials Science and Engineering B*, **116**, 233 (2005)

[4.6] H. Matsubara and T. Sakuma, *Journal of Material Science*, **25**, 4472 (1990)

[4.7] M. Chhowalla, K. B.K. Teo, C. Ducati, N. L. Rupesinghe, G. A. J. Amaratunga, A. C. Ferrari, D. Roy, J. Robertson, W. I. Milne, *J. Appl. Phys.*, **90**, 5308 (2001)

[4.8] J. Jehng, C. Chen, Y. Dai and J. G. Huang, *Carbon*, **44**, 1808 (2006)

[4.9] E. Salernitano, T. D. Makris, R. Giorgi, N. Lisi, L. Pilloni, F. Sarto and M. Alvisi, *Diamond and Related Materials*, **13**, 305 (2004)

[4.10] R. Sharma, P. Rez and M. M. J. Treacy, *Microsc Microanal*, **11**(Suppl 2), 212 (2005)

[4.11] C. Bower, O. Zhou, W. Zhu, D. J. Werder and S. Jin, *Appl. Phys. Lett.*, **77**, 2767 (2000)

[4.12] V. I. Merkulov, D. H. Lowndes, Y. Y. Wei, G. Eres and E. Voelkl, *Appl. Phys. Lett.*, **76**, 3555 (2000)

[4.13] M. Sommer and F. W. Smith, *J. Mater. Res.*, **511**, 2433 (1990)

[4.14] M. S. Dresselhaus, G. Dresselhaus, R. Saito and A Jorio, *Physics Report*, **409**, 47 (2005)

SUMMARY

In the area of nanoscale science and technology, carbon nanotubes (CNTs) are revered by scientist both from an experimental and theoretical standpoint. These one dimensional structures are envisioned as singular (single-walled) or an ensemble (multi-walled) of graphene-sheets wrapped seamlessly in a specific direction. The remarkable effects the diameter and the direction of rolling the graphene-sheet (chirality) have on the structural properties of the CNTs are manifested in the unusual properties possessed by these materials. CNTs exhibit ballistic electrical transport, which is highly promising for nanoscale electronic device applications. The superior Young's modulus renders CNTs amongst the most rigid known materials. Coupled with the extremely light weight, the extent of enhancing the mechanical properties of materials can only be speculated at this point.

The hot-wire chemical vapour deposition (HWCVD) technique holds the most promise as a suitable route for a low cost, mass-production of CNTs. At this point, using the HWCVD technique it is possible to selectively obtain single- or multi-walled (MW) CNTs and a high degree of control over the tube diameter. Nevertheless, selectively growing CNTs with a specific chirality and producing large quantities of CNTs using HWCVD are still lacking. This is attributed to the fact that the growth process of CNTs is not currently accounted for.

In an effort to understand the intricate growth process of CNTs, scientists worldwide are ceaselessly trying to determine the effect of each deposition parameter on the morphology and structural properties of CNTs. However, few studies have focused on the one factor that distinguishes the HWCVD from other forms of CVD, which is the filament itself.

In this regard, this study focussed on investigating the carburization of a tungsten (W) filament during the synthesis of CNTs. Subsequently, the effect that the temperature and structural properties of the carburized filament have on the morphology and structural properties of the deposited CNTs was investigated. The structural changes in the filament induced by carburization influences the deposition process in the following manner:

- $T_{fil} = 1400\ °C$:   The surface of the filament underwent a faster transition from a W_2C to a WC phase, which had a relatively constant temperature for the deposition. This ensured a more stable filament-temperature, which led to optimum C-supply and atomic hydrogen etching rates for the synthesis of MWCNTs with lesser defects and a superior structural perfection.

- $T_{fil} = 1600\ °C$:   During the first 15 minutes the surface of the filament is covered with graphitic hemispherical deposits. At 60 minutes the filament was covered with a solid graphite-like carbon layer. This resulted in variations in the temperature of the filament and a lower atomic hydrogen etching rate. Consequently, structurally inferior MWCNTs with a high defect concentration were synthesised.

- $T_{fil} = 1800\ °C$:   Increased levels of atomic hydrogen resulted in a higher concentration in the W_2C content of the filament-surface, which led to the formation of cracks. At 60 minutes of exposure, the filament was covered with a solid graphite-like carbon layer and was fully carburized. During the first 15 minutes, the higher atomic hydrogen levels led to a decrease in the size of the Ni-nanoparticles, as evident in the reduced diameters of the synthesised MWCNTs compared to lower filament-temperatures. Compared to 1600 °C, a decreased concentration of non-MWCNTs

impurities was present. However, compared to 1400 °C the smaller diameter MWCNTs have more buckling in the tube-walls.

- T_{fil} = 2000 °C: During the first 5 minutes, the surface of the filament consisted of only the W_2C phase. Consequently, this led to the formation of cracks. Full carburization and formation of an encapsulating graphite-like carbon layer occurred at 60 minutes. During the first 15 minutes, extreme levels of C-etching by atomic hydrogen occurred. Moreover, C-depletion from the ambient accompanies the formation of the W_2C phase. Consequently, the deposition of defect-rich graphite-like carbon occurred.

It is therefore concluded that at the current deposition conditions the ideal filament-temperature is 1400 °C. A slower carburization rate occurred at this temperature accompanied by the synthesis of entangled MWCNTs with a minimal impurity concentration and a superior structural perfection.